Università Politecnica delle Marche
Scuola di Dottorato di Ricerca in Scienze dell'Ingegneria
Corso di Dottorato in Ingegneria Industriale

Design of a metamaterial-based hand held vibration probe

Ph.D. Dissertation of:
Alessandro Annessi

Supervisor:
Prof. Paolo Castellini

Assistant Supervisor:
Prof. Paolo Chiariotti
Prof. Milena Martarelli

Ph.D. Course coordinator:
Prof. G. Di Nicola

Abstract

Le misure vibrazionali sono un punto di riferimento nella dinamica strutturale. Lo stesso vale anche per la diagnostica dei guasti e la valutazione della qualità del prodotto in vari campi dell'industria, dalle linee di produzione dei componenti ai prodotti finiti. Queste misure sono solitamente eseguite utilizzando accelerometri piezoelettrici collegati alla struttura in esame. Il collegamento è solitamente realizzato tramite adesivi o cera d'api, magneti o perni filettati. Tuttavia, il processo di installazione di questi sensori può richiedere molto tempo e, in alcuni casi, può essere irreversibile o addirittura non consentito. Le sonde vibrazionali di tipo hand-held sono state ampiamente utilizzate in passato, anche se le loro prestazioni (ad es. gamma di frequenze di lavoro e accuratezza complessiva) risultano inferiori rispetto alle installazioni fisse. Tuttavia, la diffusione dei robot nell'ambito dell'industria 4.0, caratterizzata dall'obiettivo di produzione a zero difetti, ha motivato un nuovo interesse per questo tipo di soluzione. Le sonde di misura vibrazionali tipo hand-held sono costituite da componenti che devono garantirne la linearità entro un determinato intervallo di frequenza e il contatto costante con la struttura in prova. Inoltre, le vibrazioni spurie, dovute alla manipolazione da parte di un operatore umano o di un robot, devono essere evitate introducendo un elemento di disaccoppiamento. Normalmente, vengono impiegati materiali convenzionali come la gomma e il silicone, per via del loro comportamento viscoelastico. Tuttavia, questi materiali possono subire modifiche al loro comportamento dinamico quando soggetti a condizioni ambientali diverse. Lo scopo di questa tesi è dimostrare il vantaggio nell'adottare metastrutture come elementi di disaccoppiamento nelle sonde vibrazionali di tipo hand-held. La metastruttura sviluppata si basa su una ripetizione periodica di celle unitarie caratterizzate da una forte separazione modale. Ne consegue, quindi, un ampio intervallo di frequenze di funzionamento.

Abstract

Vibrational measurements are a landmark in structural dynamics. This is true also for fault diagnosis and product quality assessment in various fields of industry, from production lines of components to finite products. These measurements are usually performed using piezoelectric accelerometers attached to the structure under investigation. The connection is usually made using adhesive or bees-wax, magnets or threaded pins. However, the process of installing these sensors can be time-consuming and, in some cases, irreversible or even not allowed. Hand-held vibration probes were widely used in the past, even though their performances (i.e. working frequency range and overall accuracy) were lower compared to fixed installations. However, the spread of robots in the framework of industry 4.0, characterized by the zero defect manufacturing target, caused a new interest in this solution. Hand-held vibration measurements probes are made of components that must guarantee linearity within certain frequency range as well as constant contact with the structure being tested. Furthermore, spurious vibrations, due to the handling by a human operator or a robot, need to be avoided introducing a decoupling element. Normally, conventional materials, like rubber and silicon, are exploited, taking advantage of their viscoelastic behavior. However, these materials may undergo changing on their dynamic behavior when subject to different environmental conditions. The aim of this thesis is to demonstrate de advantage of adopting metastructures as decoupling elements in hand-held probes. The design of the metastructure developed is based on a periodic repetition of unit cells characterized by a strong mode separation and, thus, a wide frequency bandgap.

Contents

List of Figures

List of Tables

Chapter 1

Introduction

Vibration testing has always been a standard in industry for condition monitoring (CM) in machinery and product quality assessment. Being able to determine the optimum time to carry out maintenance in production machinery is crucial to avoid breakdown and production loss. This is possible thanks to reliable CM techniques, which are not only able to determine current condition, but also give reasonable predictions of remaining useful life. To perform this task, machines need to be instrumented with sensors (usually accelerometers) measuring their vibration signature over time, permanently or on a regular basis [7]. On the other side, during the manufacturing process, it is fundamental to evaluate if the product satisfies the required design specifications and if there is any issue related with its functionality. For this purpose, in-line testing and inspection is crucial to monitor the characteristic of the assembled product. The introduction of collaborative robots (cobots) opens up new opportunities for implemented production, reducing completion time and minimizing error, enhancing flexibility and accuracy in manufacturing processes in which the presence of a human operator is mandatory to adapt the operation to actual condition or to teach the cobot by demonstration without prior specific programming [8, 9, 10, 11, 12]. In this scenario, in-line testing and inspection or condition monitoring are processes completely suitable with the use of cobots, leading to better precision and consistency during measurements than a human operator and still characterized by task flexibility. Industrial and collaborative robots are part of the new framework of industry 4.0, increasing automation in manufacturing processes. Furthermore, they are characterized by a strong digitalization and networking, where every machine or product is *smart*, i.e instrumented with sensors and connected to the network to store data, which is fundamental for monitoring and diagnostics [13, 14, 15]. The integration of collaborative or industrial robots with server computers, sensors and actuators, all connected to the same network can lead to innovative ways to perform non-destructive testing (NDT) and monitoring [16]. In this context, industry is moving towards the so called *Zero Defect Manufacturing (ZDM)* [17, 18, 19].

A wide variety of techniques is available for dimensional in-line testing of products, spanning from contact (friction-roller type, caliper-type) to non-contact measurements (optical, pneumatic, ultrasonic and electrical techniques) [20, 21]. Dimensional tolerances can be verified using machine vision and robots on moving objects [22] or warm-die forged workpieces can be timely corrected from the forming process using optical methods [23]. A different way to look for faults is by exploiting vibration, using non-contact (proximity probes, laser Doppler vibrometers) or contact (accelerometers) techniques.

Laser Doppler vibrometry (LDV) has taken strong roots in the quality control field, thanks to its non-intrusive peculiarity, high sensitivity and accuracy. Di Giulio et al. tested the mechanical reliability of electronic devices by means of a scanning laser Doppler vibrometer with the aim to extend the electro-optic approach to an high percentage of the production line [24]. Vanlanduit et al. proposed a robust and fully automatic process for scanning laser Doppler vibrometer measurements and data processing technique for drop-out removal, applied to a mask of a picture tube [25]. Vass et al. used laser Doppler vibrometry and wavelet analysis for fault diagnosis on assembled universal electric motors for washing machines on a production line [26]. On the other side, LDV has several drawbacks. Firstly, its cost is not negligible compared to traditional instrumentation like accelerometers. Secondly, they need to be handled carefully due to their working principle and construction. Moreover, it is likely to suffer from poor surface return of the laser signal, due

to sub-optimal surface conditions, leading to signal drop-out and, thus, presence of outliers in the acquired data. Furthermore, LDV measurement range is limited to relatively small displacements. Maintaining laser spot position is a crucial factor to perform good measurements, thus, instrumentation need to be set up properly in relation to the application. In addition, speckle noise occurs when measuring rough surfaces of objects moving during each cycle time on the production. Lastly, laser vibrometers requires a proper isolation from floor vibrations because it is a relative sensor line [27, 28, 29, 30, 31, 32].

The traditional alternative to expansive laser-based non-contact measurement is the usage of the well known accelerometer. This is a cheap and reliable solution for quality assessment using vibration signals, which can be also employed in harsh environments. Plaza et al. used a triaxial accelerometer signal to evaluate the surface finish of products, exploiting properly extracted vibrational features through different methodologies [33]. Reis et al. used multivariate analysis and optimization on vibration signals from accelerometers to assess noise quality of compressors and, thus, identify non-conforming products on the assembly line [34]. Measurement problems with accelerometers come out when dealing with installation constraints. The mounting process is quite demanding in terms of time and human resources. In fact, accelerometers need to be positioned manually on the structure using an adhesive elements, magnets or permanent connections.

Encouraged by the novel industrial technology environment, those issues can be tackled thanks to the use of collaborative robots together with a new design of probes for vibration measurements, which could be engineered to be installed on the end effector of the robot itself. The so-called vibration probe is an instrument which allows to perform measurements pushing the accelerometer against the surface to be investigated. The most important component inside it, is the decoupling element, which is required to couple the accelerometer to the test surface in a controlled manner, ensuring contact and avoiding undesirable vibrations due to the handling. Exploiting new vibration isolation design solutions (i.e. phononic crystals and metamaterials), the decoupling element can be tailored for the specific application, allowing an excellent measurement bandwidth. Therefore, a cheaper and reliable solution for in-line testing or quality inspection, i.e the hand accelerometer probe, is suitable in the new fast and smart industrial framework and can be exploited more effectively than in the past, lowering the costs but not compromising with measurement performance and time efficiency.

In this thesis, a metastructure, acting as a vibrational mechanical filter, is designed and experimentally validated to be used as an efficient decoupling element for a vibration hand probe.

In Section 2, a brief overview of the typical instrument for measuring vibration, the accelerometer, is made. Advantages and drawbacks of the measuring process are considered and different mounting techniques performance are compared. Motivation to use vibration probes and the proposed solution are presented. Subsequently, phononic crystals and metamaterials are introduced. Firstly, a brief overview of the state of the art is carried out, listing and describing relevant works in the field. Then, the theoretical basis to approach the study of periodic structures are introduced and fundamental working principles are detailed.

In Section 3, the metastructure unit cell is designed accordingly to the application requirements. The band diagram is numerically computed evaluating the full 3D bandgaps present for the proposed unit cell. Mode shapes related with the bandgap opening mechanism (global modes) are shown along with the closing ones which are local modes. A 1x1x3 finite metastructure is analyzed numerically, carrying out both static and dynamic simulations. Lastly, the transmission is evaluated for both undamped and damped condition, introducing a complex Young modulus.

Section 4 will address the experimental validation of the proposed metastructure. Initially, dimensions of the fabricated samples are checked to verify they meet the manufacturer tolerances. Computerized tomography is performed on each sample outlining the presence of internal dust leaved by the manufacturing process. Thereafter, a compression test is performed on the metastructure to measure the force-displacement curve, which will be used to evaluate the optimum preload value for the metastructure in operating conditions. The compression data is also used to validate the numerical model, retrieving the structure stiffness and thus the experimental Young modulus. Afterwards, a scanning laser Doppler vibrometer is employed to evaluate the operational deflection shapes of the metastructure under vibration measuring on a point grid on the sample top and side. The transmissibility function is then measured experimentally and compared with the numerical results. The reproducibility of the experiment is evaluated with a campaign on a single metastructure. Lastly, the transmissibility of each sample is measured and compared, obtaining

the response uncertainty related with the manufacturing process.

In Section 5, the proposed metastructure is tested in operating conditions to assess its performances as a decoupling element. Different geometries for the accelerometer connection are evaluated, choosing the more efficient one. Then, the optimal preload for each solution is chosen based on experimental data. Measurements are then repeated to check the reproducibility of the setup and the performances of different samples.

To reduce the structure encumbrance, a multi-material modular approach for the metastructure is presented in Section 6. A sensitivity analysis is carried out to check the bandgap performances dependence on different geometric parameters, choosing the best arrangement. The band diagram is then evaluated and mode shapes characterizing the bandgap are shown.

Finally, conclusions are drawn in Section 7 and future work is outlined.

Chapter 2

State of the art on sensors and metamaterials

2.1 Measuring with accelerometers

Among all the different sensors employed to measure vibrations and shocks, the most important one, due to its performance and relatively low cost, is the accelerometer. An accelerometer is an electromechanical transducer that produces at its output terminals an electrical output proportional to the acceleration to which it is subjected. It belongs to the class of inertial sensors due to its construction and working principle. In fact, it is composed by a single degree of freedom (dof) system in which a proof mass, a spring and a damper are present. Its base configuration is reported in Fig. 2.1. The accelerometer has to be firmly fixed to the structure under testing. If the structure is subjected to an acceleration, the proof mass will be also accelerated to the same rate. Thus, a force has to be present to move the proof mass which is related to the stiffness of the single dof system. Therefore, a measure of the acceleration is possible measuring the spring deformation, which is proportional to the force needed to move the known mass [35]. The accelerometer is a system of the second order, described by the following equation in the frequency domain:

$$\frac{x_2}{\ddot{x_1}} = \frac{K}{-\frac{\omega^2}{{\omega_n}^2} + \frac{2\zeta i\omega}{\omega_n} + 1} \tag{2.1}$$

where $K = 1/{\omega_n}^2$ is the static sensitivity, ω_n is the undamped resonance frequency of the system, ζ is the critical damping ratio and i is the imaginary unit. x_2 is the output displacement, converted into electrical voltage by a displacement sensor, whilst $\ddot{x_1}$ is the input acceleration. The magnitude of the typical transfer function of an accelerometer is shown in Fig. 2.2. It is characterized by a wide useful frequency range for measurements, typically from 0.5 to 10000 Hz with 5% of linearity. Commonly, the active element of an AC accelerometer consists of piezoelectric discs or slices loaded by seismic masses and held in position by a clamping arrangement.The piezoelectric elements produce a charge proportional to the applied force. When the accelerometer is subjected to vibration, the combined seismic mass exerts a variable force on the piezoelectric element, proportional to the

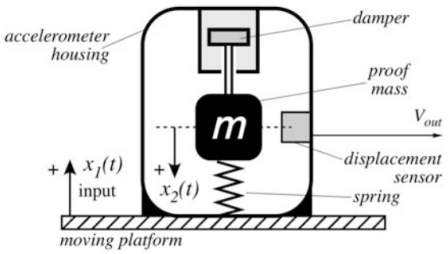

Figure 2.1: Concept of a linear mechanical accelerometer [1].

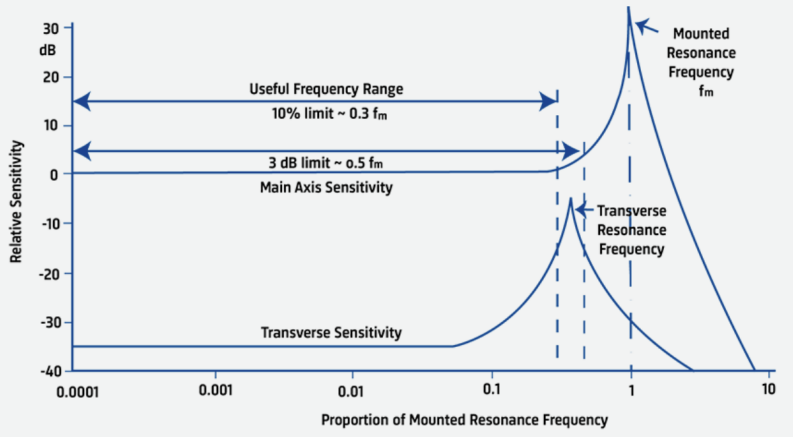

Figure 2.2: Accelerometer frequency response function and useful measurement range (Courtesy Brüel & Kjær).

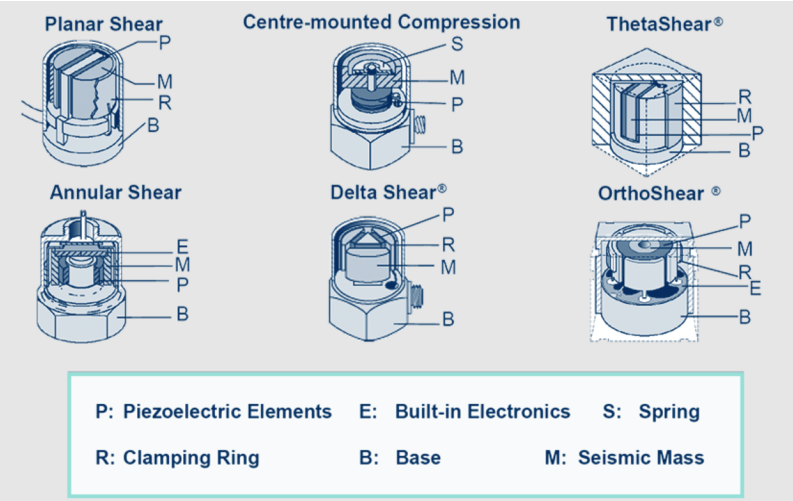

Figure 2.3: Different designs and elements in the accelerometer (Courtesy Brüel & Kjær).

acceleration of the seismic masses. Common designs are shown in Fig. 2.3. Nowadays, the majority of piezoelectric accelerometers have a built-in electric circuit for impedance conversion from the high impedance signal from the piezoelectric material into a low impedance voltage signal. This standard, which is called *Integrated Electronics Piezo-Electric* (IEPE), enable both power supply and signal to be trasmitted via one shielded wire. For a comprehensive and detailed explanation about vibration measurement and accelerometers the reader could refer to [1, 35, 36, 37, 38, 39]. Vibration testing is usually performed using accelerometers attached to the structure under testing. So far, this option has been considered as the optimal one because it allows the best transmission of the vibration wave from the object under test to the sensor in a broad frequency range. That is the case of secure installations as stud mounting, its frequency response is shown in Fig. 2.4 (configuration 1). However, it requires to realize a threaded seat on the object, which may not always be allowed. Besides, the connection of the sensor to the structure is time-consuming and irreversible. Other installation solutions exploited so far are the use of adhesive or beeswax, which allow a good response (shown in Fig. 2.4 (configuration 2 and 3)) whilst having the inconvenience of being still time-consuming and inefficient at high temperature. The use of magnets (shown in Fig. 2.4 (configuration 4 and 5)) is another widely used approach, but it has the drawback of acting as a low-pass filter on the signal propagating from the structure under test to the sensor, that causes a loss of the high frequency information during the measurement. Lastly, accelerometers could be mounted on hand probes, i.e. metal shrill tips which are held onsite by hand. A hand probe is shown in Fig. 2.4 (configuration 6) with its relative frequency response. The hand probe

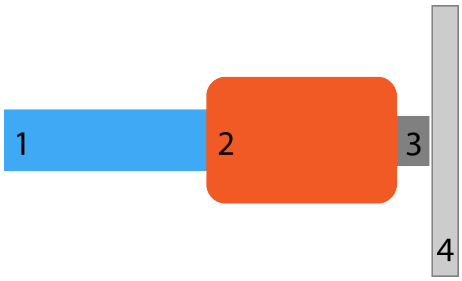

Figure 2.5: Vibration hand probe schematics: (1) the handle, (2) the decoupling element, (3) the piezoelectric accelerometer and (4) the vibrating surface under test.

performance, in terms of measurement range, is the worst in comparison with other available solutions but it allows a quick and easy measurement. The narrowness of the measurement bandwidth is mostly due to the operator handling the probe itself, acting as an even stronger low-pass filter with respect to magnet mounting configuration.

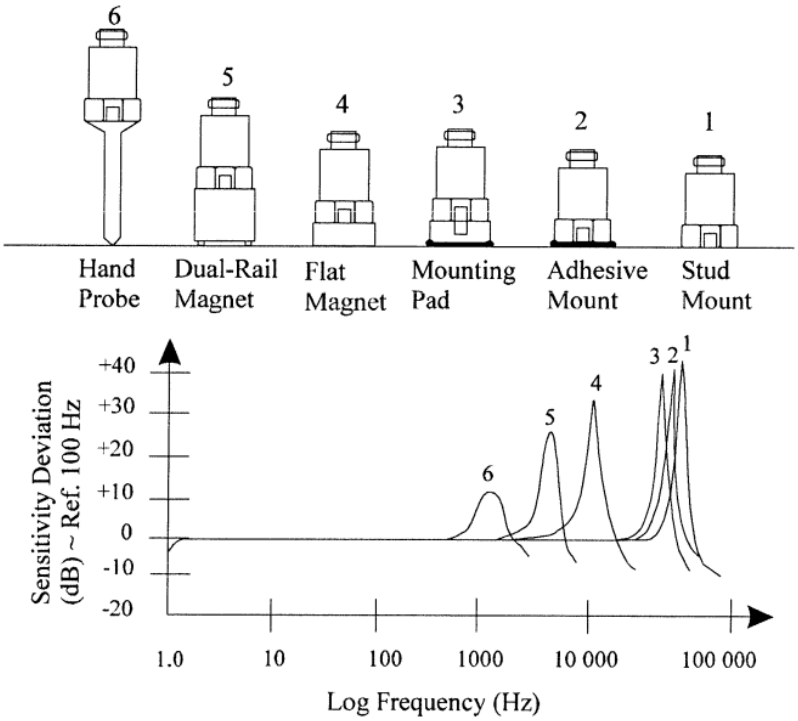

Figure 2.4: Mounting configurations and their related frequency response (Courtesy of PCB piezotronics).

2.2 Hand-held probes

Hand probes had been used in the past as a versatile and quick way to do vibration measurements, even if their performance was limited to low frequency ranges. Nowadays, as the use of robots and cobots for holding sensors advances, the idea to use hand probes in vibration testing is starting to emerge as a valid alternative to the approaches described in 2.1. The design of the currently employed hand-held vibration probes is different compared to the traditional ones shown in Fig. 2.4 (configuration 6). The schematics of the vibration probe is depicted in Fig. 2.5. It is composed by three main elements:

1. A handling, which could be wielded by a human operator or a robot arm (in the perspective of in-line testing).

Figure 2.6: DISCOM vibration probe solution https://discom.de.

2. A decoupling element, which is fundamental to avoid the introduction of spurious vibrations during the test due to the handling and to ensure constant contact between the accelerometer and the surface under test.

3. A lightweight accelerometer of the piezoelectric type, mounted on the tip of the probe.

To perform a measurement, the accelerometer is pushed against the surface under test by means of the probe itself, which has a handle or a proper connection to a robotic arm. The strength (i.e. the force) used to press the probe needs to be included in a specific range driven by experimental laboratory evaluations. In fact, the measurement range of the instrument is strongly dependent from the exerted force and the relative deformation of the decoupling element, modulating its working frequency range. Moreover, the accelerometer mass is a crucial parameter to be considered. In fact, it needs to be chosen properly in order to avoid the presence of a low resonance frequency peak due to the component itself, affecting again the measurement frequency range. Some prototypes available on the market so far rely on the strong damping properties of rubbery and silicon materials to get rid of any disturbance in the measurement [40]. An example of a commercial probe for vibration measurements, from the company DISCOM GmbH, is shown in Fig. 2.6. Alternative innovative solutions are still needed to design modular decoupling units which allows to work on variable frequency ranges in relation to the application. Metastructures represent a good solution for this purpose.

2.3 Introduction to phononic crystals and metamaterials

In the past decades, new material concepts in the acoustic and vibration fields have been introduced, revolutionizing the way of designing devices for wave shaping.

Phononic crystals (PnCs) were officially outlined in 1993 thanks to a work from Kushwaha et al. in which they draw the analogy between electronic, photonic and phononic crystals. The interest was motivated by the presence of complete phononic bandgaps in periodic composite, in which, in analogy with the photonic case, wave propagation would be forbidden, opening possibility for a multitude of applications in which vibration isolation is required [41]. In particular, they are artificial crystals for elastic and acoustic wave shaping, only possible thanks to the tunable dispersion properties of the crystal. The most relevant one is the presence of bandgaps, i.e. a frequency range in which no wave propagation is allowed in the material band diagram. Characteristic applications in this fields are related with vibration attenuation, which are possible exploiting crystal bandgap properties [42] and wave guiding, obtained by the introduction of defects in the crystal matrix which confine acoustic energy in the bandgap region [43, 44, 45, 46, 47], lensing [48, 49, 50] and imaging [51]. An unusual property which can occur under certain conditions is negative refraction [52], which can be employed to design lenses with sharp focus [53, 54, 55]. Furthermore, researchers are being inspired from nature geometries to develop novel metamaterials to manipulate wave propagation in subwavelength scale [56] and tunable sound reflectors for noise-shielding [57]. In addition, fractal lattice structures have been exploited for the design of phononic band gap based

devices [58, 59]. A comprehensive overview on progress, future perspective and challenges of PnCs is done in [60, 61], ranging from their origins to the latest novelties.

Dealing with PnCs, the bandgap opening mechanism is related to the specific lattice considered. Thus, phononic crystal performances are limited by its characteristic dimension, i.e. there is no possibility to work beyond the diffraction limit. To overcome this issue, local resonance concept can be exploited to work in a subwavelength condition [62].Combining lattice structure with local resonance, bandgaps widen and increase in number due to the superposition of both different phenomena [63].

In analogy with PnCs, a metamaterial is a conventional material (e.g. plastic or metal) arranged in a particular manner, mostly but not necessarily in a periodic fashion, which gives it specific properties regarding wave propagation.The term *metamaterial* was introduced by Walser [64] to highlight the aim to achieve performance beyond the limitation of conventional composites.

Unit cells, from which the metamaterial is constituted, have characteristic dimensions smaller than the wavelength of external impinging wave. Thus, they can be treated as effectively homogeneous materials at the frequency of operation and can, therefore, be characterized by some effective material parameters which can be retrieved via analytical and numeric methods (i.e. artificial composites can be considered as metamaterials only when operating below a certain frequency) [65, 66, 67, 68, 69]. Moreover, metamaterials are innately dispersive unless active elements are included [70].

Metamaterials are widely known in various fields of physics for their unusual properties usually not available in nature. From vibration to acoustics, they changed the way material properties could be tailored to a specific purpose. Nowadays, they are starting to emerge as valid solutions in a wide variety of engineering applications. For example, they can be used for vibration isolation [71] and anchor losses reduction [72] in Micro Electro Mechanical Systems (MEMS). Moreover, metamaterial resonant panels are arising as a lightweight and compact solution for sound and vibration isolation [73, 74, 75, 76]. Metaconcrete made by single and double mass resonators can be installed in buildings for trapping wave energy from shock and vibrations, reducing stress in the mortar when subjected to dynamic loading [77, 78]. Mir et al. proposed a MetaWall for sound insulation and energy harvesting as an alternative for traditional roadside noise barriers [79]. Muhammad et al. proposed an attenuation solution for bearing induced vibration using a metahousing, consisting of a dissipative elastic metamaterial and exploiting resonant units mismatch to broaden the metamaterial working range [80]. Chiral mechanical metamaterials are a general purpose solution for flexible structures. Possible industrial applications include morphing airfoils, smart structures, auxetic stents and flexible electronics, compliant structures and impact attenuators [81]. A comprehensive review on metamaterials for vibration control can be found in [82], in which Dalela et al. hits all the fundamental topics, from 3D resonant metamaterial to periodic arrangement of trees for traffic vibration suppression.

A new way to think about wave manipulation is by exploiting active component in traditional elastic and acoustic metamaterials [83] Wang et al. proposed a tunable elastic metamaterial for broadening the bandgap range at low frequency. The activation of magnets, which are embedded in each unit cell, allows to use the metamaterial as a tunable waveguide [84].

The concept of locally resonant material was firstly introduced by Liu in [62] and then exploited widely in the world of metamaterial. Claeys at al. [85] designed and analyzed a metamaterial plate for acoustic isolation adding bending local resonators in a rectangular core sandwich, allowing good performances through a lightweight structure. The proposed metaplate can be integrated in structural parts, used in harsh environment and easily tailored to specific applications. Built-it local resonators can be exploited also to design metamaterial beams for vibration suppression without sacrificing the beam's load bearing capacity [86].

Matlack et al. proposed a scalable elastic metastructure for vibration and noise mitigation at low frequencies which exploited the architected lattice geometry to selectively control the locally resonant modes [87].

Star-shaped and cross-shape inspired metastructures are valid alternatives to resonant metamaterials and are designed to be used as efficient vibration isolators in the low frequency range [88, 89, 90].

In literature, many strategies to obtain wide frequency bandgaps also in the low range can be found. Meng et al. proposed a rainbow metamaterial that exploits spatially varying resonators to obtain a broader frequency bandgap. Multi-frequency broadband attenuation could be achieved

using a non-symmetric configuration of resonators [91]. In [63], a three dimensional truss-lattice structure is proposed for low frequency wave propagation absorption, coupling the Bragg resonance, originated by a body-centered cubic lattice, and a local resonance, established by locally increasing beam diameters. Claeys et al. proposed different combinations of multiple resonators to achieve multiple stopbands for reducing vibration in a known transmission path, acting on specific targeted frequency zone [92]. Another technique is to exploit active components such as piezoelectric patches, distributed periodically on the host structure [93]. In dissipative elastic metamaterials, damping properties of the constituent unit cell can be exploit to merge attenuation region induced by different resonators, obtaining a broaden version with respect to the undamped case [94]. Furthermore, the mixing of local resonance with Bragg bandgaps mechanisms allows to widen the attenuation frequency range [95]. The last method, proposed in [96] is called modes separation and it is practically exploited in this thesis. This method will be explained in detail in Section 2.8.3.

Several works present in the literature concern the design of metamaterials characterized by wide and low frequency bandgaps exploiting mode separation technique. In Tab. 2.1 works related with this topic are summarized in a straightforward way, comparing their performances. The bandgap performance is defined as the ratio of the frequency band ($\Delta\omega$) over the central frequency (ω_c) as given in 2.2

$$\frac{\Delta\omega}{\omega_c} = \frac{2(\omega_t - \omega_b)}{\omega_t + \omega_b} \tag{2.2}$$

where ω_t is the bandgap closing frequency and ω_b is the bandgap opening frequency. The wider the bandgap, the greatest the bandgap performance. Percentage in Tab. 2.1 is relative to the first bandgap.

Table 2.1: Metamaterials based on mode separation technique and related references.

Author	**Composition Type**	**Working direction**	$\mathbf{\Delta\omega/\omega_c}$	**Year**	**Reference**
Jiang	Single-Material	3D	161%	2021	[97]
Muhammad	Single-Material	3D	160.2%	2020	[98]
Fei	Single-Material	3D	83%	2020	[99]
Muhammad	Multi-Material	2D	92%	2020	[98]
D'Alessandro	Single-Material	3D	140%	2020	[96]
Kumar	Single-Material	2D	87%	2019	[100]
Barnhart	Multi-Material	1D	58%	2019	[94]
Zhou	Multi-Material	1D	155%	2019	[101]
Elmadih	Single-Material	3D	63%	2019	[102]
Muhammad	Multi-Material	2D	150%	2019	[103]
D'Alessandro	Single-Material	3D	134.7%	2019	[104]
D'Alessandro	Single-Material	3D	64%	2018	[105]
D'Alessandro	Single-Material	3D	159%	2017	[6]
Lu	Multi-Material	3D	100%	2017	[106]
D'Alessandro	Single-Material	3D	132.2%	2016	[107]
Acar	Single-Material	2D	74%	2013	[108]

A special attention is addressed to the results proposed by D'Alessandro et al. in [6] regarding mode separation, which are described in details in Section 2.8.3.

2.4 Direct lattice

In the introduction to Solid State Physics by Hofmann [3], a lattice structure is defined as a set of regularly spaced points. Necessary condition to have a so called Bravais lattice is to have their positions arranged in space as multiple of the generating vectors, i.e. vectors creating the lattice by translations equal or multiple of their length. In three dimensions, a lattice can be defined as all the points that can be generated by the vector $\mathbf{R}$ which is the linear combination of three generating vectors $\mathbf{a_1}$, $\mathbf{a_2}$ and $\mathbf{a_3}$. The lengths of $\mathbf{a_1}$, $\mathbf{a_2}$ and $\mathbf{a_3}$ are often referred as lattice constants.

$$\mathbf{R} = n_1\boldsymbol{a_1} + n_2\boldsymbol{a_2} + n_3\boldsymbol{a_3} \tag{2.3}$$

where $n_{1,2,3} \in \boldsymbol{Z}$. Considering lattice symmetry, possible Bravais lattice in three dimensions are 14 and they are shown in Fig. 2.7. A lattice defined as a regular grid of points in space is called direct. Now, a volume of space defined by lattice points is considered. If, when translated through all the vectors of the Bravais lattice, it fills space without either overlapping itself or leaving voids, it is called primitive unit cell of the lattice. Each primitive unit cell contains only one lattice point. A special choice of the primitive unit cell is the Wigner–Seitz cell which is the region of space that is closer to one given lattice point than to any other. The volume of a primitive unit cell is given by $V_{uc} = |\boldsymbol{a_1} \cdot \boldsymbol{a_2} \times \boldsymbol{a_3}|$. In the solid state physics, the points constituting the lattice structure are atoms, the crystal building blocks. In a phononic crystal, they are usually rods [109, 110] and holes [111]. In periodic lattice structures is important to pay attention to symmetries, which could be of different kind. Translational symmetry, which is the lattice generating mechanism by translation, has already been introduced. Other symmetries could be mirror lines, rotational axis, inversion symmetry. Their occurrence influences the crystal properties.

2.5 Reciprocal lattice

The direct space is the domain in which the direct lattice leaves and where pressure or displacement fields are computed for the periodic structure together with vibrational modes. On the other hand, to study the wave propagation in the lattice (i.e. dispersion relation, bandagaps, equifrequency contours), it is fundamental to define the reciprocal space, also known as wave vectors space, in which a reciprocal lattice is defined. It is described as the lattice which includes the Fourier transform of the wavefield of the original lattice. In other words, it is formed by the set of wave vectors K that yield plane waves with the periodicity of the given direct lattice, satisfying the following equation

$$e^{-i\mathbf{K}\cdot\mathbf{R}} = 1 \qquad \forall \mathbf{R} \tag{2.4}$$

The reciprocal primitive lattice vectors are defined as

$$\boldsymbol{b}_i = \frac{\epsilon_{ijk}\boldsymbol{a}_j \times \boldsymbol{a}_k}{\boldsymbol{a}_1 \left(\boldsymbol{a}_2 \times \boldsymbol{a}_3\right)} \tag{2.5}$$

where $\boldsymbol{a}_{1,2,3}$ are the direct lattice vectors and ϵ_{ijk} is the completely anti-symmetric Levi Civita symbol. Equation 2.5 results from the orthogonality property between the two spaces which is written as $\boldsymbol{b}_j \cdot \boldsymbol{a}_i = 2\pi\delta_{ij}$, where δ_{ij} is the Kronecker delta. Thus, the regular basis for the reciprocal lattice can be written as

$$\mathbf{K} = m_1\boldsymbol{b_1} + m_2\boldsymbol{b_2} + m_3\boldsymbol{b_3} \tag{2.6}$$

where $m_{1,2,3} \in \boldsymbol{Z}$. Any linear combination of the reciprocal lattice vectors reaches a point on the reciprocal lattice.

Bringing the Wigner-Seitz cell from the direct space to the reciprocal space using Fourier transform, its analogous in the wave vector space is obtained, which is the first Brillouin zone. Spanning all the Bloch waves (details in Section 2.6) inside it, is sufficient to obtain, because of periodicity, all Bloch wave in the periodic medium. Thus, band structures are represented with respect to the first Brillouin zone Considering all the symmetries of the unit cell, the first Brillouin zone can be reduced to a smaller area called irreducible Brillouin zone (IBZ), which is the smallest set of waves to fully describe the crystal dispersion. This a great advantage because it allows to reduce computation time relevantly in numerical modeling.

An example of a simple square lattice is depicted in Fig. 2.8a with its relative first Brillouin zone in the $\boldsymbol{k}$-space on Fig. 2.8b. The reciprocal lattice vector is simply defined in terms of the direct lattice constant as $b = 2\pi/a$.The triangular area, depicted in red in the reciprocal space, is the IBZ obtained reducing the larger one exploiting lattice diagonal and axial symmetries. Furthermore, the IBZ contour on which the wave propagation properties of the material will be investigated, is indicated as $\Gamma - X - M - \Gamma$.

Basis vectors/crystal axes	Angles	Crystal system
$a \neq b \neq c$	$\alpha \neq \beta \neq \gamma \neq 90°$	triclinic
$a \neq b \neq c$	$\alpha = \gamma = 90° \beta \neq 90°$	monoclinic
$a \neq b \neq c$	$\alpha = \beta = \gamma = 90°$	orthorhombic
$a = b \neq c$	$\alpha = \beta = \gamma = 90°$	tetragonal
$a = b \neq c$	$\alpha = \beta = 90° \gamma = 120°$	hexagonal
$a = b = c$	$\alpha = \beta = \gamma \neq 90°$	rhombohedral
$a = b = c$	$\alpha = \beta = \gamma = 90°$	cubic

(a)

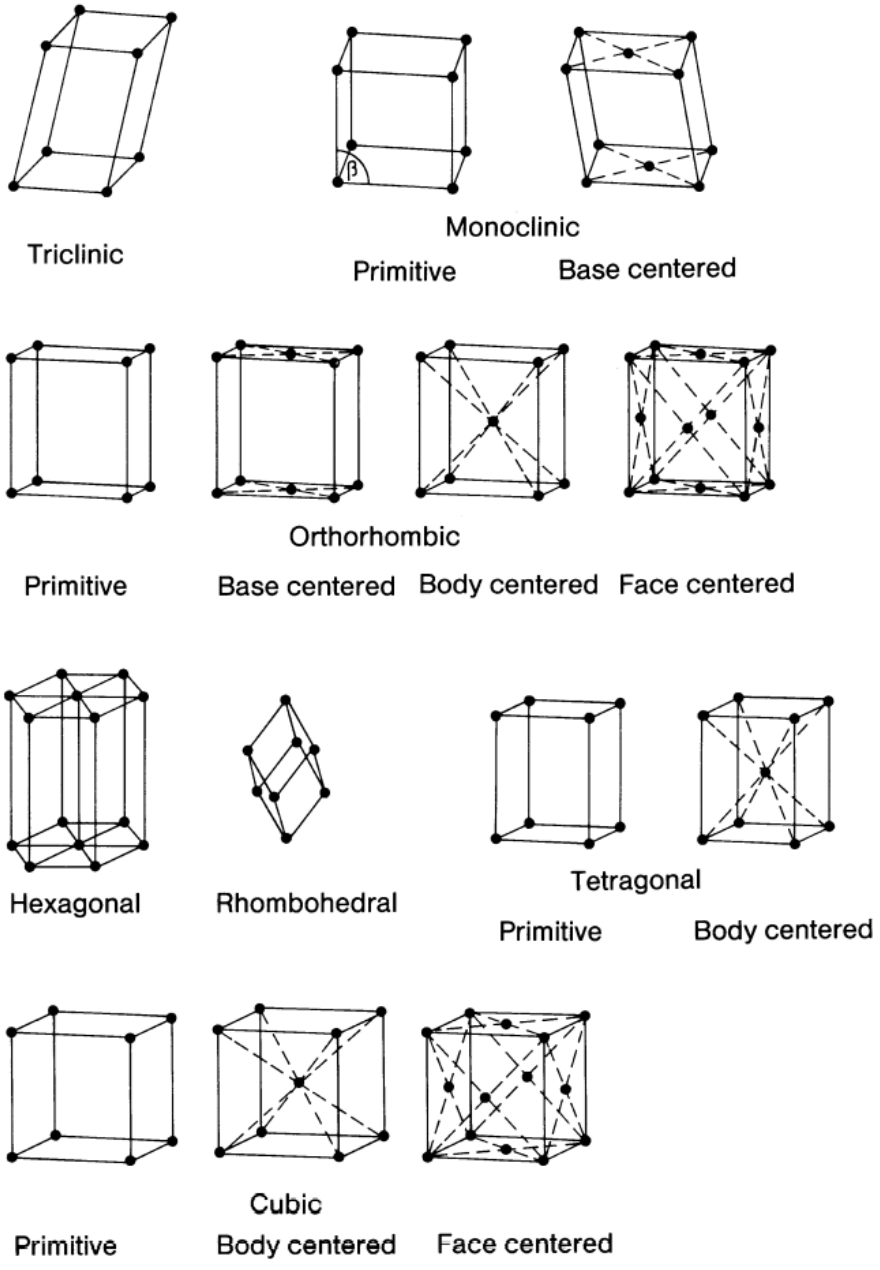

(b)

Figure 2.7: Bravais lattice in three dimensions [2].

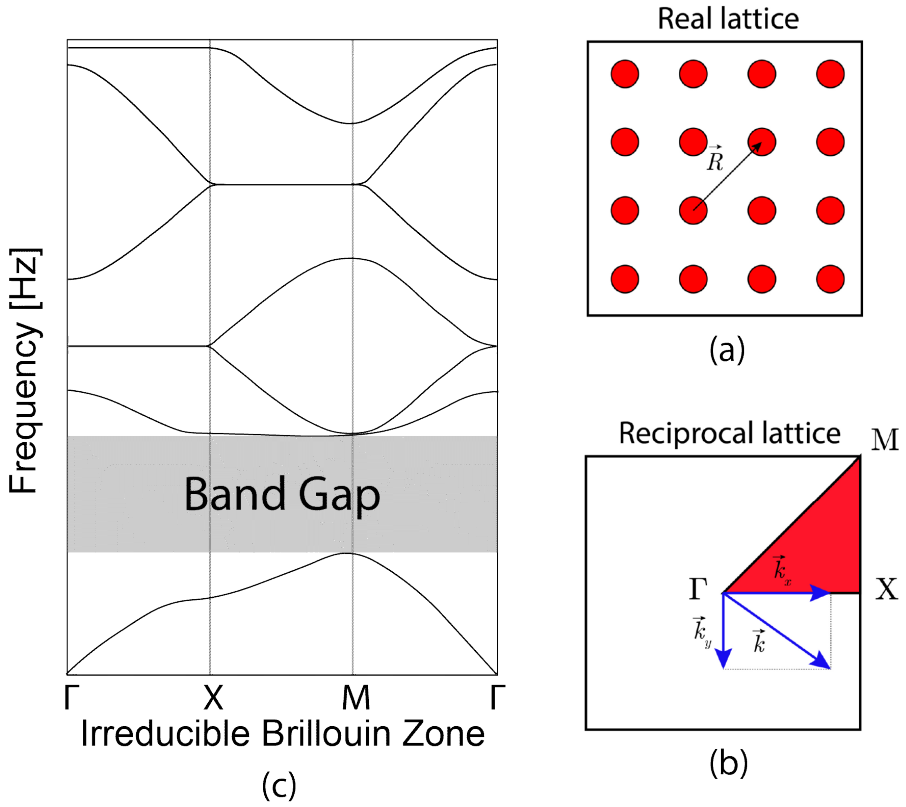

Figure 2.8: (a)Direct and (b)reciprocal representations for a simple square lattice crystal. The IBZ is defined as $\Gamma - X - M$ due to lattice symmetries. (c) Example of a typical band structure for the considered lattice.

2.6 Bloch theorem

When dealing with crystals and periodic structures in general, the Bloch's theorem is a fundamental pillar. In solid state physics it is introduced referring to periodically arranged atoms and it is essential to describe the motion of electrons in a periodic potential in the context of quantum mechanics. Dealing with phononic crystals and metamaterials, the periodic modulation of material properties takes the place of the periodic potential. In our case, wave propagation is described by classical Helmholtz equation where coefficients are periodic:

$$-\nabla \cdot (c(\boldsymbol{r}) \nabla u(\boldsymbol{r})) = \omega^2 u(\boldsymbol{r}) \tag{2.7}$$

where c is the wave propagation and u is the displacement field. They are both periodic with the lattice and dependent on position $\boldsymbol{r}$. ω it the angular frequency.

The eigenmodes of the periodic Helmholtz equation are Bloch waves of the form

$$u(\boldsymbol{r}) = e^{-i\mathbf{k}\cdot R} \tilde{u}(\boldsymbol{r}) \tag{2.8}$$

where $\mathbf{k}$ is the Bloch wave vector and $\tilde{u}(\boldsymbol{r})$ is a function with the same periodicity of the Bravais lattice. In fact, it must guarantee that $\tilde{u}(\boldsymbol{r}) = \tilde{u}(\boldsymbol{r} + \boldsymbol{R})$, where $\boldsymbol{R}$ is any lattice vector. One of the most important consequence of this theorem is that the solution is simply a plane wave modulated by a lattice-periodic function. Periodic boundary conditions, which are derived from Bloch theorem, are needed to compute band structure of a single unit cell of a periodic material. Firstly, the unit cell is chosen to be externally limited by pairs of boundaries. Each pair is defined to have one boundary (S_1) to be obtained by a lattice vector translation $\boldsymbol{R}$ of the other (S_2). Therefore, the periodic boundary conditions written for each pair is defined for displacement as:

$$\tilde{u}(\boldsymbol{r} + \boldsymbol{R})|_{S_1} = \tilde{u}(\boldsymbol{r})|_{S_2} \tag{2.9}$$

or

$$u(\boldsymbol{r} + \boldsymbol{R})|_{S_1} = e^{-i\mathbf{k}\cdot\boldsymbol{R}} \quad u(\boldsymbol{r})|_{S_2} \tag{2.10}$$

2.7 Dispersion and band diagram

Different methods are available to retrieve the band structure of a phononic crystal or a metamaterial in the hypothesis of infinite media, relying on the application of the Bloch-Floquet theorem:

- Transfer Matrix Method (TMM)
- Plane Wave Expansion (PWE)
- Multiple Scattering Theory (MST)
- Finite Difference Time Domain (FDTD)
- Finite Element in Time Domain (FETD)
- Finite Element Method (FEM)

All the listed methods can be adapted to work in 1D, 2D or 3D dimensions. PWE is a popular general purpose method for band structure computation. It is limited in handling different media (except for rigid inclusions in air or holes in a solid matrix) and in dealing with complex geometries due to the use of a structure factor in the formulation. Furthermore, its convergence is slow due to the number of Fourier harmonics to be included in the computation. MST has similar limitation with respect to PWE, being an analytical method for the evaluation of the scattered field of simple atoms geometries (such as cilinders or spheres) on a uniform background. FTDT is a time-domain method, with the advantage to cover a wide frequency range with a single simulation run. It can give results in both space and time domain. However, its numerical efficiency for computing band structure can be very slow, especially for resonant structures. To operate with more complex unit cells, considering various boundary conditions, it is helpful to exploit FEM. Furthermore, FEM strengths are the availability of commercial softwares, which are characterized by ease of use, and open-source ones, which are highly customizable [112].

In our case, a finite element model built in COMSOL Multiphysics© is used to retrieve dispersion curves numerically in conjunction with periodicity boundary conditions (i.e Bloch-Floquet periodicity) already introduced in Section 2.6. Firstly, the wavenumber directions to be used are defined, spanning all the wavevectors of the IBZ with a finite resolution. Then, the Floquet BC are applied, in pairs, over the faces of the unit cell defining the periodicity. Lastly, the eigenfrequency problem is solved for the equation of motion over all the wavevectors. This method is characterized by a relatively fast computation speed (depending on domain meshing and consequently number of degrees of freedom) and incredibly ease of implementation. In fact, the user is not required to fully understand the underlying finite element theory to obtain accurate dispersion curves, essential in our application. A first drawback related with this method is the inability to reduce model domain dimensions, thus decreasing the computation time. Furthermore, in the case of complex unit cell designs, the number of mesh modes, i.e. the number of degree of freedom, could increase excessively leading to long computation time [113].

2.8 Bandgap mechanics: Bragg scattering, local resonance and mode separation

As previously introduced in Section 2.3, wave propagation bandgaps, in a phononic crystal or a metamaterial, can be obtain from Bragg scattering or local resonance mechanism. In addiction, a different strategy to open extremely wide bandgaps is referred as mode separation. In the following, an overview of the different bandgap opening mechanism is done.

2.8.1 Bragg scattering

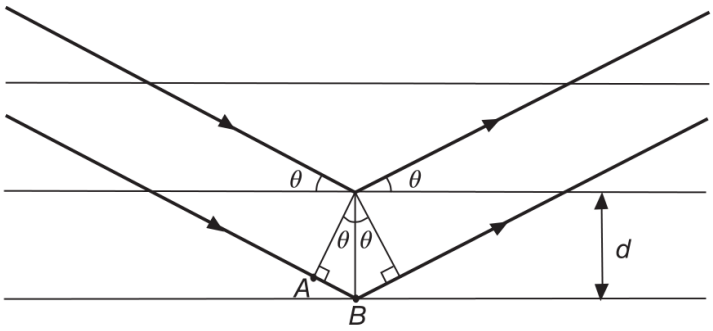

Figure 2.9: Scheme for the derivation of Bragg condition. Horizontal lines represents crystal planes while bold lines the incoming wave [3].

Bragg theory studies the reflection of an incoming wave considering flat lattice planes of the crystal, in the case of wavelengths similar to atoms spacing. A geometrical scheme for the derivation of Bragg condition is represented in Fig. 2.9. Horizontal lines represent crystal planes, which are spaced by a distance d. The incoming wave, depicted as bold lines, propagates in the crystal with an angle of incidence and emission equal to $90°-\theta$. To obtain constructive interference, the path length distance between the wave reflected from one layer and the next one needs to be multiple of the wavelength λ. Referring at the geometrical scheme, it means that $2AB = n\lambda$, where AB is the distance between the points defined in figure and n is a natural number. From geometrical considerations, $sin\theta = AB/d$, and thus we obtain the Bragg condition for all the crystal layers

$$n\lambda = 2dsin\theta \tag{2.11}$$

Bragg scatting theory deals with the direct lattice space. When considering the reciprocal space, Laude description must be taken in consideration, which is a more general fashion to formulate the scattering problem:

$$|\mathbf{k}|sin\theta = \frac{\pi n}{d} \tag{2.12}$$

where $k = 2\pi/\lambda$ is the magnitude of the wave vector $\mathbf{k}$. Bragg and von Laue conditions are equivalent but expressed in different domains. More details on Bragg scattering can be retrieved in [114] and [115].

The concept behind Bragg scattering can be employed to design phononic crystals working at high frequencies in the microscale and nanoscale dimensions thanks to the use of simple geometries [116] in the ultrasonic frequency range [117, 118]. More bulky crystals can be design to operate in air in the audible range of frequencies with lattice constant in the order of centimeters [119] or even decimeters [120]. The condition to exploit Bragg scattering is to have a $\lambda < 2d$ (which is called Bragg limit). Thus, bandgap derived from this phenomenon depends on the lattice constant dimensions. Therefore, to design crystals in the low frequency regime, lattice constants must increase accordingly and could reach excessive dimensions. This is the major drawback of Bragg diffraction based design.

A typical band diagram obtained for a simple square lattice by Bragg mechanism is shown in Fig. 2.8c.

Another way to investigate the band structure of a periodic system is to consider complex eigenfrequencies in the dispersion model. In this case, band diagram is determined analytically exploiting transfer matrix method. Its derivation for a known geometry is not the target of our particular study. Thus, it is described in a qualitative way, without reporting the equations describing the phenomena.

For this study, a waveguide of circular section is patterned regularly varying its value, as shown in Fig. 2.10a. The resulting band diagram, in terms of real and imaginary part of the wavevector, is shown in Fig. 2.10b. The imaginary part of the transmission is equal to zero at all frequencies except in the band gap region, in which it has non-zero values. This indicated that non-propagating Bloch waves (i.e. evanescent waves) emerge in the bandgap range, with amplitude decaying exponentially in the direction of propagation.

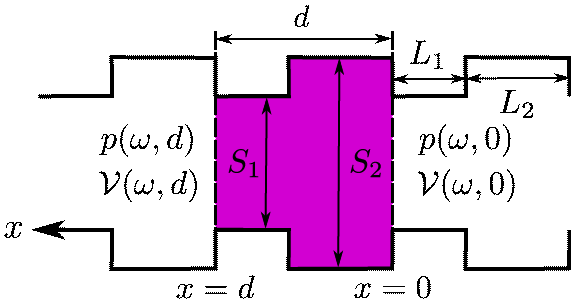

(a)

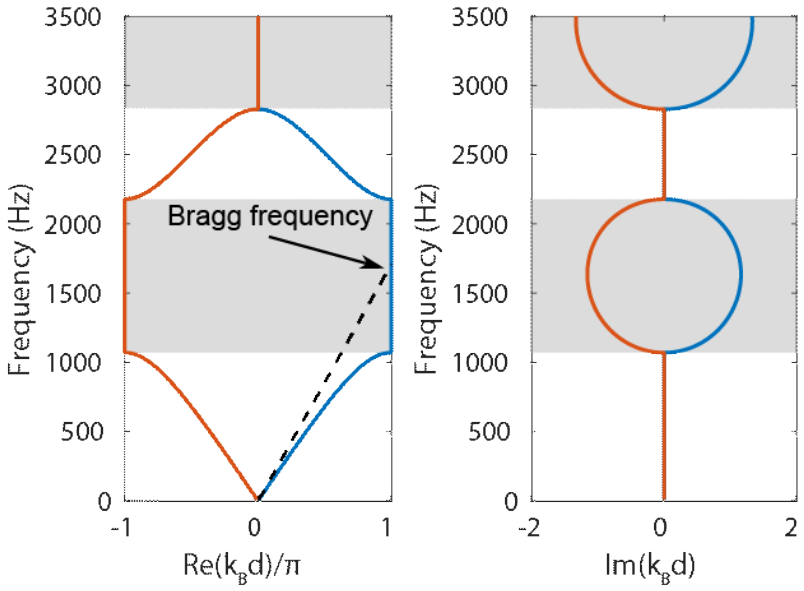

(b)

Figure 2.10: Complex band diagram (b) related to a periodic variation of the diameter in a waveguide (a) [4].

2.8.2 Local resonance

As detailed in Section 2.8.1, PnCs frequency performances are restricted by the lattice vector size due to the Bragg limit. A way to overcome this issue is to exploit the so-called Locally Resonant Materials (LRM). A resonance type bandgap can appear at frequencies below the Bragg limit, meaning it is possible to push versus low frequencies without increasing the size of the unit cell in the crystal. The target is to operate with metamaterials at subwavelength level, for example, designing structures to attenuate sound propagation with a unit cell dimension smaller than the wavelength in air [5]. Liu et al. where the first to introduce this kind of materials being inspired from the electromagnetic field [62]. LRM are made out of an hardcore unit, usually made from metal, encapsulated in a soft coating like silicon rubber and lastly immersed in a polymer such as epoxy. The resonant structure is composed by the metal unit, which acts as mass, and the soft coating layer which is characterized by a certain elasticity, and thus acts as a spring. The resulting local resonance can appear at very low frequency (about two orders of magnitude below the Bragg frequency).

As an example, a 2D unit cell composed by a single layer cylindrical core made of steel coated with polymer and an external steel thin layer, all embedded in water, in considered. The transmission through a series of 5 unit cells is reported in Fig. 2.11a. A sharp dip is present at low frequency, meaning that wave propagation is barely allowed at that specific range. To understand better the underlying mechanism, the unit cell displacement field is depicted in Fig.2.11b. As shown in the schematic representation in the bottom, the displacement field is the result of the opposite motion of the core and the outer steel layer in opposite phase, thanks to the presence of

the polymer acting as a spring. Looking at the periodic structure as a homogeneous material, this behavior can be interpreted as the presence of a dynamic negative effective mass density in the frequency range of the dip.

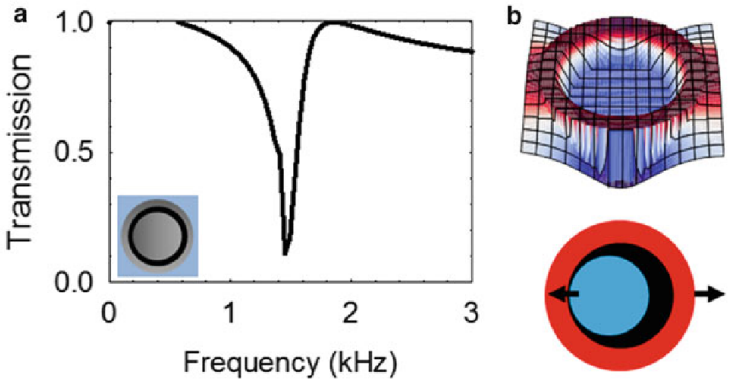

Figure 2.11: (a) Transmission curve by a low resonant phononic crystal. (b) Displacement field computed at the transmission dip frequency and the corresponding representation of the relative mode shape of the unit cell [5].

Another example of local resonators applied in the acoustic field is illustrated in [4] and described in Fig. 2.12. It is considered a circular waveguide to which a periodic series of single branch Helmholtz resonators is connected, as illustrated in Fig. 2.12a. The bandgap is narrow and limited only to the frequency range of the resonator but it is extremely efficient, reaching high attenuation values. As visible in Fig. 2.12b, the imaginary part of the transmission diagram is has non-zero values only in the bandgap region. In the case of Bragg interference, the bandgap is wide and the imaginary part of the transmission is rounded. On the other hand, using locale resonators, the imaginary part of the transmission is extremely sharp and narrow as the bandgap itself.

In the case of LRM, what we called bandgap is now renamed stopband, due to its narrow working frequency range.

Disadvantages of using LRM are related with rather narrow working frequency range and the requirement of heavy resonators to operate in the low frequency range. A further step towards better performances, is to couple Bragg scattering and local resonance to obtain wider bandgaps [121, 122]. Novel bandgap formation mechanism are proposed to ease the practical implementation of such hybrid metamaterials, switching from the multi-phase to the single-phase one [95]. In conclusion, LRM are usually applied for vibration and noise reduction in various applications. For example, they can be added as a subwavelength array of local resonators to a host structure of an automobile dash panel [123] or introduced in panels to create acoustic absorbers [124, 76] .

2.8.3 Modes Separation

D'Alessandro et al. introduced in [6] the concept of modes separation which is used in this work for the original metastructure design. The idea behind it is to exploit global and local modal shapes of the unit cell to open ultra-wide bandgaps at low frequency, thanks to the combination of subsequent bandgaps. The key to apply this method is to carefully engineer the unit cell in order to confine all the elastic modes characterized by the participation of big modal masses (i.e. global modes), in the first passband. From the second on, all passbands are characterized by small participating modal masses (i.e. local modes), in which the movement of structure bigger elements is not involved. Usually, local modes are related with elastic element in the structure that acts as springs and are characterized by the participation of small modal masses. Therefore, they are called deaf modes because they are not perceived on a global level.

The geometry proposed by D'Alessandro et al. is shown in Fig. 2.13. It involves massive spheres linked together by a box-line connection that exploits the flexural stiffness of the beam from which is composed. In addition, spheres move as rigid bodies and, due to their size and mass, vibrate only at low frequencies (in the first passband).

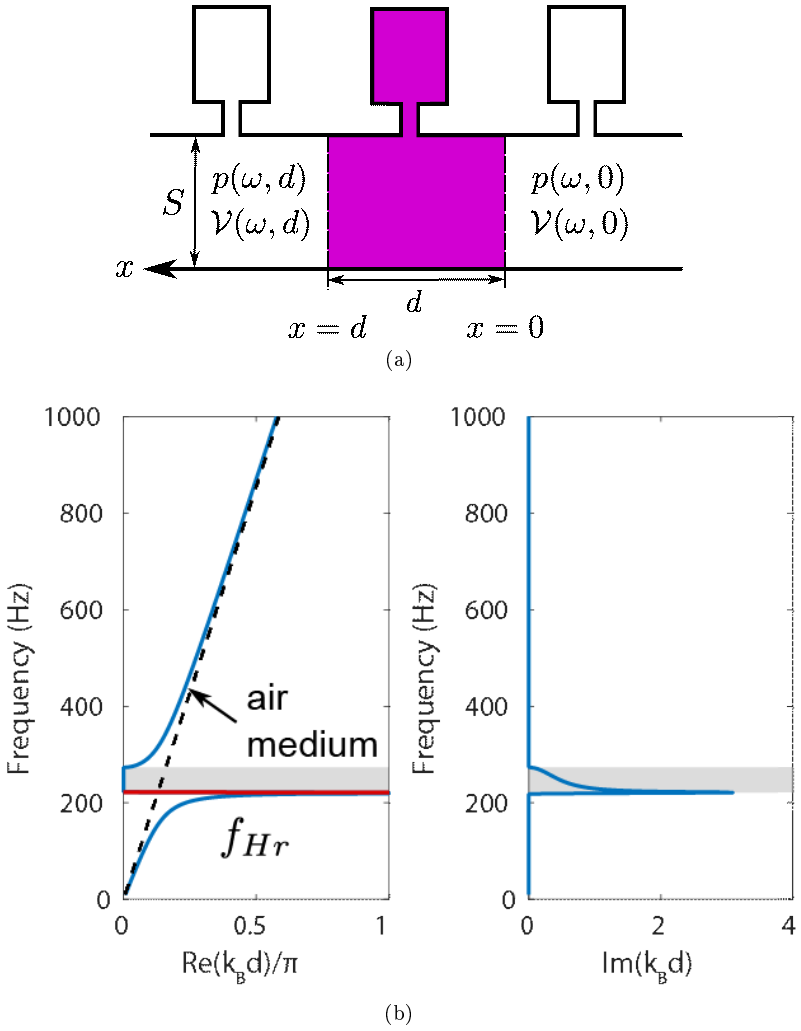

Figure 2.12: Complex band diagram (b) related to a waveguide with periodic side branch resonators in parallel (a) [4].

The numerical band structure for the proposed geometry is shown in Fig. 2.14a. Modes defining each bandgap limit in the band diagram are shown in Fig. 2.14b. The opening mode of the first bandgap is a global mode as it engages the whole unit cell, while all remaining modes are local and involves only connection elements. Therefore, spheres can be seen as lumped masses moving by rigid motion and the box-connection as elastic springs. The modal mass is significantly lower in the case of local modes while the modal stiffness is comparable. Thus, local modes are characterized by high frequency, not involving all the unit cell. The specific organization of global and local modes allows to have bandgap limits which are overstepped in the transmission spectrum. Therefore, they act as a ultra-wide unique bandgap, approaching the behavior of a low-pass mechanical filter.

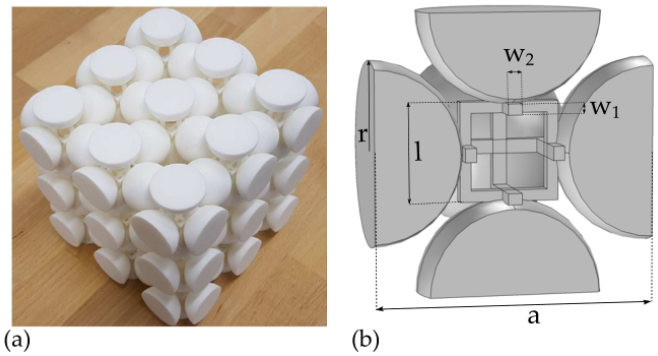

Figure 2.13: Unit cell geometry engineered via modes separation [6].

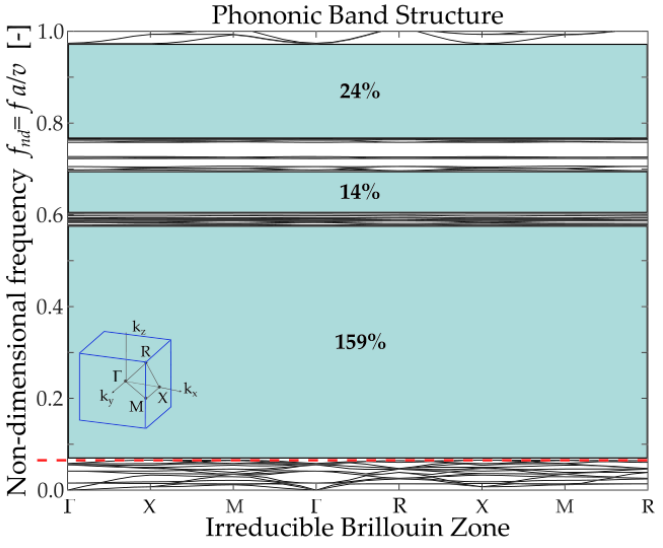

(a)

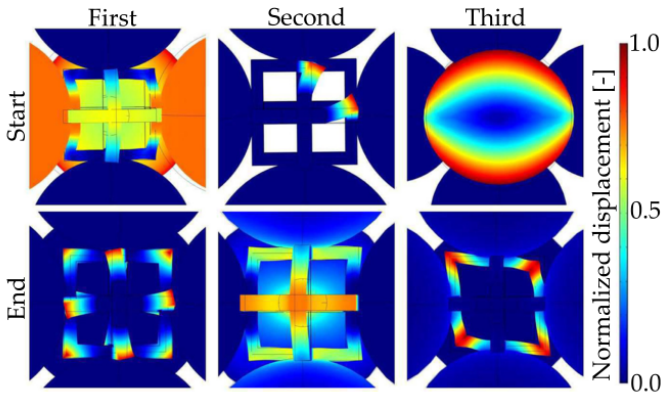

(b)

Figure 2.14: Band diagram (a) and relative bandgap opening and closing mode shapes (b) [6].

Chapter 3

Metastructure design

3.1 Introduction

This chapter introduces the design of a vibrational metastructure targeted to be exploited as a decoupling element for a novel hand-held vibration probe. Initially, the application requirements are framed and the proposed unit cell design is shown. Finite element analysis are carried out to compute the band diagram of the infinite periodic medium and check its performance range as vibration isolation element. Successively, a finite metastructure is chosen as a repetition of the elemental unit cell. Further numerical analyses are performed to verify the structure deformation under static conditions is not excessive and assess the metastructure dynamic behavior with respect to the infinite medium, considering also the material damping.

3.2 Unit cell design

3.2.1 Requirements

The metastructure should meet specific requirements driven by the application in which the vibration probe will be used. The requirements for the specific application case targeted in this thesis are:

1. A wide frequency range (i.e. bandgap) in which wave propagation is strongly attenuated and remains flat along the frequency range of interest, approximately of 10 kHz wide
2. A low bandgap opening frequency (near 1 kHz), still allowing measurement in the low frequency range.
3. A compact and lightweight design to guarantee a comfortable handling.
4. An adequate strength with respect to the application.

Thus, the metastructure acts as a strong insulator for vibrations in the bandgap region.

3.2.2 Unit cell design idea

The design of the proposed unit cell is guided by the mode separation working principle. As such, the idea is to exploit rigid masses connected through flexible components as described in [6].

The proposed unit cell has a lattice constant equal to $a = 4$ cm and its configuration is shown in Fig. 3.1a. It consists of eight masses (colored in blue) connected through connecting flexilble components (colored in orange). In Fig. 3.1b, a close-up view of a quarter of the unit cell is reported for the sake of clarity, while in Fig. 3.1c, the quarter of the unit cell is sectioned to put in evidence the deformable components located inside the mass. They consist of three slanting beams of diameter $s = 1.6$ mm connected one to the others in the centre of the mass and at the corners with the other deformable components of the adjacent quarters. Connections are engineered to be stiff enough to deal with the mass of the structure itself whilst not add excessive weight. Moreover, a proper fillet is chosen between beam connections to prevent stress concentration. In the centre

of the quarter of the unit cell, in proximity of the connection between the four slanting beams (three of them are visibile), additional masses of diameter $d = 4$ mm are designed to further lower the opening frequency of the first bandgap. The unit cell has five symmetry planes: three are parallel to cube faces and located at the middle point of each edge of the unit cell of Fig. 3.1a; the remaining two are on both diagonal directions of a single mass cube (Fig. 3.1b).

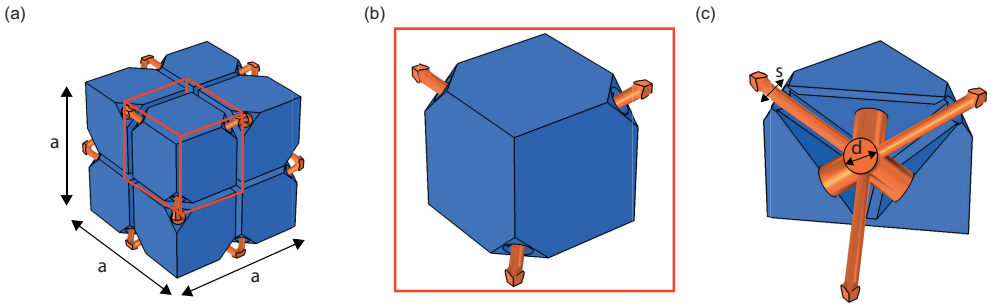

Figure 3.1: (a) Schematic view of the unit cell. (b) One quarter of the unit cell. (c) Sectional view of one quarter of the unit cell. Rigid masses are colored in blue while deformable connections in orange.

The Polyamide PA 2200 is chosen for prototyping the system in Additive Manufacturing (exploiting SLS technology) and then performing experimental tests. This choice was driven to balance production complexity and performance of the system. Material properties of PA2200 are shown in Tab. 3.1. For numerical modeling, the Tensile modulus is equal to 1700 N/mm^2, while a value of 1240 N/mm^2 is chosen for the Shear modulus along with a density of 0.9 g/cm^3. The Poisson ratio is evaluated as $\nu = E/2G - 1 = 0.31452$. Thus, wave speed can be computed as $v = \sqrt{\frac{E}{\rho}} = 1374$ m/s [125].

Table 3.1: Material properties for fine polammide PA 2200 for EOSINT P SLS printers.

PA 2200			
Particle dimension	laser diffraction	60	μm
Density	laser sinterized	0.9-0.95	g/cm^3
Tensile modulus	DIN EN ISO 527	1700 ± 150	N/mm^2
Shear modulus	DIN EN ISO 527	1240 ± 130	N/mm^2

3.3 FEM Analysis

3.3.1 Dispersion Analysis

The bandgap properties of the unit cell shown in Fig. 3.1 has been calculated by a numerical dispersion analysis performed in COMSOL Multiphysics©. Block-Floquet boundary conditions are applied on the six surfaces of the unit cell to simulate the periodic repetition along the three orthogonal directions of the cell in the infinite periodic medium. According to the geometry of the unit cell and to its symmetries, a simple orthorhombic lattice (ORC) arrangement is chosen for the dispersion analysis [126]. The resulting Irreducible Brillouin Zone (IBZ) is shown in the inset of Fig. 3.3a. The mesh used for the eigenfrequency analysis is shown in Fig. 3.2. The maximum element size used is smaller than $\lambda/5$, where λ is the wavelength associated to the highest frequency to be considered (which is equal to 15239 Hz, referring to Fig. 3.3b).

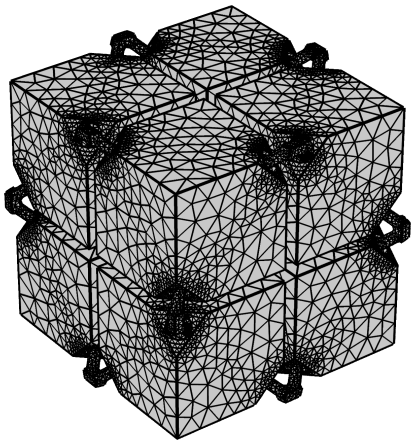

Figure 3.2: Mesh used for the numerical computation of the band structure.

From Fig. 3.3a, it is evident that under the hypothesis of infinite periodic repetition of the proposed unit cell, four wide frequency bandgaps are present. The first bandgap opens at 1478.1 Hz and closes at 5916.8 Hz, the second covers the range of frequencies from 5952.1 Hz to 8654.7 Hz, while the third from 8716.0 Hz to 9625.4 Hz and the fourth from 9827.3 Hz to 15239.0 Hz.

To better investigate the bandgap opening mechanism, in Fig. 3.3b the mode shapes of the opening and closing modes for each bandgap are reported together with their dimensional frequencies. The opening mode of the first bandgap is related to the highest modal mass (thus, involving all the masses of the unit cell), while the others clearly represent local modes characterized by the deformation of connections, as shown in Fig. 3.4. What described so far represents the ideal behavior of an infinite metastructure constituted by a unit cell like the one designed and represented in Fig. 3.1.

The engineerinzation of the component requires a preliminary step, i.e. the assessment of the effects due to moving from an infinite metastructure to a finite one. Thus, it has been decided to start from the minimum number of repetitions that can allow to consider the structure periodic, which is 3, and thus obtaining a drastic reduction of the wave propagation also in the frequency ranges corresponding to the second, third and fourth passbands.

To support such statement, a finite 1x1x3 metastructure, shown in Fig. 3.5, is analyzed numerically in COMSOL Multiphysics©. Thus, its external dimensions are 40 mm x 40 mm x 120 mm.

The final application, as an hand-held vibration probe, will be with the bottom surface mounted on a handler and the system pressed against the structure under testing. Therefore, a fixed constraint is used for the metastructure bottom surface.

3.3.2 Static analysis

Since the workpiece has to be made through additive manufacturing, it is important to check that there are no problems at static level due to its own weight. Therefore, numerical models considering gravity load are carried out for horizontal and vertical configuration of the metastructure. For the simulation, the base surface of the metastructure is assumed fixed. The mesh used for the computation is shown in Fig. 3.6.

The metastructure compression due to gravity load is assessed using a stationary study. The resulting displacement field is reported in Fig. 3.7. The numerical simulation gave as result a maximum stroke of 0.13 mm along the axial direction.

A further evaluation is performed considering the metastructure pressed as it would be in operating conditions, not only on ideal configuration (i.e. properly distributed load on top surface) but also considering an off-center load. The typical preload from DISCOM GmbH is about 10 N, which will be the constant load imposed in the simulations. To test the static performances of the metastructure, three different cases are considered. In the first case, an off-center load is imposed on a single mass of the top surface, resulting in a maximum displacement of13.93 mm in the axial direction. In the second case, the same load is applied on two different adjacent masses of the

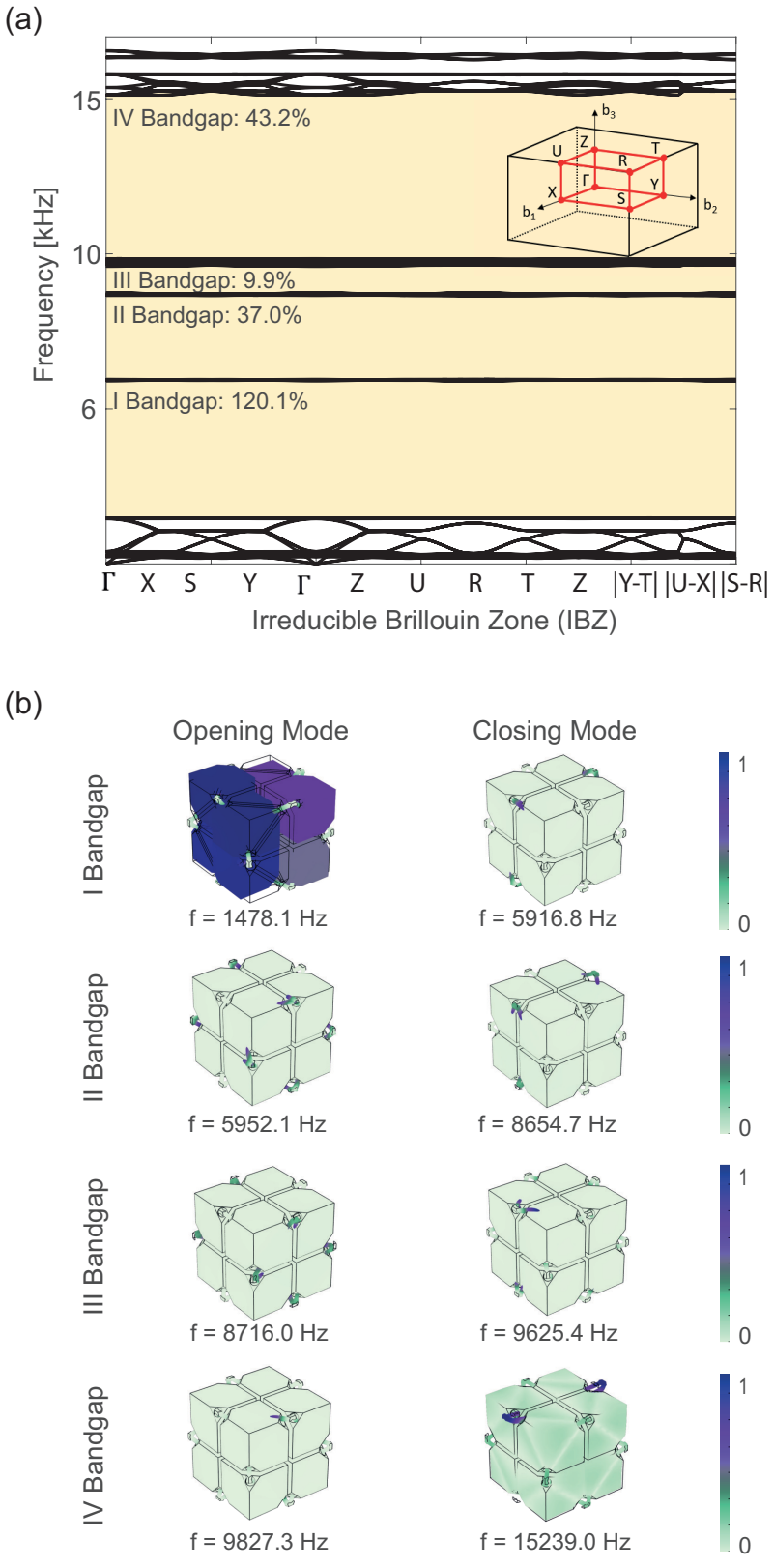

Figure 3.3: (a) Numerical dispersion diagram computed in COMSOLMultiphysics©. The considered Irreducible Brillouin Zone (IBZ) is also provided. (b) Elastic mode shapes (normalized with respect to the maximum displacement) at the bandgaps frequency limits. The symmetry points of the IBZ are not specified since the modes of each bandgap limit present the same mechanical characteristics. The contour of the normalized displacement field is shown in color.

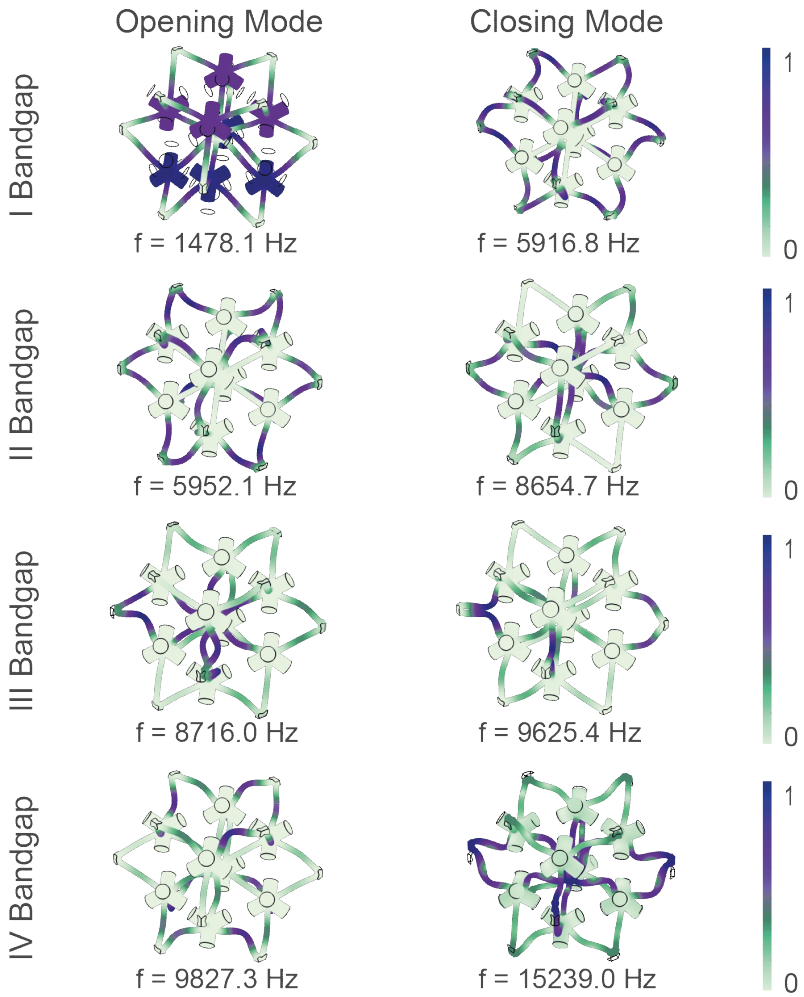

Figure 3.4: Internal beam view of the elastic mode shapes of Fig. 3.3b (normalized with respect to the maximum displacement) at the bandgap frequency limits.

metastructure, obtaining a maximum stroke of 8.87 mm along the axial direction. Lastly, the load is applied on the whole top surface, resulting in a stoke equal to 3.56 mm which is a reasonable value for practical applications.

The maximum bending deflection produced by the gravity load due to its own weight is assessed, the metastructure is clamping as a cantilever beam. The numerical simulation gave as result a maximum bending of 0.81 mm, see Fig. 3.9.

3.3.3 Modal Analysis

A finite element based modal analysis (eigenfrequency method) has been performed by means of COMSOL Multiphysics©, recreating the same constrains imposed on the metastructure for the experimental evaluations. The base of the component is fixed, i.e. the metastructure is clamped on bottom surfaces of the first layer of masses (mimicking double adhesive tape) whilst the rest of the structure is free to vibrate. Computed mode shapes are always in pairs due to the symmetry of the metastructure. The full set of mode shapes, before the bandgap opening frequency, are shown in the appendix B. For simplicity, only one mode shape for each symmetry pair is considered in Fig. B.-1. Eigenfrequencies related with each mode shape are listed in Tab. 3.2.

3.3.4 Vibration transmissibility assessment

A numerical transmissibility analysis is performed on the finite metastructure in COMSOL Multiphysics© to assess its anti-vibrating abilities. The input is applied on the bottom surface of the metastruc-

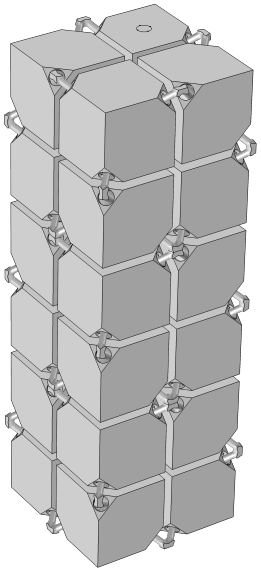

Figure 3.5: The finite metastructure used for vibration isolation purpose.

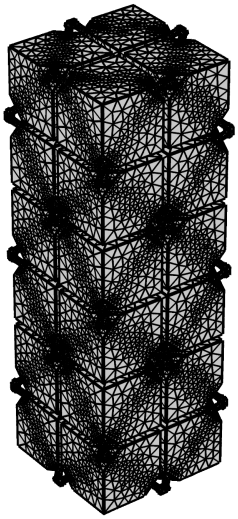

Figure 3.6: Mesh used for the static study, with a average element quality equal to 0.65.

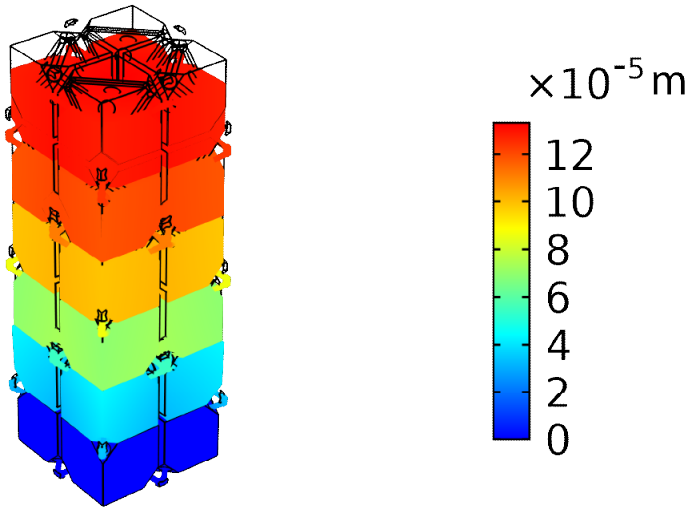

Figure 3.7: Numerical displacement due to the gravity along the axial direction.

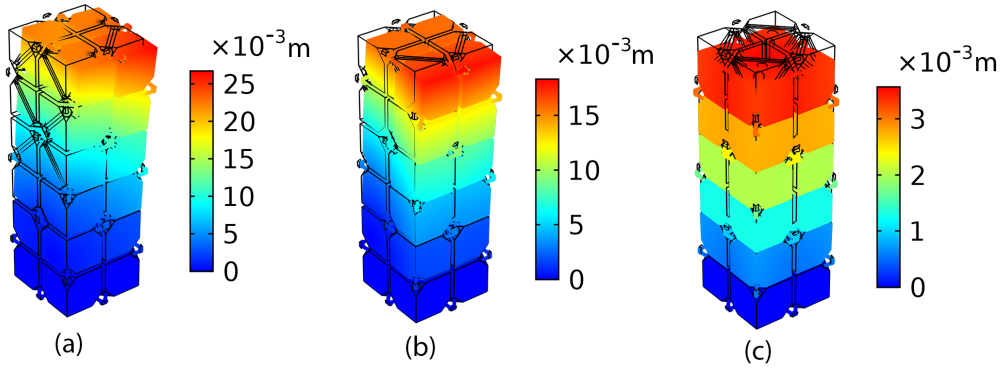

Figure 3.8: Metastructure displacement field due to the superposition of gravity load and surface load of 10 N on (a) only one mass, (b) two adjacent masses or (c) on all four masses.

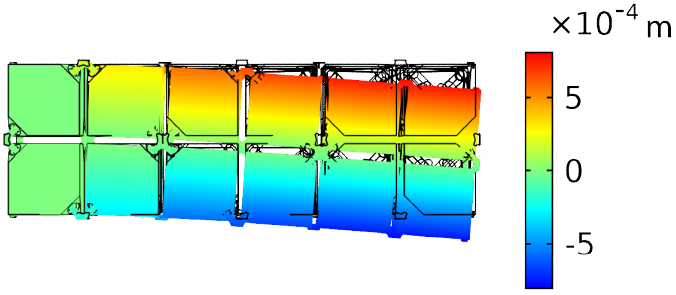

Figure 3.9: Numerical displacement due to the gravity along the load direction.

mode	f_n [Hz]
1	10.411
2	47.902
3	53.628
4	113.73
5	119.05
6	134.26
7	147.79
8	179.95
9	180.5
10	188.24
11	207.04
12	209.24
13	228.42
14	230.69
15	232.16

mode	f_n [Hz]
16	233.84
17	245.85
18	259.16
19	270.52
20	281.04
21	334.23
22	782.72
23	783.29
24	869.33
25	1116.2
26	1235.1
27	1285
28	1352.4
29	1352.8

Table 3.2: Numerical eigenfrequencies from COMSOL Multiphysics©

ture as a prescribed z-axis acceleration, while the output acceleration in z direction is measured on the top surface in a small area as shown in Fig. 3.5, to mimic experimental tests reported in the next section. The transmissibility function is finally computed by dividing the output acceleration by the prescribed input one. No x- and y- displacements of the bottom surface of the metastructure are allowed to mimic the clamped condition we will have in the experiments. The transmissibility functions are shown in Fig. 3.10. The black curve represents the undamped condition.

Theoretical bandgaps computed through the dispersion analysis under the hypotheses of infinite periodic structure are also reported in yellow for comparison in Fig. 3.11. The discrepancies in terms of opening and closing frequencies are due to the finite dimension of the metastructure considered in the transmission analysis and to the boundary conditions imposed on the bottom surface.

According to the results presented in [6], if no material damping is considered, the transmission diagram shows all the passbands expected from the dispersion analysis, but only the first one exhibits a transmissibility higher than 1. Passbands characterized by local modes indeed exhibit three order of magnitude attenuation with respect to the first one since, even if properly excited by the applied input forces, their response is only linked to mass connections and dependent on the number of unit cells that the wave must pass through. The higher the number of unit cell repetitions, the smaller the passband magnitude.

To better reproduce the real behavior of the final 3D printed metastructure, the material dissipation must be considered by introducing a complex Young Modulus in the numerical model. It reads $\overline{E} = E(1 + i\tau\omega)$, where i is the imaginary unit, ω is the circular frequency and τ in [s] is the time constant. This parameter is experimentally identified in [6] on a solid cube of the same material PA2200 (alias PA12) here employed. In our case τ must be tailored properly with experimental data. In fact, nonlinearities introduced by the geometry itself (i.e. small slanting beam diameter) and material dissipation must be considered. Therefore, a sensitivity analysis on the τ parameter is performed, obtaining results shown in Fig. 3.10. Hence, a value of $\tau = 3$ μs is chosen as a first approximation. The final transmissibility diagram thus obtained is superimposed in red on the undamped case in Fig. 3.11. As expected, passbands corresponding to local modes, i.e. around 6 kHz and 9 kHz, disappeared from the transmission diagram, thus proving the proposed design strategy.

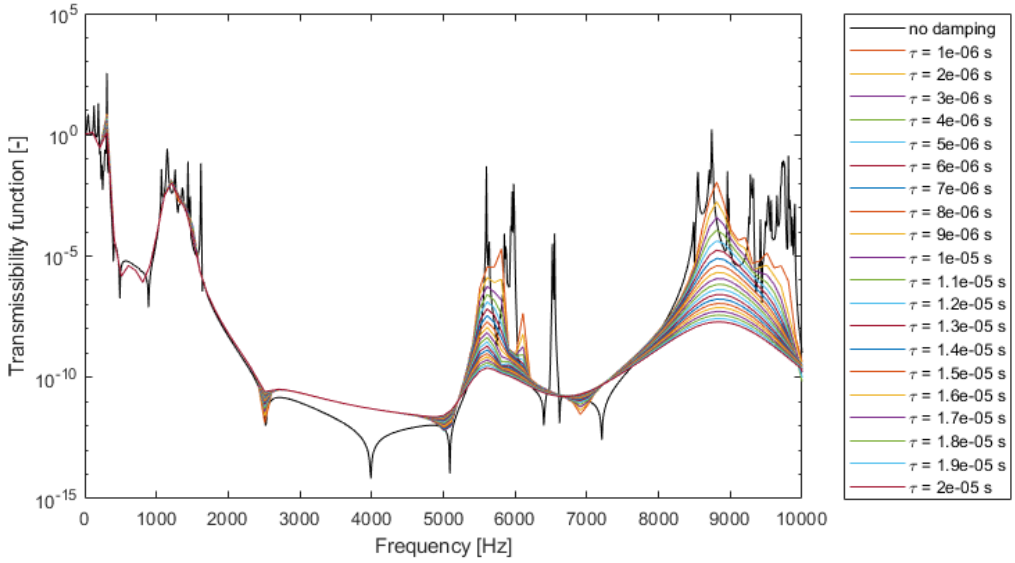

Figure 3.10: Comparison between numerical transmission diagram computed in COMSOL Multiphysics© over τ parameter and experimental data.

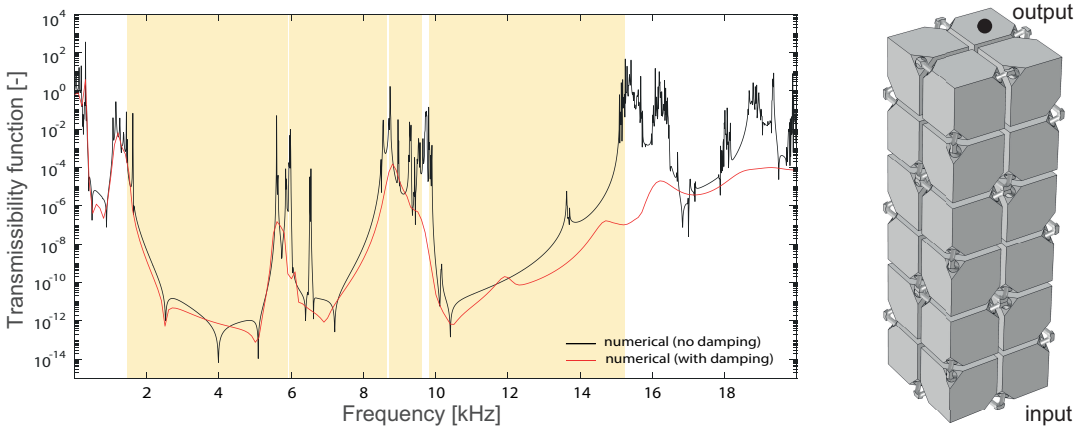

Figure 3.11: Numerical transmission diagram computed in COMSOL Multiphysics©. Theoretical bandgaps computed through the dispersion analysis are reported in yellow for comparison. A schematic view of the 1x1x3 metastructure is also reported for the sake of clarity.

Chapter 4

Metastructure design validation

4.1 Introduction

A preliminary prototype of the metastructure made by 1x1x3 unit cells is manufactured through a Selective Laser Sintering (SLS) process in Polyamide PA 2200 (alias PA12) [127]. SLS is an AM technique which exploits a laser as power source to locally melt and sinter powder material, typically nylon or polyamide. The laser aims at points defined in space by the 3D geometry model, binding the material together layer-by-layer and creating a solid structure. Its limits are mainly related with technology resolution, which is in the order of the tenth of a millimeter, and process thermal energy dissipation, which lead to unwanted deformation mostly relevant in slant structures. Therefore, the minimum diameter of a rod to be printed without flaws is in the order of 1 mm. It is worth mentioning that the diameter of the slanting beams is chosen accordingly to this constraints imposed by the SLS technique.

Experiments are then carried out to initially verify the metastructure static and dynamic performances. Thereafter, another set of 9 specimens are produced by SLS in the same batch to evaluate the manufacturing process uncertainty.

4.2 Dimensional characterization

The company that manufactured the components ensures a tolerance of ± 0.2 mm for a dimension up to 50 mm, ± 0.3 mm for a dimension up to 100 mm and 0.3% for dimensions greater then 100 mm. The previous values should take into account the uncertainty related to all printing parameters (from laser and geometric factors to material properties [128]). A crucial aspect referred by the manufacturer is the component shrinkage due to its non-uniform cool-down, from sample top to bottom, even dependent on its position on the printing bed.

4.2.1 Preliminary dimensional assessment

Standard dimensional measurements by caliper (Mitutoyo Digimatic ABS AOS 0-150mm, resolution 0.01 mm, uncertainty ± 0.02 mm) are taken on the first metastructure sample. During a preliminary measure, the height on the z-direction of cubes (which form the unit cell, numbered in Fig. 4.1) are assessed, highlighting a trend in the printing process. The procedure is then repeated on each metastructure, in this case, measuring not only cubes height (z-direction) but also cubes width (x-y direction) and slanting beam diameter, as previously done, along metastructure z-direction (i.e. along 6 numbered metastructure planes of Fig. 4.1). Results are shown in Fig. A.1 in the appendix A. Comparing measurements for different specimens, a decreasing (or increasing, in the case of flipped metastructure) trend for the cube height is present that requires further evaluation. Cube measurements in the x and y-directions are nearly constant along longitudinal metastructure direction, with low dispersion around the mean value. In addition, they are remarkably different from height measurements from the first chart. It seems that the printing process is more accurate in the (x,y) plane then on the z-direction. Lastly, diameter measurements seem to follow an alternating trend due to their printing direction (45 degrees inclination from cube

planes, following its diagonals). Dimensional tolerances declared by the manufacturer (0.3 mm) are verified in the majority of dimensional tests.

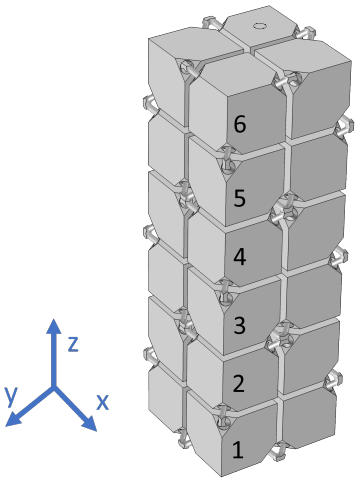

Figure 4.1: Reference system associated with the metastructure and cube enumeration.

To confirm the initial trend evidence, a study of measurement repeatability on the metastructure is carried out. Numbered cubes are measured 50 times each, leading to a sample of 300 measurements. The related histogram, with a bin width equal to 0.02 mm, is plotted in Fig. 4.2. Considering all collected data, the average cube height is 18.18 ± 0.14 mm with a coverage factor 2. The resulting data appears to be fitted effectively by a bimodal distribution instead of a normal one, due to the presence of printing defects. In fact, comparing the frequency distribution of each measured cube in Fig. 4.4, it can be noticed that cubes samples 5 and 6 are shifted towards lower height values with respect to others. Thus, cubes on the metastructure base are different with respect to the ones at the top. This observation is confirmed by the chart of Fig. 4.3, in which all frequency distributions are superimposed. Ultimately, mean and standard deviations for each measurement sample are reported in Tab. 4.1 verifying the accuracy claimed by the manufacturer.

Table 4.1: Measurement repeatability for each numbered cube. Mean and standard deviation with a coverage factor of 2 are computed.

	μ [mm]	σ [mm]
cube 1	18.24	0.06
cube 2	18.24	0.06
cube 3	18.21	0.06
cube 4	18.20	0.07
cube 5	18.11	0.06
cube 6	18.07	0.04

Table 4.2: Measurement repeatability for each numbered cube for all 10 metastructure specimens. Mean and standard deviation with a coverage factor of 2 are computed.

	μ [mm]	σ [mm]
sample 2	18.21	0.07
sample 3	18.19	0.10
sample 4	18.19	0.08
sample 5	18.18	0.07
sample 6	18.20	0.13
sample 7	18.20	0.11
sample 8	18.17	0.07

sample 9	18.20	0.09
sample 10	18.20	0.05

So far, all evaluations are carried out on a single metastructure. Further analysis are necessary to assess the reproducibility of the SLS printing process over different specimens. Caliper measurements of cube heights are done over all cubes on each side of the metastructure for each of the remaining 9 specimens. Thus, 48 measurements are obtained for each metastructure (6 cubes for each column times 2 column for each metastructure side times 4 sides). Histograms obtained for the 9 metastructure samples printed in a batch are shown Fig. 4.5 and related statistical indicators are presented in Tab. 4.2. Data seems to be less affected by the bimodal behavior characterizing metastructure sample 1. Finally, data from all specimens is aggregated and presented in the histogram of Fig. 4.6. The overall mean value is equal to 18.19 ± 0.10 mm for cube height, with a coverage factor of 2, ensuring again dimensional tolerance conformity with manufacturer specifications.

The same evaluations are done for slanting beam diameters. Measurements by caliper are taken on 7 different beams on all four sides of each metastructure, as shown in the representation of Fig. 4.7. Thus, a total of 28 measurements are taken on each sample (7 diameter evaluations times 4 metastructure sides). Resulting histograms are shown in Fig. 4.10 and related statistical indicators are indicated in Tab. 4.3. Manufacturer specifications are verified also for the diameter of the slanting beams, which is a crucial parameter for the dynamic performance of the metastructure. Data from all specimens is then collected and plotted in the histogram of Fig. 4.8. The bimodal distribution found in Fig. 4.2 is present in the case of slanting beams as depicted in Fig. 4.9. The contribution made by each sample to this behavior is shown in Fig. 4.9. Lastly, the overall mean value is computed with the related uncertainty and it is equal to 1.60 ± 0.13 mm for the slanting beam diameter.

Table 4.3: Diameter measurement for metastructure sample.

	μ [mm]	σ [mm]
Sample 1	1.57	0.15
Sample 2	1.59	0.11
Sample 3	1.63	0.10
Sample 4	1.61	0.12
Sample 5	1.61	0.14
Sample 6	1.61	0.12
Sample 7	1.58	0.14
Sample 8	1.60	0.14
Sample 9	1.59	0.13
Sample 10	1.59	0.12

Mean values are cents off the nominal diameter value of 1.6 mm while standard deviations are all within manufacturer dimensional tolerances (0.3 mm). The latter is verified even if considering all measurement population (normal fit shown in Fig. 4.8), obtaining a diameter value of 1.6 ± 0.26 mm.

4.2.2 Computed Tomography evaluation

The metastructure developed is characterized by a complex hollow geometry of slanting beams connected together with the remaining structure. Thus, there is the need to inspect interior parts of manufactured specimens. It is necessary to assess if cavities were free from dust eventually left by the manufacturing process. The measurements have been performed by using a CARL ZEISS METROTOM OS Computer Tomograph. Reconstructions were then processed in CALYPSO 2019 software developed by CARL ZEISS.

The scan take 2050 slices (excluding the black reference ones). Voxel resolution is 70.67 μm while the focal spot size is 70 μm. Due to metastructure attitude to vibrate while being moved, 3 averages have been performed for each slice, leading to an acquisition time of 3 seconds each. A

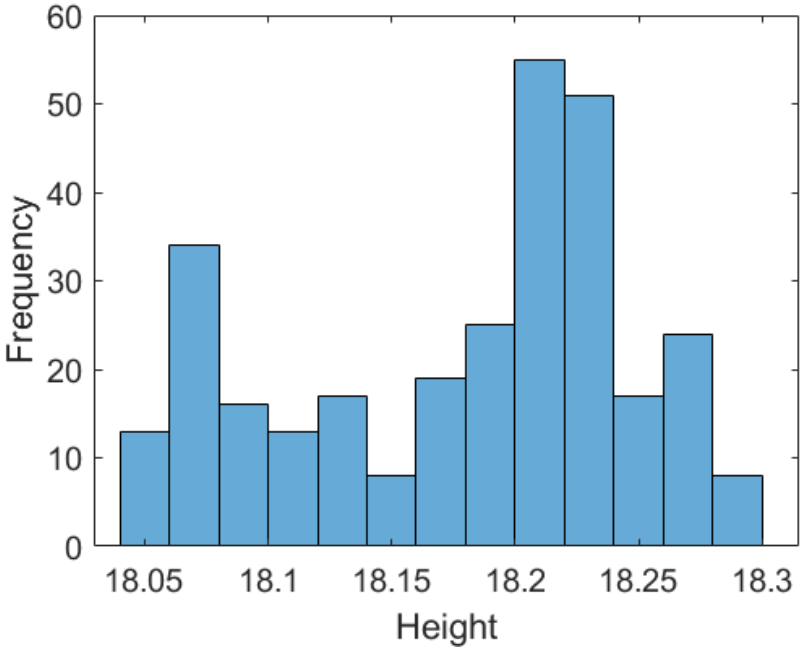

Figure 4.2: Frequency distribution for cubes heights along metamaterial z-direction.

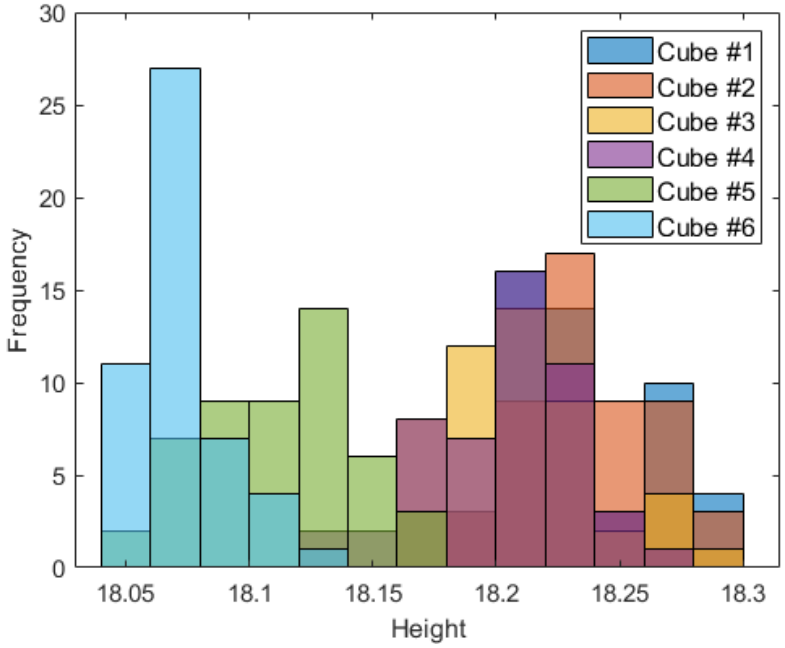

Figure 4.3: Superposition of frequencies related to each cube height for the sample 1.

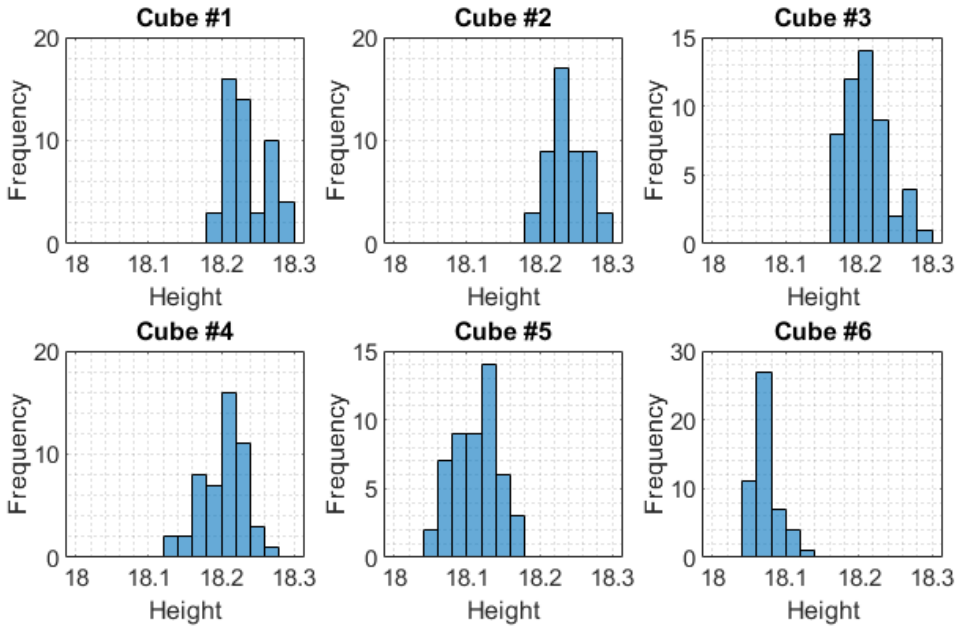

Figure 4.4: Frequency distribution for each cube along metamaterial z-direction for the sample 1.

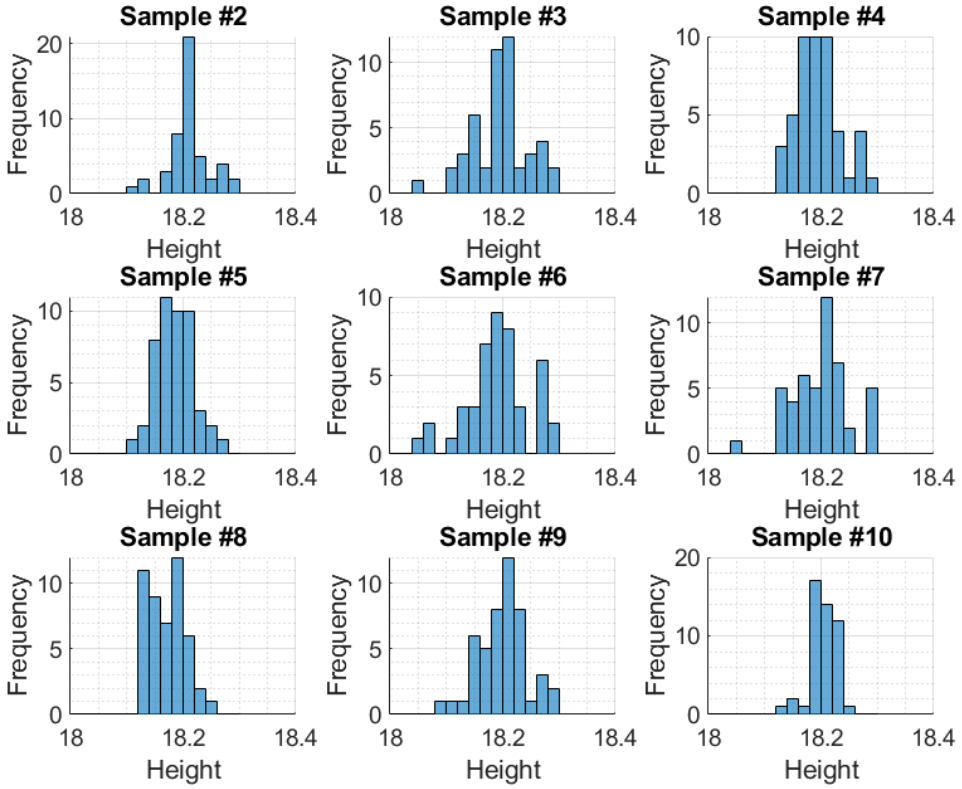

Figure 4.5: Frequency distribution for cubes heights along metamaterial z-direction for each remaining sample.

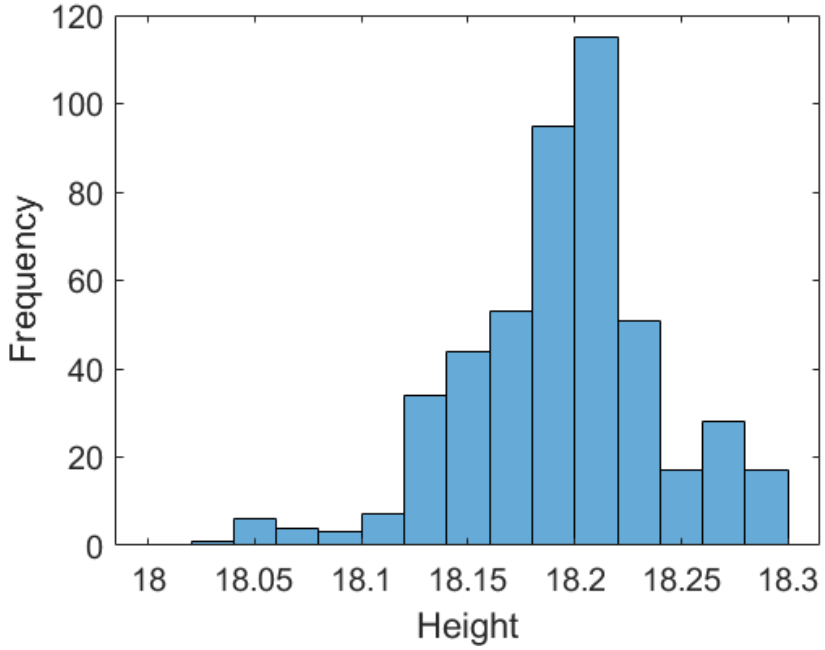

Figure 4.6: Frequency distribution for cubes heights along metamaterial z-direction merging data from all samples.

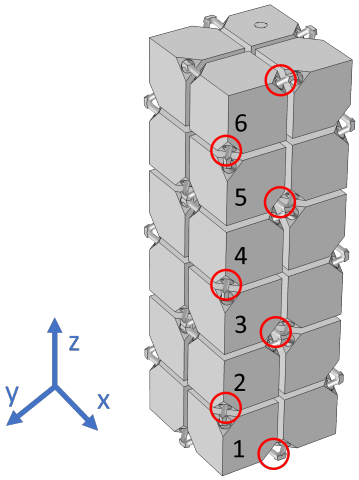

Figure 4.7: Reference system associated with the metastructure and cube enumeration. Measured diameters are highlighted in red circles.

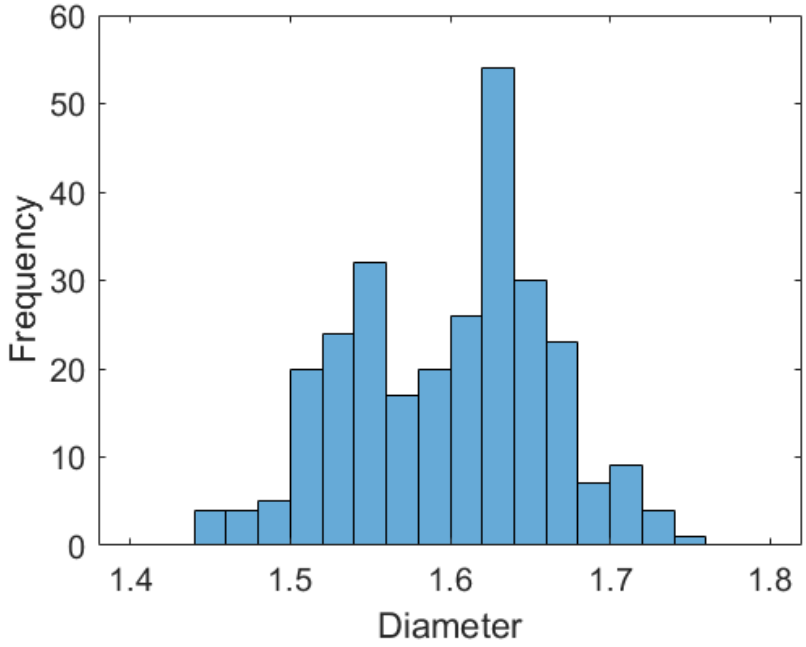

Figure 4.8: Normal distribution fit for the diameter of slanting beams considering measurements on all samples.

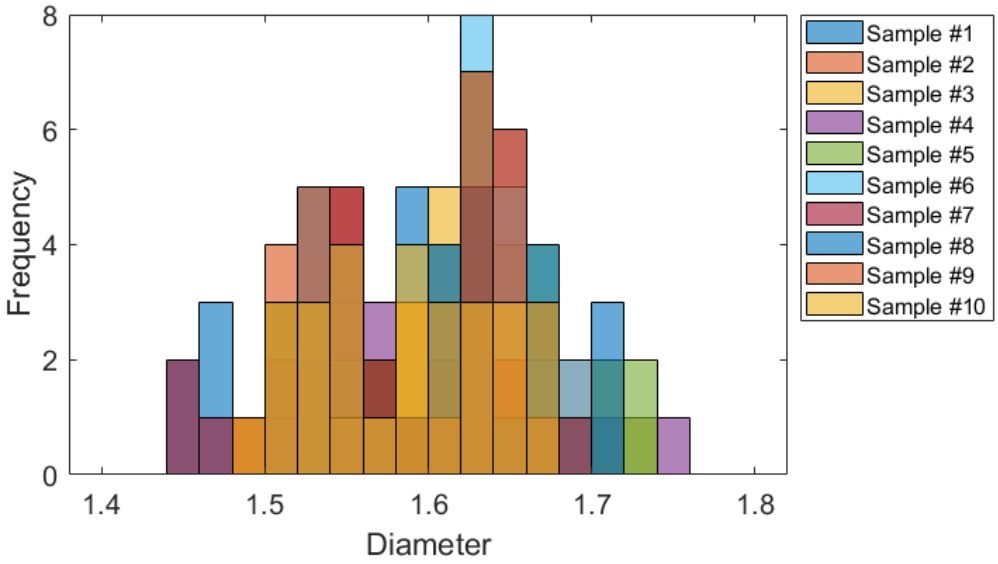

Figure 4.9: .

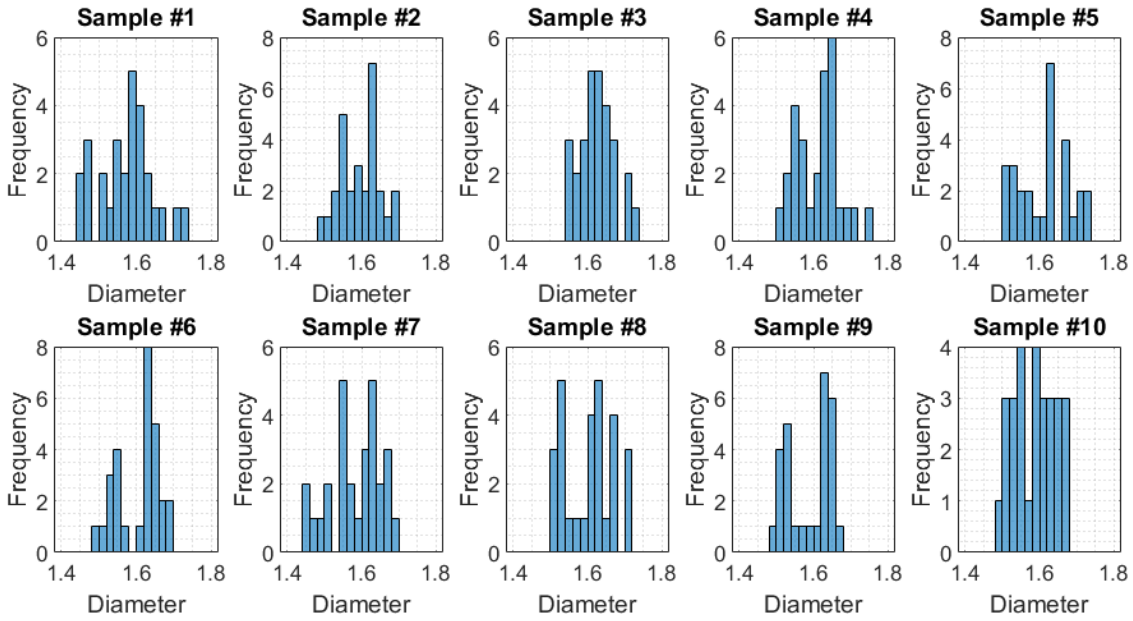

Figure 4.10: Normal distribution fit for the diameter of slanting beams measured on each sample.

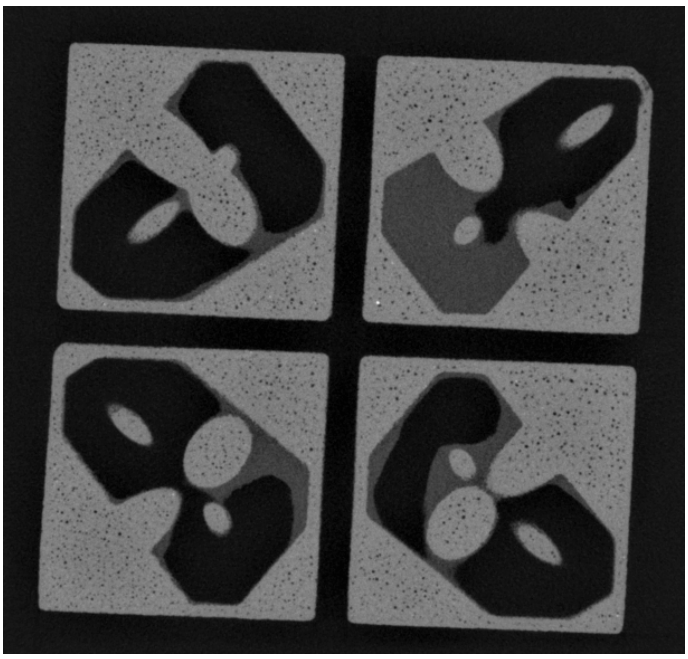

Figure 4.11: Example of a slice obtained from the tomographic reconstruction. Black areas correspond to air, lighter areas to PA 2200 print and gray areas to remaining dust.

copper filter of 0.25 mm is mounted on the X-RAY source for the scan. The acquisition time for each sample was 2 hours and 33 minutes.

A preliminary measurement was performed on the first metastructure sample after the initial cleaning by compressed air. The complexity of the metastructure makes internal inspection impossible, thus a X-RAY reconstruction of the specimen allows proper quality analysis. By observing the slice of Fig. 4.11, it is evident that pressed powder, left by the manufacturing process, is internally present. Thus, a further clean up is needed to allow the metastructure to work as intended. Subsequently, to assess the degree of cleanliness obtained, the tomographic measurement is repeated and dust removal is verified. In addition, looking at bulk parts of the metastructure, the visible porosity is caused by the printing process itself.

nature of the PA 2200 material emerges,

Thereafter, a tomographic computer scan is performed for each sample printed in a batch with the same settings. From the visual inspection of the slices it can be deduced that, in most cases, residual dust is present. It would not have been possible to verify it without a X-RAY analysis. Representative tomographic slices for each sample are shown in the appendix D. .

4.3 Static characterization

In order to measure properly, the accelerometer installed on the tip of the vibration probe, described in Section 2.2, needs to be in contact with the testing surface during the measurement and, thus, need to be pushed with a certain axial preload. Therefore, to determine the level of preload needed for the metastructure not to go in bundle, it is necessary to carry out a preliminary analysis, which will then be verified with a static test. During the compression test, reaction forces, i.e. preloads, are measured at different imposed displacement values.

Experiments have been carried out using a MTS810 material testing system, equipped with a MTS force transducer model $661.22D-01$ with a load capacity of 250 kN. During the test, the metastructure has undergone one load/unload cycle, the displacement speed was equal to 0.01 mm/s.

Test results are shown in Fig. 4.12. The evident slope changing around 8 mm of displacement is due to the bundling of the masses of which the metastructure is composed. In fact, in the interval with lower slope only the slanting beams take charge of the deformation, while the masses behave as rigid elements. Increasing the displacement, the masses come into contact and thus the metastructure starts to work as a bulk. Moreover, hysteresis is present in the force-displacement curves and it is caused by the intrinsic viscoelastic behavior of the material.

4.4 Numerical model updating

For the evaluation of the metastructure performances by means of transmissibility simulation, the printing material (PA2200) is considered as linear elastic to simplify numerical modeling. Initially, mechanical parameters specified by the manufacturer, shown in Tab. 3.1, are used. Having performed the static characterization of the metastructure, the elasticity modulus can be retrieved from the force-displacement curve for the specific sample.

Fixing the Poisson ratio value, Young Modulus can be estimated from the linear fit shown in Fig. 4.13 of the compression data in the range between about -4.8 mm and -7.5 mm. This interval is chosen considering the data which is less noise-affected, before the slope changing due to metastructure bundling. In fact, when measuring small force variations, as in this case, results can be less accurate due to instrument amplitude resolution.

The slope, i.e. the metastructure stiffness, found out from the linear fit is 2.44 $[N/mm]$. To retrieve the Young Modulus, as a first approximation (i.e. not considering more complicate structural analytical models), a static compression simulation of the metastructure has been carried out with a E equal 1 $[MPa]$ and a preload Δz of 1 mm. A coefficient relating the metastructure stiffness and the Young modulus of the material can be computed from the surface reaction force $F_z = -0.0018$ $[N]$ where displacement has been applied. Overall stiffness can be computed as $K = F_z/\Delta z = k_E E$, thus $E = 1352 \pm 32$ $[MPa]$ (with 95% confidence interval on linear fit). To confirm the value retrieved from the former approximation, a numerical model of the displacement-controlled compression test is carried out, employing the same displacement range

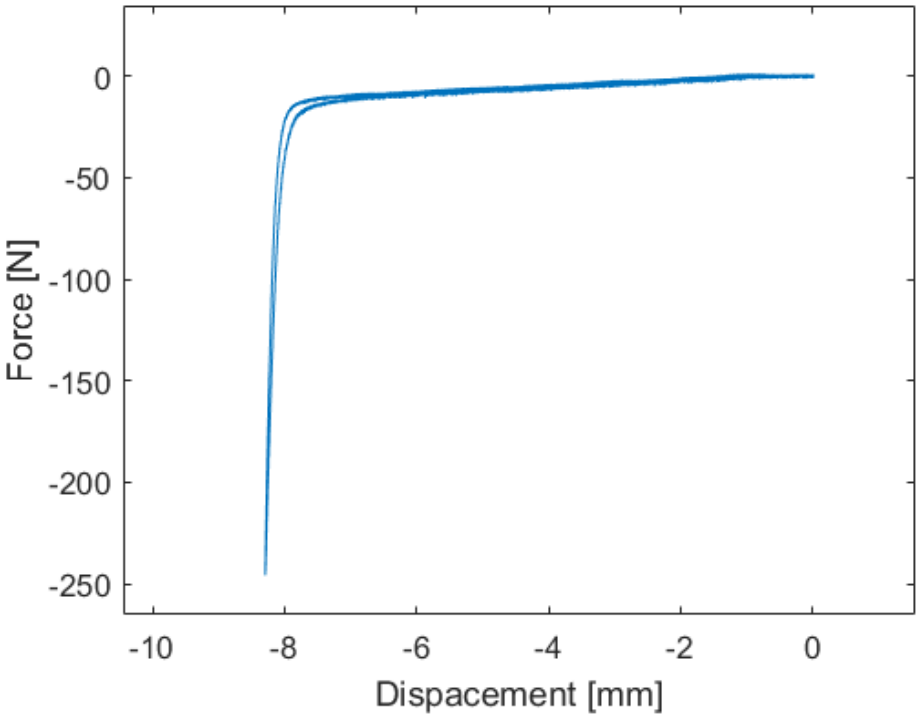

Figure 4.12: Compression test results using MTS810 testing machine.

used for the linear fit of Fig. 4.13, obtaining force as the reaction force on the upper boundary. Force-displacement curves for a spectrum of Young Modulus values are obtained with their relative slopes. For a stiffness value of 2.44 $[N/mm]$, retrieved experimentally, the associated numerical Young Modulus is included between 1350 and 1360 $[MPa]$, upholding the initial assumption. Therefore, the Young modulus experimentally retrieved is approximately 20% smaller compared to the initial value from the datasheet. Both numerical transmissibility curves, computed with Young modulus from datasheet and the updated one, and experimental data are show in Fig. 4.14. A much better match with experimental data is clear observing the red curve plotted in 4.14a. The small peak present at 5145 Hz in the experimental data of Fig. 4.14b, due to local modes of the metastructure, is picked properly after model updating. As already done previously, a complex modulus is used in the numerical model to get closer to the real behavior of the metastructure. A sensitivity analysis on the τ is carried out to choose the optimal value. Results are shown in Fig. 4.15. Moreover, density can be retrieved from mass and volume of the first metastructure specimen. The mass value is 92.3 g with 0.01 g accuracy. The metastructure volume can be estimated importing the point cloud obtained by computer tomography in the MeshLab software 90.7375 mm^3. Density value for the selected sample is around 1 g/cm^3, which is in good agreement with manufacturer datasheet. Performing the same procedure over all 10 specimens and averaging the resulting values, we obtain an average density of 9.75 g/cm^3 with a standard deviation of 0.02 g/cm^3. Uncertainties in density estimation are related to the presence of dust remains in the samples. This cause primarily the presence of an additional weight to be considered. Secondly, it creates issues when the point cloud is imported in MeshLab open source software. In fact, surfaces defining the edges of the metamaterial are not sharp, resulting in a less then optimal volume reconstruction and estimation.

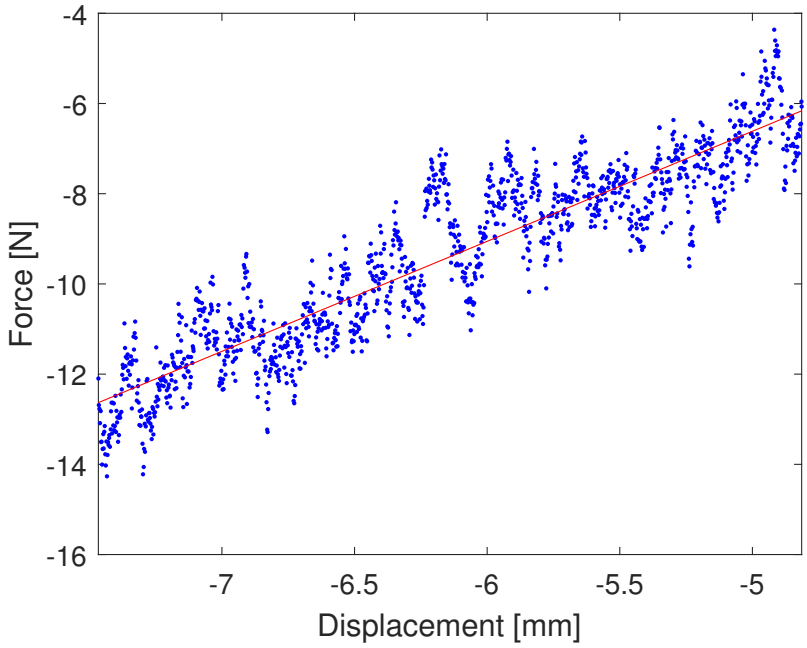

Figure 4.13: Linear fit for the compression data before the metastructure gets full packed.

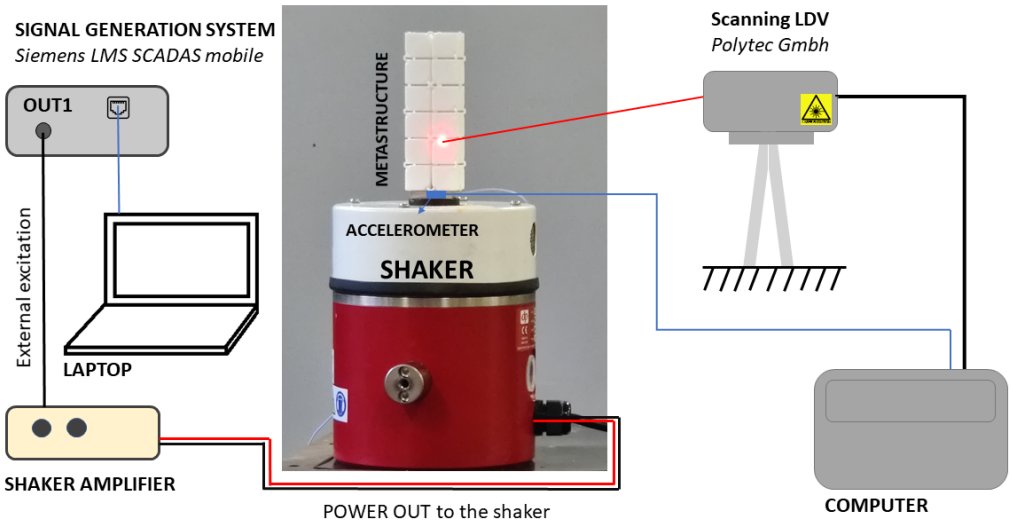

Figure 4.16: Experimental setup for experimental modal analysis with scanning laser Doppler vibrometer and reference accelerometer.

4.5 Dynamic characterization

4.5.1 Deflection shapes measurement by SLDV

The scanning laser Doppler vibrometer (SLDV) allows to perform an analysis of the Operational Deflection Shapes (ODS) of a structure. This technique allowed us to determine the ODS of the metastructure when placed in vibration. ODS have been measured by performing a scanning on the side and on the top of the metastructure.

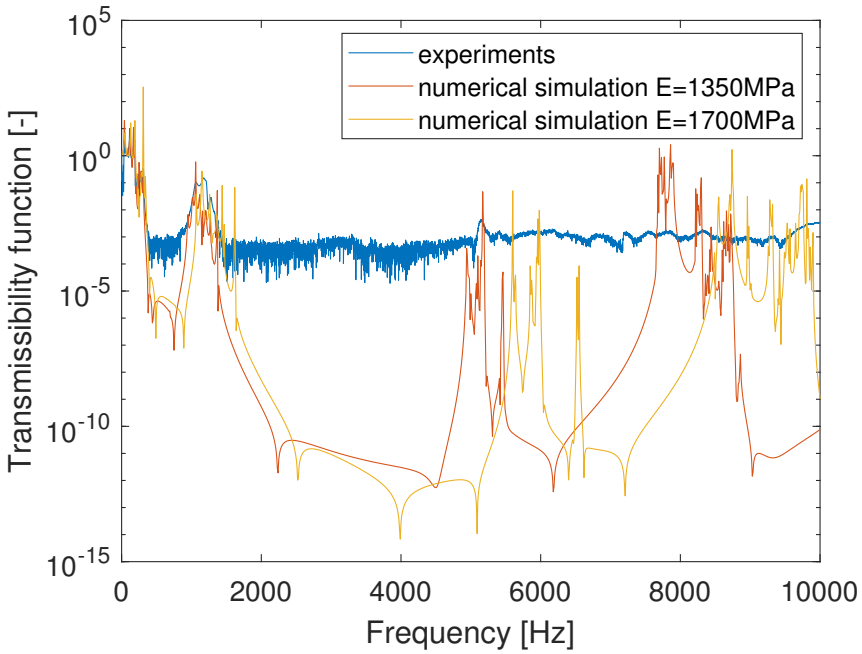

(a) Close up on the low frequency range.

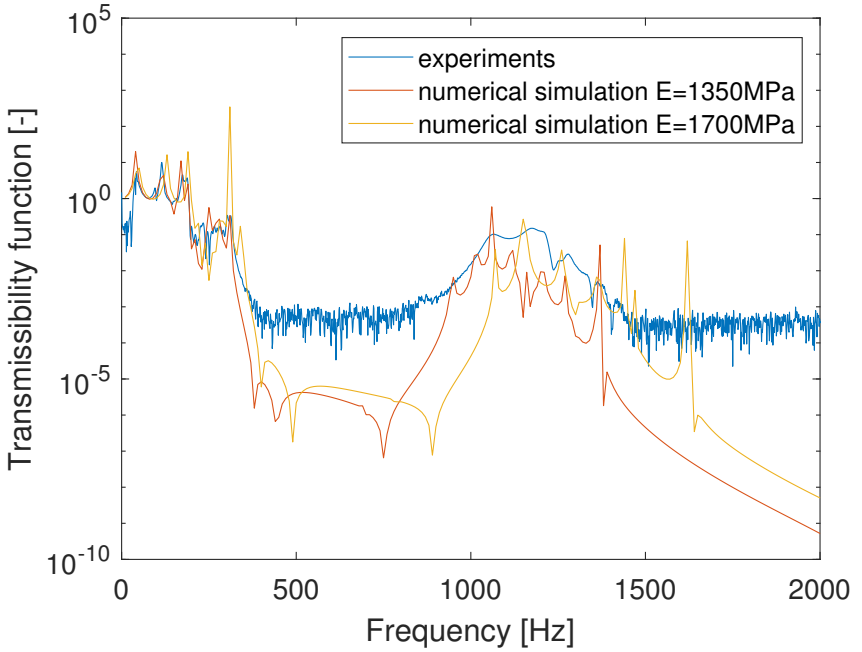

(b) Comparison between numerical and experimental transmissibility function in the whole frequency range.

Figure 4.14: Comparison between numerical and experimental transmissibility function, after Young modulus parameter updating.

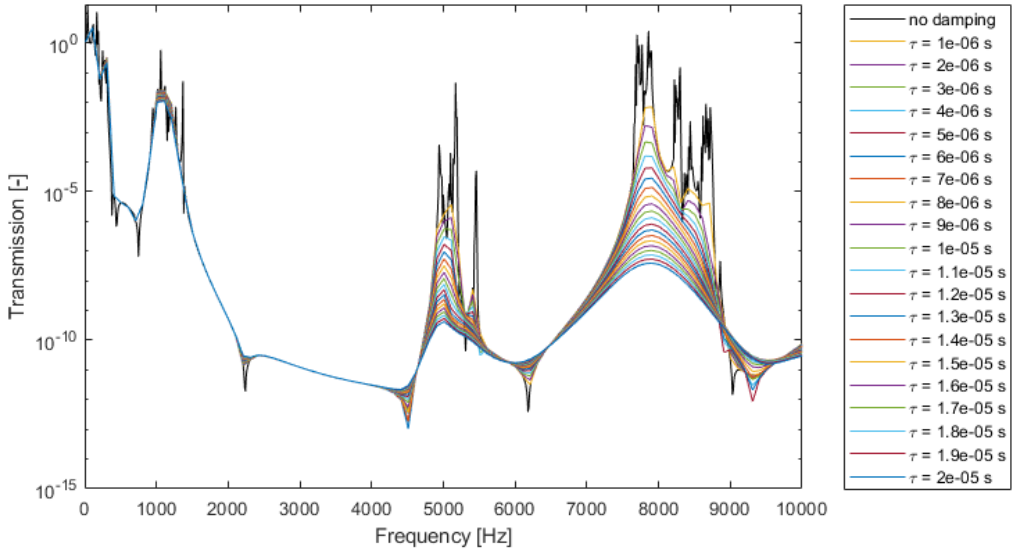

Figure 4.15: Comparison between numerical transmission diagram computed in COMSOL Multiphysics© over τ parameter and experimental data. A τ equal to 3μs is chosen.

The employed test setup is presented in Fig. 4.16. The metastructure is mounted with double adhesive tape on the plate of the electrodynamic shaker (Data Physics V20), to recreate experimentally the same constraint used for numeric simulations and to allow a proper excitation. A miniaturized accelerometer (PCB model 352C23 with a sensitivity equal to 5.39 mV/g [129]) is then mounted on the electrodynamic shaker plate (and is solid with it) as reference signal to evaluate a transmission function, which would be namely m/s (velocity measured by the SLDV) over m/s^2 (acceleration measured by the reference accelerometer). To scan the top and the side of the structure, a Polytec OFV 055 scanning head with the relative OFV 3001 S controller is employed; acquisition parameters are listed in Tab. 4.4. A custom grid is drawn for both top and side faces of the metastructure.

In the former case, a grid of 248 points, shown in Fig. 4.17a, is employed. In the latter case, 405 points are used in the grid shown in Fig. 4.17b (spatial grid resolution is adequate to solve mode shapes of interest). Lastly, the electrodynamic shaker excites the structure in the band 2 $Hz - 20\ kHz$. Transmission function between the vibrometer response (velocity) and the reference accelerometer (acceleration) are saved as well as spectrum. Even if the transmission is not a frequency response function (we do not measure the input force, but only the acceleration at the shaker plate), modal analysis can be performed due to the phase reference of the accelerometer. The aim of this experimental campaign is to assess the dynamic behavior of the metastructure under known conditions, without focusing on magnitudes but on modal parameters, exploiting modal analysis algorithm (i.e. PolyMAX).

The main issue related with the use of a laser Doppler vibrometry is the quality of laser beam signal return after impacting on the sample. In the specific case, the PA 2200 material, from which the metastructure is fabricated, is opaque. The laser beam impacting on the metastructure surface is transmitted in the sample and illuminated, yielding to a low signal return, not sufficient for measuring. Therefore, a glass powder is glued on target surfaces to enhance beam diffusion and signal return. The added powder has a negligible mass compared to the metastructure itself.

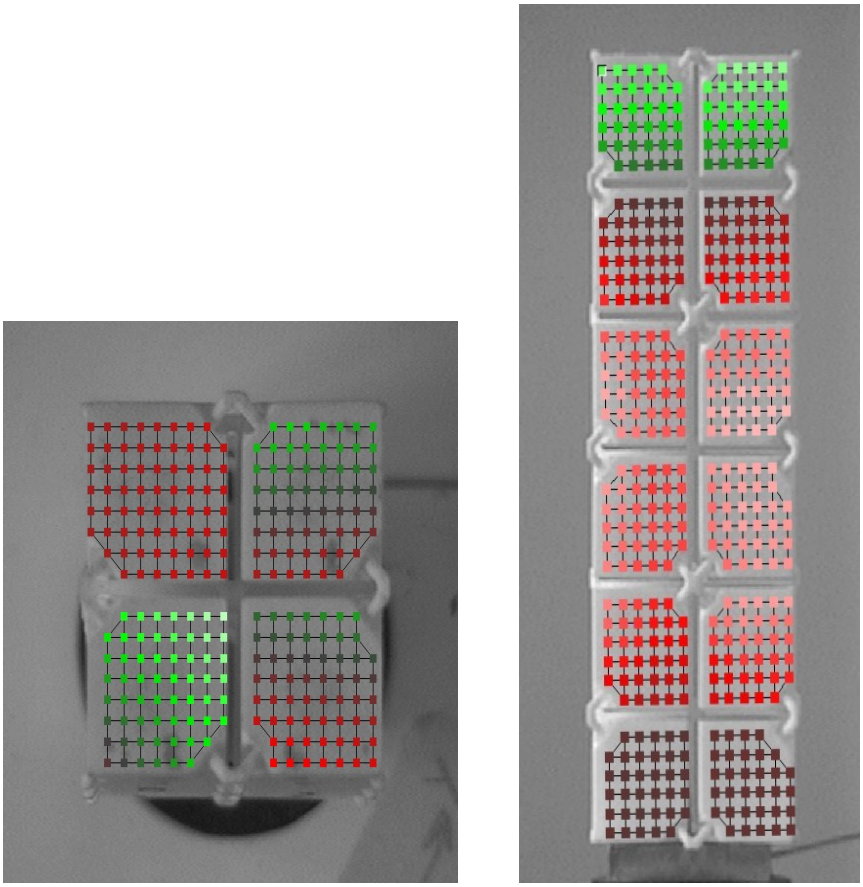

(a) Scanning grid of the metastructure top face composed by 248 points. Color scale referred to preliminary peak picking analysis, showing one of the computed operational deflection shapes.

(b) Scanning grid of the metastructure side face composed by 405 points. Color scale referred to preliminary peak picking analysis, showing one of the computed operational deflection shapes.

Figure 4.17: Scanning grid for SLDV measurement campaign.

Looking at experimental transmission of Fig. 4.20, the designed metastructure has a relevant amplitude only in the first (from 0 to approximately 310 Hz) and second (from 900 to approximately 1420 Hz) transmission bands due to its engineered design. The second one itself has a lower magnitude with respect to the first. The high amplitude peak related to the first transmission band cause the saturation of the vibrometer demodulator, resulting in a strong noise base and hiding global modes of the second transmission band. Therefore, an additional analysis is carried out shrinking the excitation band to 614 Hz to 10240 Hz. This expedient allows to excite properly and retrieve modes on the second transmission band in a better way. It can be pointed out that we are performing modal analysis on a function which is a ratio between two response signals from the vibrometer and the accelerometer. A comparison between the transmission functions sum and the average velocity spectrum is shown in Fig. 4.18. There is no relevant frequency shift between the curves, meaning a proper estimation of natural frequencies. I should like to draw attention to the fact that data have different measurement unit and scales in the figure are properly chosen to make the two curves easily comparable. The present offset is only caused by y-axis scaling.

Table 4.4: Scanning laser Doppler vibrometer equipment used in the measurement campaign.

Vibrometer	Polytech OFV 055
Controller	OFV 3001
Sensivity	5 $\frac{mm/s}{V}$

Tracking Filter	Fast
Averages	16
Bandwidth	5000 Hz
Freq. Res.	0.78125 Hz
Spectral Lines	6400
Windowing	Hanning

Experimental Modal analysis

Modal analysis is then performed on transmission functions using PolyMAX algorithm for natural frequency and mode shape retrieving. Natural frequencies are listed in Tab. 4.5 while mode shapes are presented in the appendix C.

mode	f_n **[Hz]**
1	13.14
2	40.651
3	44.11
4	94.108
5	97.566
6	115.784
7	124.793
8	145.472
9	162.932
10	156.649
11	179.132
12	180.351
13	205.411
14	208.742
15	214.201
16	222.898

mode	f_n **[Hz]**
17	229.891
18	232.839
19	246.930
20	272.632
21	291.01
22	233.069
23	300.127
24	801.539
25	875.327
26	847.527
27	1060.29
28	1251.269
29	1228.331
30	1361.872
31	1373.927

Table 4.5: Experimental eigenfrequencies retrieved using PolyMAX algorithm in SIMCENTER Testlab 2019.1

Numerical and experimental data comparison

After performing model updating in section 4.4, numerical modal analysis is computed considering updated material properties (E = 1350 $[MPa]$ and G = 984.71 $[MPa]$, retrieved from ν estimated in section 3.2.2). Numerical and experimental mode shapes are compared visually and natural frequency difference (NFD) is carried out. Resonance frequencies and calculated NFD are listed in Tab. 4.6.

Table 4.6: Resume table of numerical and experimental resonance frequency. Natural frequency difference is listed in the last column.

	Experimental	Numerical	NFD
1	13.14	9.2182	3.9218
2	40.651	42.439	1.788
3	44.11	47.484	3.374
4	94.108	100.37	6.262
5	97.566	105.21	7.644
6	115.784	118.39	2.606
7	124.793	130.83	6.037
8	145.472	154.58	9.108
9	162.932	159.46	3.472
10	180.351	159.51	20.841

11	179.132	159.9	19.232
12	156.649	175.82	19.171
13	222.898	182.3	40.598
14	229.891	184.37	45.521
15	205.411	204.84	0.571
16	214.201	204.87	9.331
17	222.898	207.02	15.878
18	246.93	217.39	29.54
19	272.632	218.86	53.772
20	272.632	228.87	43.762
21	291.01	229.37	61.64
22	233.069	239.01	5.941
23	208.742	247.24	38.498
24	300.127	295.72	4.407
25	801.539	808.97	7.431
26	1060.29	994.02	66.27
27	1251.269	1099.9	151.369
28	1228.331	1144.2	84.131
29	1361.872	1204.2	157.672
30	1373.927	1277.8	96.127

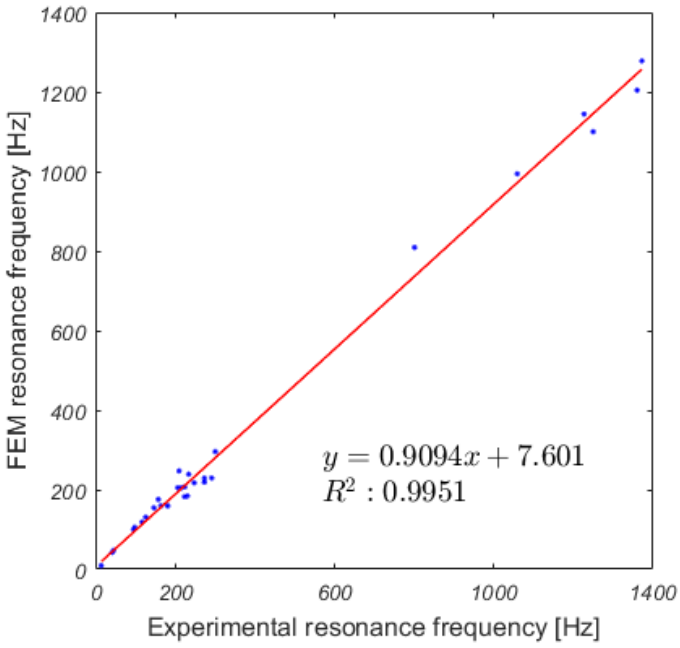

Figure 4.19: Linear fit between numerical and experimental resonance frequencies.

A linear fit is performed facing numerical and experimental resonance frequencies in Fig. 4.19. The resulting slope is equal to 0.9094 (0.8848, 0.9341) with 95% confidence bounds, which is 9% off the diagonal. Therefore, a good enough correspondence between experimental and numerical data is present. The main issue related with this type of analysis is the difficulty in the comparison between experimental and numerical mode shapes, resulting in uncertainty on visual matching. In addition, we have only scanned top and side faces of the metastructure, which is not enough for a comprehensive discernment of mode shapes. Lastly, we used a scanning laser Doppler vibrometer for the analysis, measuring in the direction of the laser beam. A 3D laser Doppler vibrometer, retrieving data in all three directions, would be a better choice for this purpose.

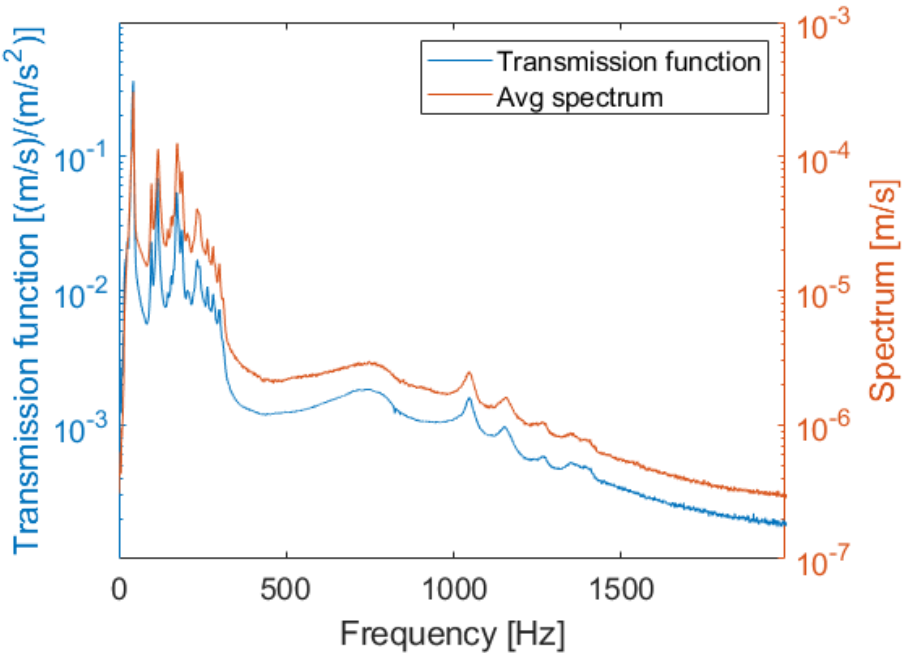

Figure 4.18: Sum over whole transmission functions over average spectrum from vibrometry data, for full bandwidth excitation.

4.6 Vibration transmissibility assessment

4.6.1 Vibration transmissibility measurement for the first metastructure

To evaluate metastructure dynamic performances with respect to the numerical case, a transmissibility measurement campaign is carried out using a similar setup with respect to the one used in Section 4.5.1. The bottom surface of the fabricated metastructure is glued on the connection plate of a shaker (Data Physics V20) characterized by an armature resonance around 12 kHz. Two miniaturized single axis accelerometers (PCB model 352C23) are employed for the test and are installed respectively on the shaker plate and on the top surface of the metastructure to measure the input and output signals. Their sensitivities are 5.39 mV/g and 5.11 mV/g, with a working frequency range from 2 to 10000 Hz (%5) [129]. An acquisition/signal generation system, Siemens LMS SCADAS mobile, is then employed to read the signal of the two accelerometers and to provide the input signal (i.e. white noise) to the shaker amplifier (Gearing & Watson Power Amplifier PA 30). In Fig. 4.20a, a schematic view of the employed experimental set-up is reported for the sake of clarity. The acquisition bandwidth spans from 0 to 10000 Hz with a frequency resolution of 1.25 Hz. The number of averages employed in each measurement is 64. The hanning window is chosen for the accelerometer signals to avoid leakage related issues.

Experimental transmissibility is finally obtained directly from the Siemens LMS TestLAB software, by making the ratio between the output and input signals (considered as the reference). In Fig. 4.20b, experimental transmission diagrams are compared with numerical results. The frequency range 0-10 kHz is chosen according to the hand probe application we are interested in and to the experimental constraints, i.e. accelerometers measurement bandwidth and shaker body resonance. Experiments clearly demonstrate the design strategy: a strong attenuation of more then two orders of magnitude is evident in the frequency range from nearly 1478 Hz to 10000 Hz (which is the upper frequency limit for the accelerometers). Attenuation levels obtained numerically cannot be achieved through experiments due to measurements noise.

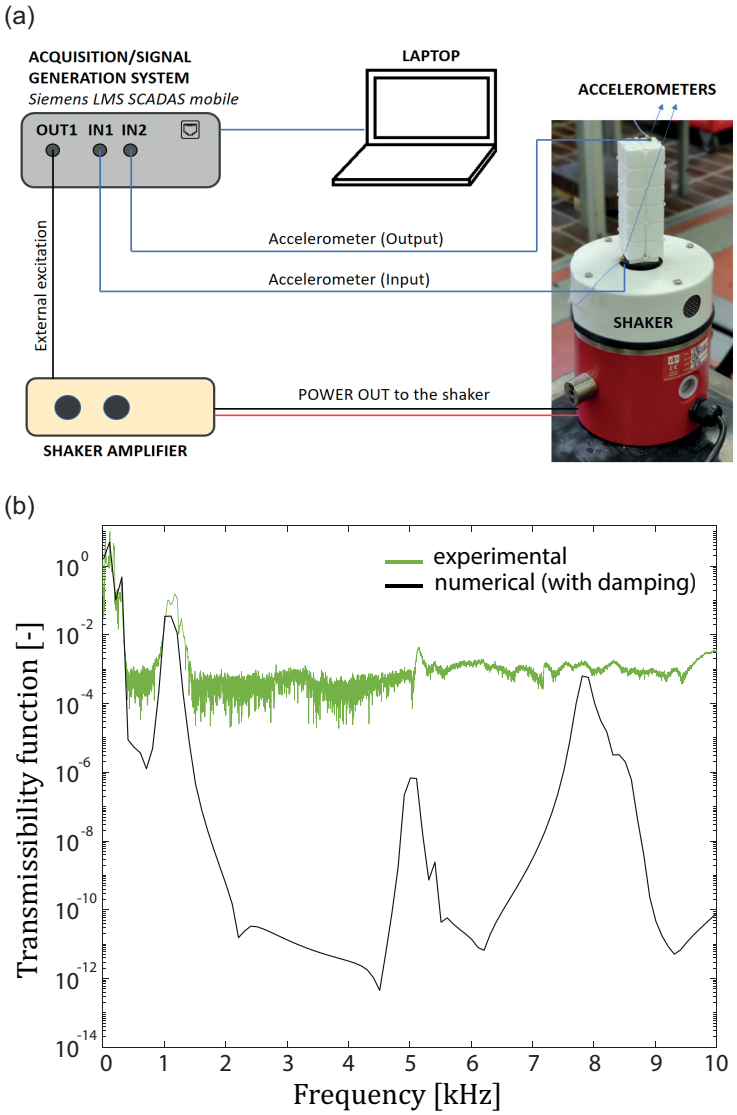

Figure 4.20: (a)Experimental set-up. (b)Transmission diagram: comparison between numerical predictions (black line) and experiments (blue and green lines).

4.6.2 Metastructure performance reproducibility

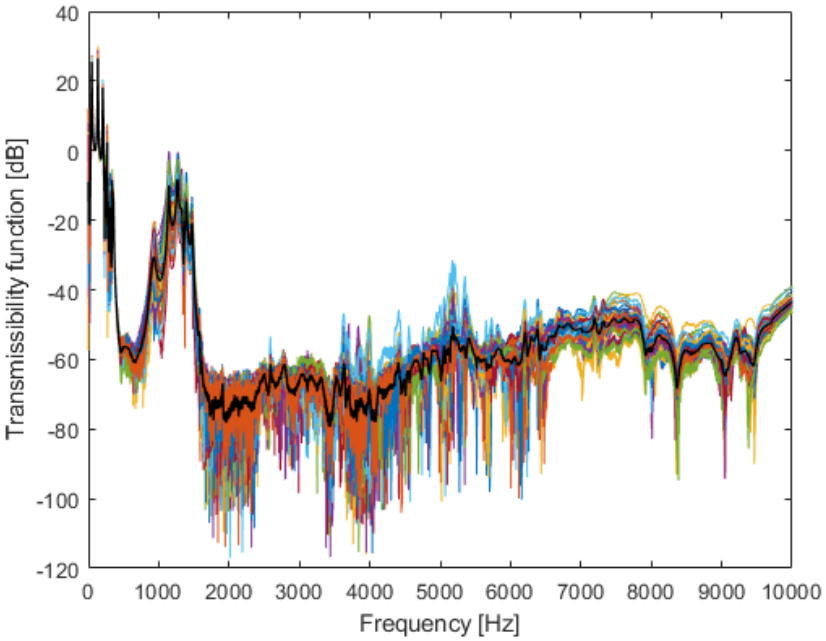

(a) Sample 3 transmissibility measurements.

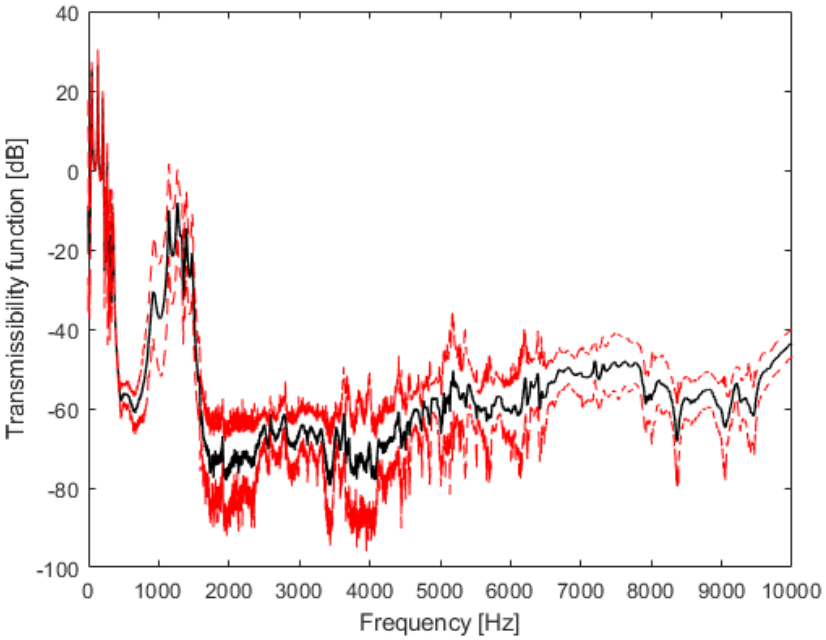

(b) Sample 3 transmissibility measurement average and relative uncertainty with a coverage factor of 2.

Figure 4.21: Repeatability of vibration transmissibility over 50 measurements on metastructure sample 3. The average curve is depicted in black.

The same transmissibility measurement carried out in the first sample, is performed the nine metastructures printed in batch, previously scanned by tomographic technique, using the same setup, shown in Fig. 4.20a, and acquisition settings. Initially, a repeatability measurement campaign is performed on a single metastructure. Each measurement is performed removing the metastructure

from the shaker plate and the accelerometer from the sample top surface, and then, assembling the same setup again. In this manner, uncertainties related with sample and accelerometer mounting are taken into account. The transmissibility of sample 3 is measured 50 times and relative uncertainty is evaluated. All 50 transmissibility measurements for sample 3 are superimposed in Fig. 4.21a over the computed average. The transmissibility uncertainty, computed with a coverage factor of 2, is plotted over the average in Fig. 4.21b.

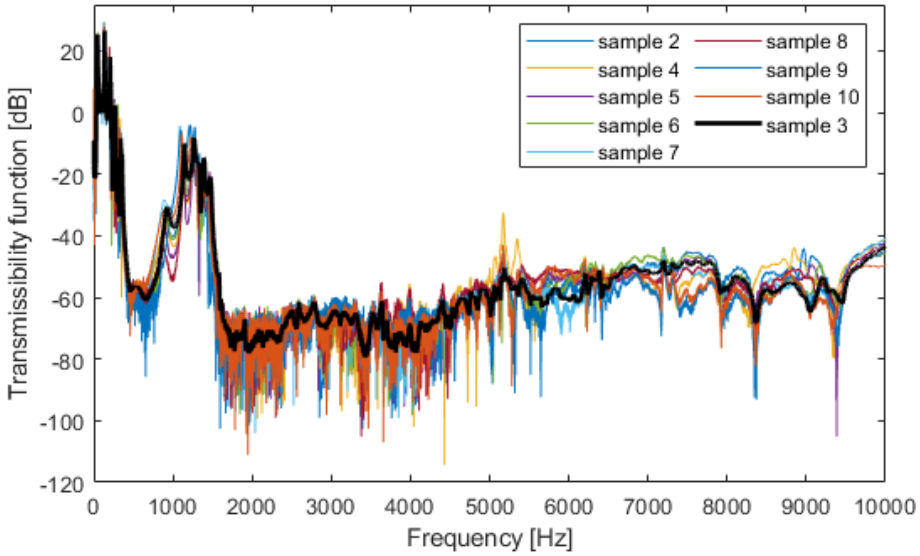

(a) Comparison between transmissibility measurements of all nine samples printed in batch.

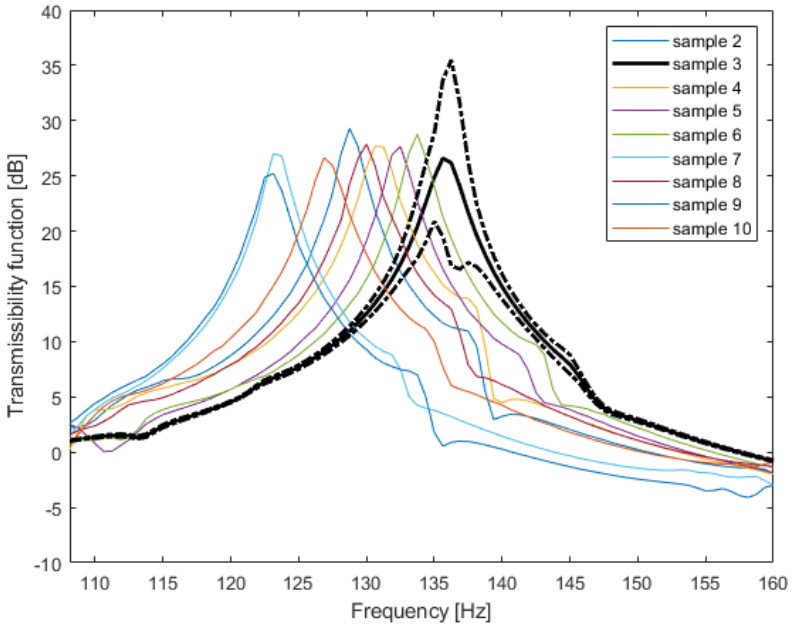

(b) Close up on the second frequency peak.

Figure 4.22: Transmissibility comparison between all manufactured samples for the second transmission peak. Average transmissibility of sample 3 is plotted in black with its relative standard deviation (coverage factor equal to 2).

Once measurement process uncertainty is evaluated on a single metastructure, transmissibility measurements are carried out over the remaining 8 samples. Obtained curves are plotted in

Fig. 4.22a spanning all the frequency range of interest. To better evaluate the metastructure performance riproducibility, the frequency shift of the second peak in the transmissibility curve is exploited. This choice is driven by the fact that to assess the metastructure frequency shift properly, the response should have enough energy to carry the information. Thus, curve features in the transmission bands, i.e. region with higher amplitude, should be considered. A zoom of the transmissibility curves from 110 Hz to 160 Hz is shown in Fig. 4.22b, highlighting the second transmission peak. The sample 3, on which repeatability campaign is carried out, is depicted with relative uncertainty with a coverage factor of 2. Curves shown in the graph are not compatible, thus, a frequency shift is present.

To investigate the possible causes that could explain such a behavior, the second peak frequency of the transmissibility function is plotted against metastructure masses in Fig. 4.23. The mass of each sample is listed in Tab. 4.7 and Tab. 4.8. It should be noted that heavier metastructures should be characterized by a lower peak frequency. Unfortunately, data seems not to fit this trend. Such a behavior may be dependent on uncertainties related with the printing process, directly affecting the slanting beam diameter and unit cell dimensions. Residual dust present in the metastructure should only led to an increase in the mass of the structure itself.

Future developments include a further analysis to assess the relation between geometrical uncertainty and variation of dynamic performances of the metastructure.

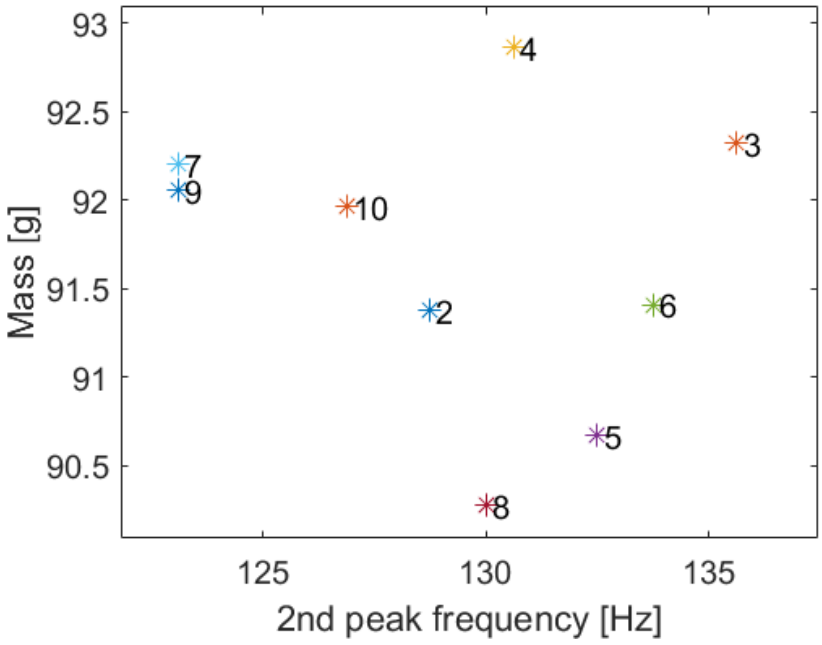

Figure 4.23: Second transmission peak frequency versus mass for all manufactured samples.

Table 4.7: Metastructure mass for enviromental temperature of 20 degC and relative humidity equal to 33.2%.

	Sample 1	Sample 2	Sample 3	Sample 4	Sample 5
weighing 1 [g]	92.34	91.38	92.33	92.86	90.68
weighing 2 [g]	92.32	91.38	92.32	92.87	90.66
weighing 3 [g]	92.32	91.38	92.32	92.87	90.67
averaged mass [g]	92.33	91.38	92.32	92.87	90.67

Table 4.8: Metastructure mass for enviromental temperature of 20 degC and relative humidity equal to 33.2%.

	Sample 6	Sample 7	Sample 8	Sample 9	Sample 10
weighing 1 [g]	91.41	92.21	90.28	92.06	91.96
weighing 2 [g]	91.41	92.2	90.28	92.05	91.96
weighing 3 [g]	91.41	92.2	90.27	92.06	91.98
averaged mass [g]	91.41	92.20	90.28	92.06	91.97

Chapter 5

Operating condition assessment

5.1 Introduction

In this section the design of a vibration probe early assembly is described and the assessment of the metastructure performances in operating conditions is presented. The probe is composed of a threaded rod (which will be mounted on a small press for testing) on which the metastructure is glued on. A connection element, designed on purpose, is then installed between the accelerometer and the metastructure, by means of adhesive tape or beeswax. Lastly, the accelerometer is attached to the connection by means of beeswax.

5.2 Accelerometer connection design

A proper choice of the connection between the accelerometer and the metastructure is fundamental to avoid the introduction of unwanted vibrations due to emerging resonances caused by the accelerometer itself or the connection element, while pressing on the surface under investigation. Different materials and geometries are tested as conceivable connections. Firstly, an aluminum square platelet, shown in the mounted configuration in Fig. 5.4, is used in the test obtaining a good but improvable response. Then, custom geometries shown in Fig. 5.1 are 3D printed using PLA (polylactic acid) and tested. The idea behind platelet design is to make an element relatively stiff to ensure a proper load on the accelerometer and sufficiently light to avoid unwanted local resonance modes. Furthermore, plastic material is ideal for this purpose due to its ease of manufacturing (using a standard fuse deposition modeling 3D printer), its mechanical properties and intrinsic high damping.

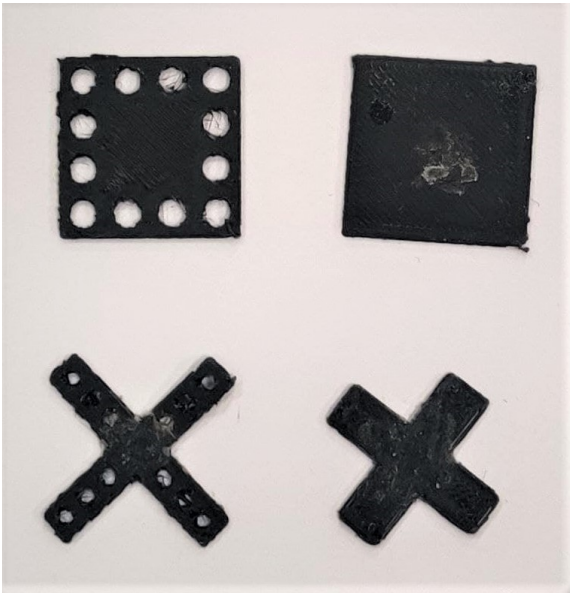

Figure 5.1: Accelerometer connection element to the metastructure.

5.3 Design validation

5.3.1 Experimental testing

As explained in Section 2.2, the vibration probe, once equipped with the proper accelerometer, is pressed against the surface under test to do the measurement. To recreate this process in a controlled manner, the vibration probe is mounted on a press using a threaded connection. The latter is used to push the metastructure, and the attached accelerometer, on an aluminum plate, clearly shown in Fig. 5.4, threaded on the shaker, which provides a controlled excitation. The setup used for this test is shown conceptually in Fig. 5.2. The same instrumentation of the transmissibility test performed in Section 4.6 is employed, with a substantial difference in terms of execution. In this case, the acquisition/generation system not only allows the acquisition of accelerometers data and shaker excitation, but also controls the response of the apparatus, consisting of the probe and the shaker, to avoid dangerous resonances, which could led to instrumentation damage due to excessive magnitude arising. This control is possible monitoring the response of two miniaturized accelerometers used in the task. The first is attached to the metastructure through the connection element discussed in Section 5.2, whilst the other is installed by means of beeswax on the shaker plate as a reference for the transmissibility function evaluation and as a control for the shaker excitation in the closed loop setup. The measurement is carried out exciting the shaker plate with a sine sweep in the frequency range of interest (100 Hz -10 kHz). To not damage the shaker, because of unwanted resonance frequencies in the system, a close loop on the control acceleration is present, maintaining it constant around 1.6 g. Tests are done pushing the metastructure against the aluminum plate (threaded on the shaker) in different steps, i.e varying the preload (in terms of displacement), by means of the threaded connection to the press, maintaining contact between the response accelerometer and the surface under test. The preload shall be provided in the linear section of the force-displacement curve of Fig. 4.12 before structure bundling, where hysteresis phenomena are contained. The linear interval of Fig. 4.12 used for retrieving stiffness is taken as a reference for preload limits. A laser triangulation system, depicted in Fig. 5.2 along with its laser path, is installed to measure the top surface displacement of the metastructure, which is related with the preload through the force-displacement curve.

The aim is to evaluate which is the optimal preload range to be used for the final application. If the vibration probe is supported by a robot, in which you can be instrumented with a force sensor, the optimal preload value need to be chosen in order to obtain a repeatable measurement. The optimal preload should always be maintained in operational condition. If, however, the probe is held by hand, it is necessary to determine how the performance of the probe changes with the

preload variation. From this analysis, the optimal preload range can be determined.

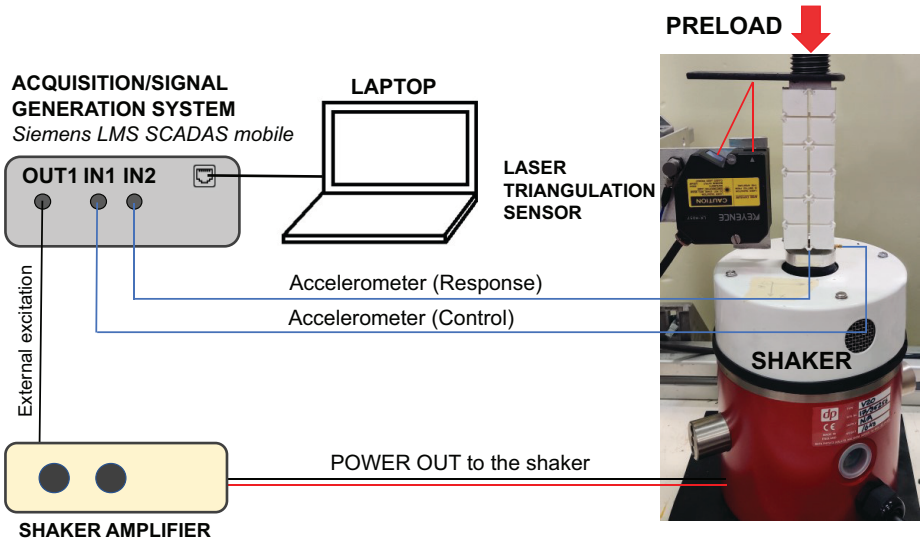

Figure 5.2: Scheme of the experimental set-up for the test in operating conditions.

The scope of this experiment is to test the metastructure in operating conditions (i.e. including all the vibration probe component), not only assessing the decoupling element performances but also its assembly. In addition, there are three crucial aspect that needs to take attention to. System element alignment is crucial not to introduce transverse loads on the metastructure, which could led to undesirable resonances and measurement stop. This issue has been encountered very often during the measurement campaign. Furthermore, all components in the experimental setup are in some way in contact to the others, as clearly shown in Fig. 5.3. This means that vibration loop problems could be present and an adequate decoupling of the shaker element from the press needs to be introduced in the future setup.

5.4 Transmissibility evaluation

Experimental data analysis is carried out in a similar way with respect to transmissibility evaluations presented in Section 4.6.1, but with a substantial difference in terms of what is then compared. In this case, making the ratio between the response (on the bottom of the metastructure) and the control accelerometers in the frequency domain, it is possible to evaluate the goodness of the metamaterial-based probe compared to the accelerometer traditionally installed. This ratio is defined as *Interfering Effect (IE)* and takes into account the intrusiveness of the metastructure on the measurement performance.

To evaluate the IE of the system properly, the excitation control should be considered. In fact, the vibration probe performance is dependent on this parameter. The control itself tend to modulate the excitation in a way that the system works in a safe manner. Doing so, the IE coefficient would be equal to 1 also in the presence of a controlled undesired resonance peak. Thus, when looking at system performance, the control driver data need to be checked to ensure it does not spoil the results.

5.4.1 Comparison between different platelet geometries

Tests are performed using different connection elements shown previously in this chapter. Initially, results for each configuration are compared at different preloads on the metastructure. Preload value, which is imposed turning the threaded rod installed in the press, ranges from the nearly undeformed state to almost 8 mm of stroke. This condition allows to work in the linear load range

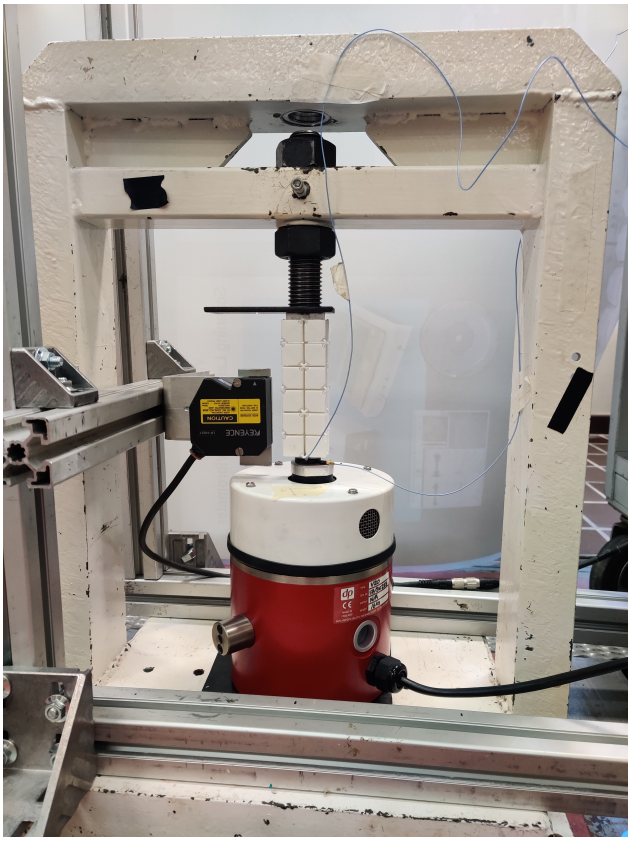

Figure 5.3: Scheme of the experimental setup for the test in operating conditions.

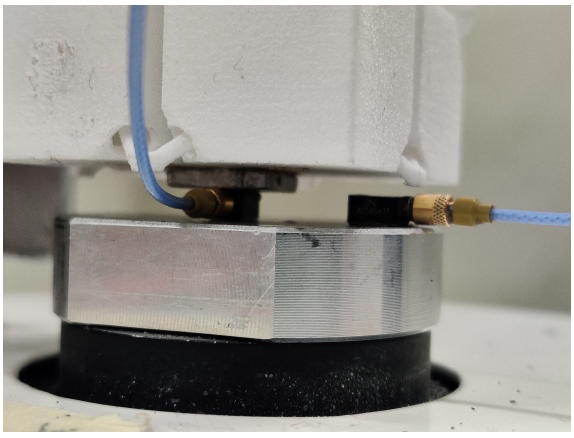

Figure 5.4: Accelerometer connection with an aluminum plate to the metastructure on the operating test setup.

and to avoid the metastructure bundling, i.e. situation in which metastructure cubes touch with the nearer ones. The incremental step used for the test is not constant due to the low precision of the available threaded rod system. Nevertheless, it allows to properly span all the preload range.

After collecting all the data at different preload for each accelerometer connection solution, the stroke (i.e. preload) values which gives the best vibrational performances in each case are assessed.

An index is defined to perform this task in first approximation, namely the *maximum deviation* (MD). It exploits the mean and the standard deviation of the IE calculated on all frequency band of interest (0-10 kHz). This index has no traditional statistical relevance, but can be employed to estimate the goodness of the measurement performance by the metastructure vibration probe. The mean value gives an estimation of how far the curve deviates from the ideal value of 1 (i.e the condition in which the accelerometer pressed with the metastructure on the aluminum plate measures exactly like the one attached with beeswax). The standard deviation gives information about how much the IE fluctuates around the mean value, i.e. how constant the vibration probe performance is. A good solution should be characterized by a mean value approaching one and a low deviation from it.

The MD is calculated and plotted for each preload value and each accelerometer connection case. Then, the best options between different accelerometer connection designs are compared to evaluate the one which gives the best overall performances.

Before starting tests with different connection elements, the driver control response is measured in a free condition (i.e. without the metastructure pushing against the shaker plate) and with only the control accelerometer attached. The driver transmissibility for our tests is reported in Fig. 5.5. Barros et al. have already investigated the transmission response of the driver under a close loop setup (controlling acceleration on different points) obtaining a similar trend, even if in a different frequency range and using a massive shaker system, proving the proper functioning of the setup. Small changes on the driver transmissibility can be lead by different positioning of the control accelerometer on the aluminum plate [130]. Therefore, the curve in Fig. 5.5 can be taken as a reference for the analysis. A change in amplitude in the driver control curve means an approaching resonance that needs to be limited.

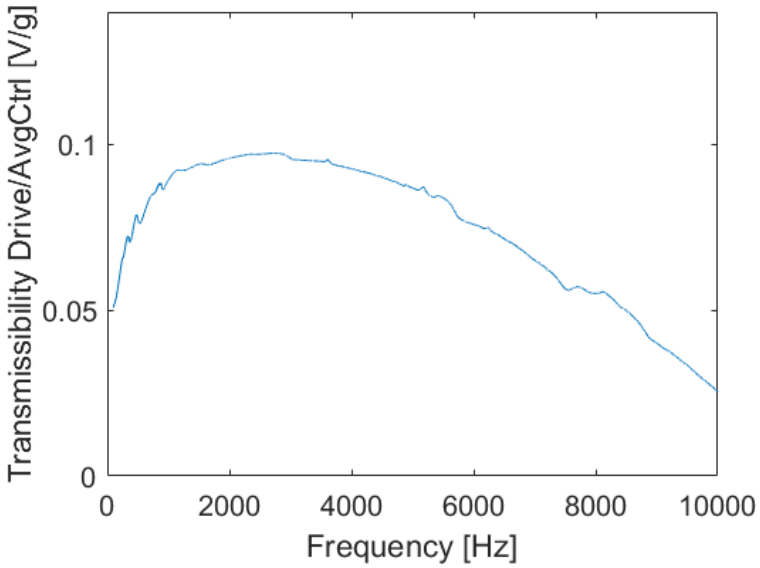

Figure 5.5: Driver voltage against average control accelerometer [V/g] measured when only the control accelerometer is attached to the shaker plate and vibration probe is not installed.

Aluminum platelet

Firstly, an aluminum plate is used to mount the accelerometer on the metastructure. The assembled system is shown in Fig. 5.4. In this case, the aluminum platelet is attached to the metastructure using beeswax, as well as the response accelerometer. Results are shown in Fig. 5.6. Data obtained exhibit a good performance for high preload values. Increasing the latter, data flattens around unity

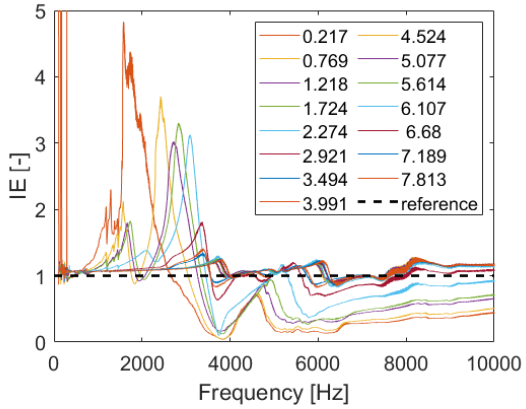

(a) Interfering effect depedence on increasing preloads.

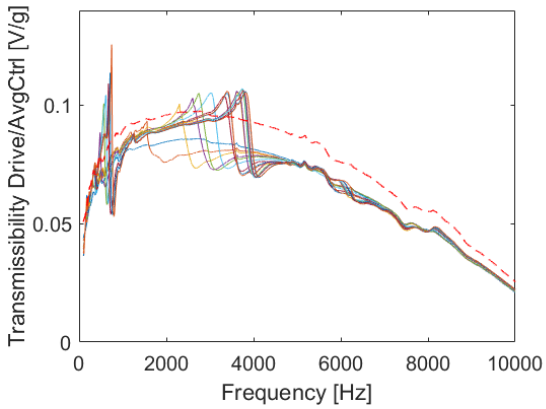

(b) Transmissibility drive over control accelerometer referred to test preloads.

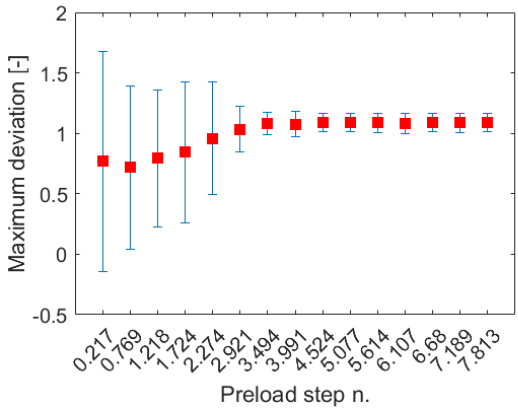

(c) Maximum deviation over test preloads. Mean values are depiceted as red squares, whilst standard deviations are represented as error bars.

Figure 5.6: Experimental results in operating conditions for the aluminum platelet.

which means the accelerometer pressed under the metastructure measure the same acceleration of the control one. Resonant peaks, initially present for low preload, which disturbs the sensor, are not found for higher values. Therefore, the metastructure has less influence on the response accelerometer and the measurement is performed properly. The same considerations can be done on the MD, which settle after a preload of 3.494 mm. Thus, preloads from 4.524 mm to 7.813 mm should provide a good enough transmission response. However, the driver control curve of Fig. 5.6b is characterized by peaks in the range between 2-4 kHz, meaning the feedback loop is controlling the excitation and, thus, the performance of the response.

Square PLA platelet

All the next connection elements are manufactured using a FDM 3D printer (Creality Ender 5 Plus) and are 1 mm thick.

The first connection to be tested is a square PLA platelet, shown in Fig. 5.7, which is attached to the metastructure with double adhesive tape. Its side dimension 16 mm. Tests are performed with increasing preloads as already pointed out. Results are shown in Fig. 5.8. By comparing the latter with results for the aluminum platelet, IE indicator is free of large resonance peaks as well as the driver transmissibility curve. The mean value of the MD (represented as red squares) decreases towards higher preload values, just like the standard deviation, but not in a sharp manner. Preloads from 3.749 mm to 7.799 mm provide a good vibration response for the vibration probe in operating conditions.

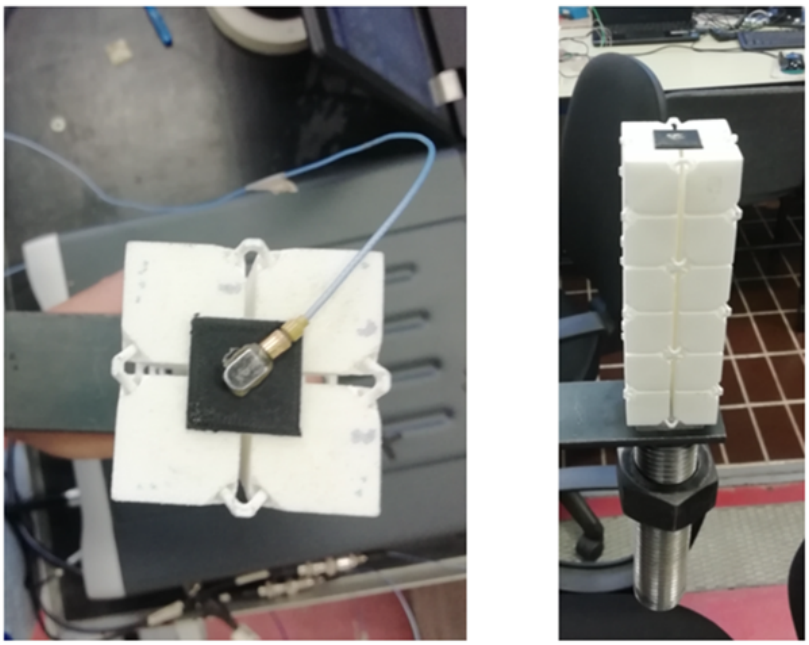

Figure 5.7: Square PLA platelet mounting.

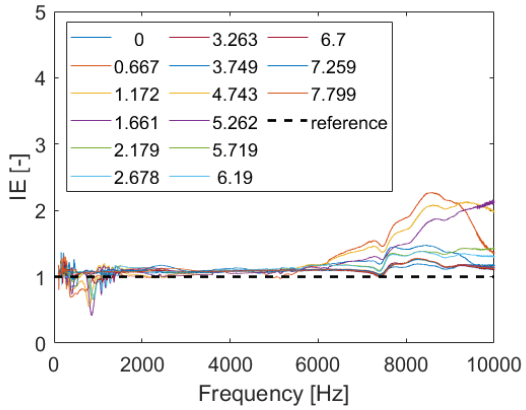

(a) Interfering effect depedence on increasing preloads.

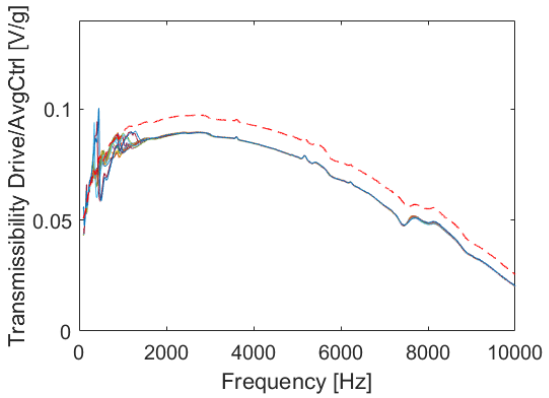

(b) Transmissibility drive over control accelerometer referred to test preloads.

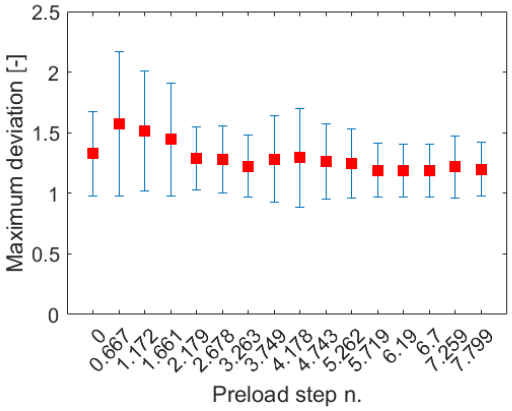

(c) Maximum deviation over test preloads. Mean values are depiceted as red squares, whilst standard deviations are represented as error bars.

Figure 5.8: Experimental results in operating conditions for the square PLA platelet.

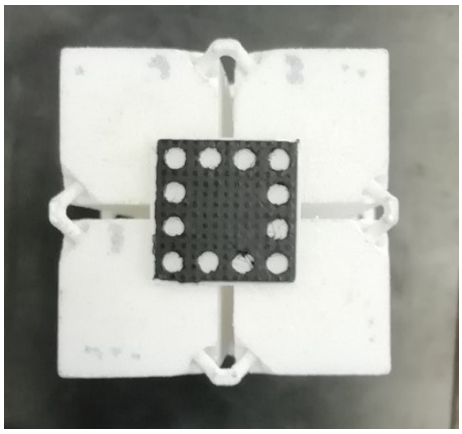

Figure 5.9: Perforated square PLA platelet mounting.

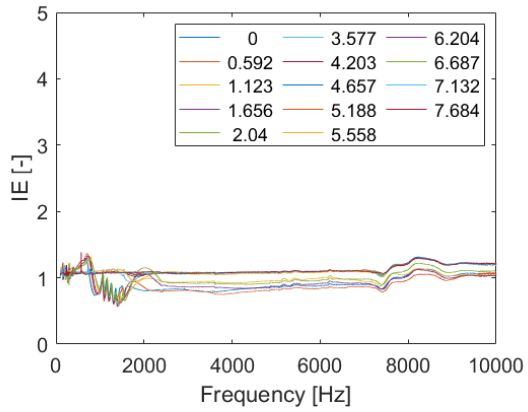

(a) Interfering effect depedence on increasing preloads.

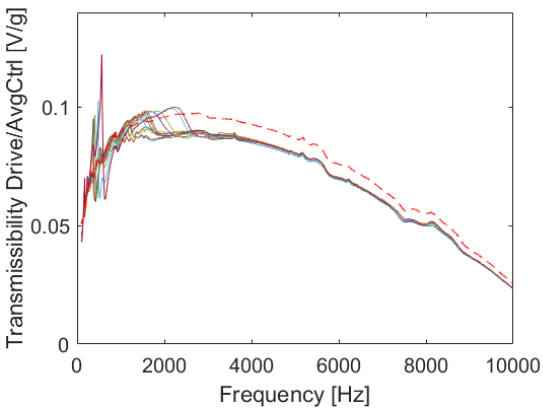

(b) Transmissibility drive over control accelerometer referred to test preloads.

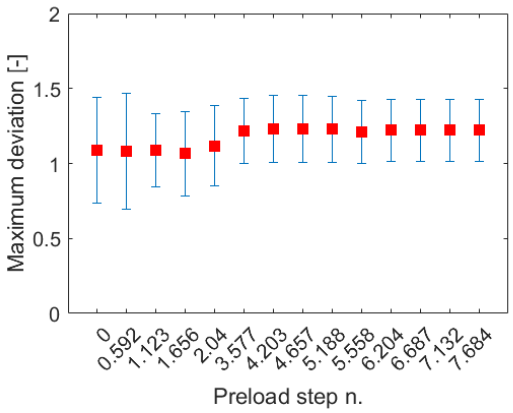

(c) Maximum deviation over test preloads. Mean values are depiceted as red squares, whilst standard deviations are represented as error bars.

Figure 5.10: Experimental results in operating conditions for the perforated square PLA platelet.

Perforated square PLA platelet

To lighten the structure, and consequently remove potential unwanted resonances, the square platelet is perforated near the outer edge, making holes with a diameter of 3mm. Its mounting

configuration is shown in Fig. 5.9. Results, shown in Fig. 5.10, are in line with the previous ones. The IE is well aligned to unity for higher preload values. Also, MD is stable above 4.203 mm of preload value. Looking to the drive transmissibility chart, a resonance peak is present and it slides towards higher frequencies increasing the preload value. Thus, a driver tension regulation is necessary, in this case, to compensate for system resonances. Therefore, IE data is valid only considering curves in which the driver control modulation is small. Good performances are obtained ranging preload values approximately from 6.204 mm to 7.684 mm.

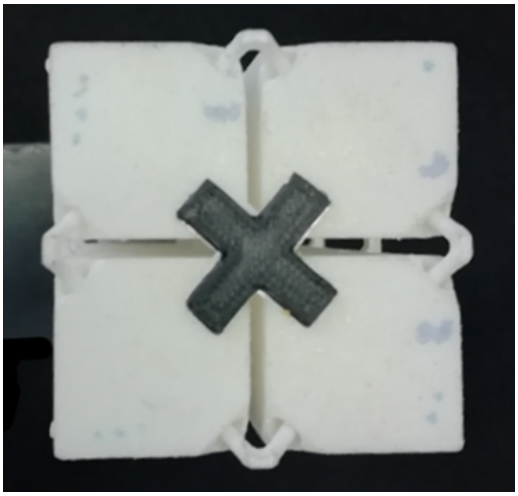

Figure 5.11: Cross PLA platelet mounting.

Cross PLA platelet

Beside the simple square geometry shown previously, another design attempt is made using a cross PLA platelet. The cross side is 12 mm long, while the width of each branch is 4 mm. Test results are shown in Fig. 5.12. IE curves align together above 2.202 mm of preload, in a similar way compared to previous cases. Furthermore, increasing this value up to 5.172 mm, eventual resonance peak flattens and curves aggregate better. In addition, the MD is consistent with the already exhibited trend. Preload values which give the best performance range from 5.172 mm to 7.691 mm.

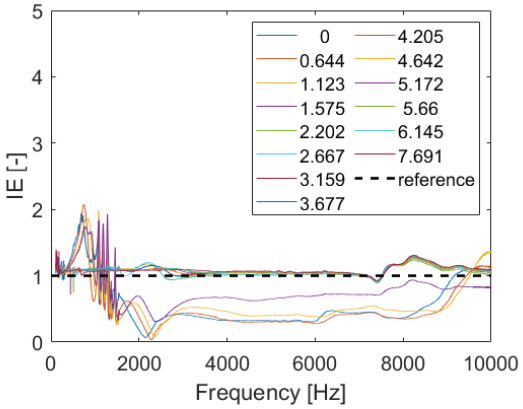

(a) Interfering effect depedence on increasing preloads.

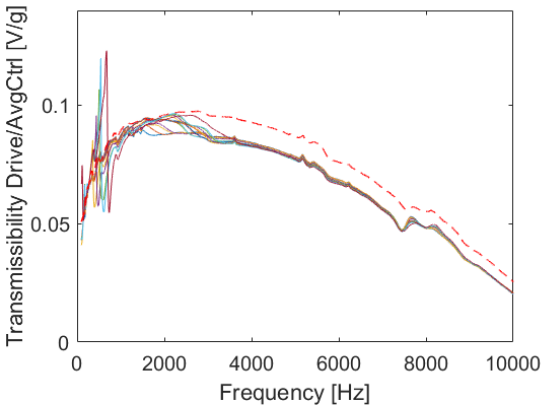

(b) Transmissibility drive over control accelerometer referred to test preloads.

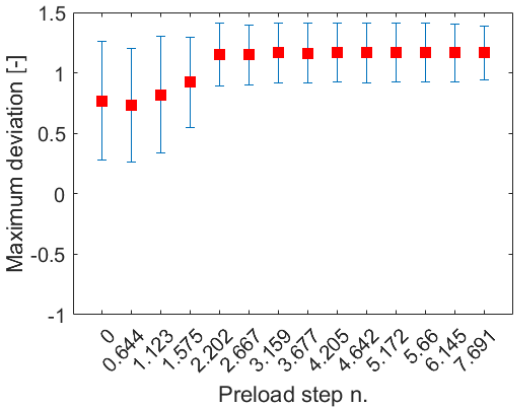

(c) Maximum deviation over test preloads. Mean values are depiceted as red squares, whilst standard deviations are represented as error bars.

Figure 5.12: Experimental results in operating conditions for the cross PLA platelet.

Perforated cross PLA platelet

Figure 5.13: Perforated cross PLA platelet mounting.

Lastly, to lighten the cross structure, crosses are stretched (obtaining a branch side length of 14 mm) and holes, with a diameter equal to 2 mm, are added. The perforated cross attached to the metastructure is shown in Fig. 5.13. In this case, IE performances are better above 5.07 mm of preload value, aggregating the transmission curves. Anyway, even if using high preload values, resonances tend to be present with a small amplitude. MD is well aligned for preloads values above 5.07 mm, although certain lower preload values could to be a possible choice. Overall, the system performance seems to be better using a preload from 5.07 mm to 7.585 mm.

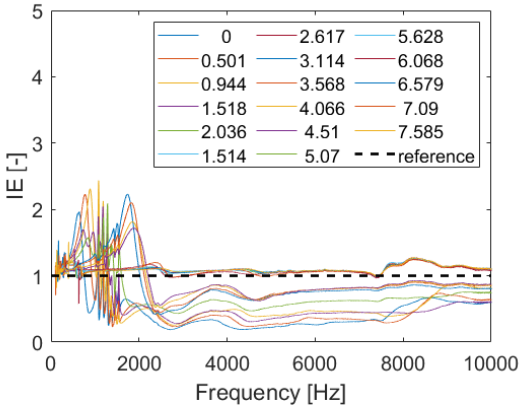

(a) Interfering effect depedence on increasing preloads.

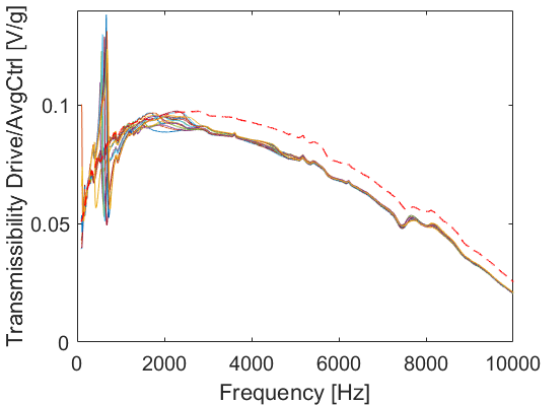

(b) Transmissibility drive over control accelerometer referred to test preloads.

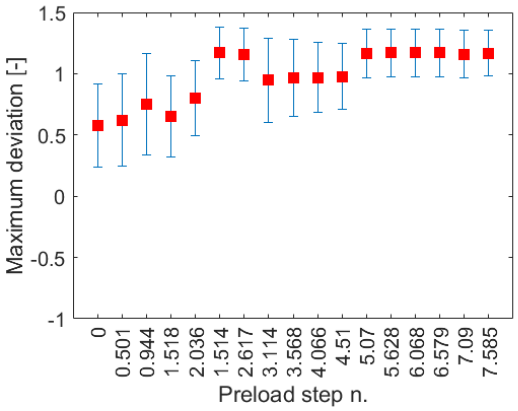

(c) Maximum deviation over test preloads. Mean values are depiceted as red squares, whilst standard deviations are represented as error bars.

Figure 5.14: Experimental results in operating conditions for the perforated cross PLA platelet.

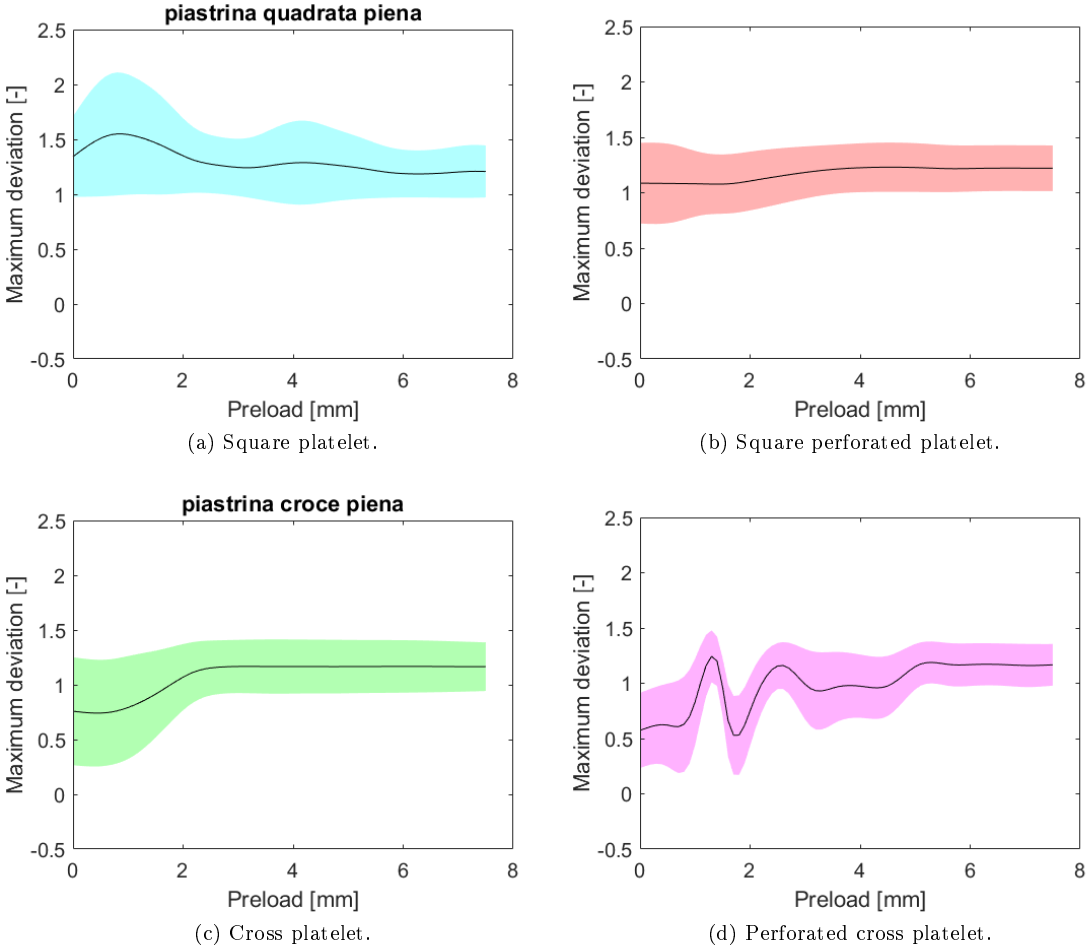

(a) Square platelet.

(b) Square perforated platelet.

(c) Cross platelet.

(d) Perforated cross platelet.

Figure 5.15: Comparison between PLA platelet performances in operating conditions, retrieved from Maximum Deviation fit.

Comparison

In conclusion, each solution shows a good working possibility if the preload is properly chosen and the whole system is aligned. Moving towards higher preload values, thus bringing the metastructure to compression, its decoupling performance increases allowing the vibration probe to measure properly. A typical preload range for this application spans from 6 N to 12 N.

The overall best IE transmissions picked manually for the different designs are reported in Fig. 5.16 for comparison. All curves are more o less aligned, proving there is a low dependence on the design geometry of the component. On the other hand, changing the connection element material from plastic (PLA) to aluminum, results in a large variation in the response. In fact, the IE related to the aluminum platelet show two resonance peaks near 3500 Hz and 6000 Hz, not present in the other configurations.

To compare the performance of the different designs in the same preload conditions, a fit of the MD index is carried out obtaining the working areas shown in Fig. 5.15. The mean value is represented as black lines, whilst standard deviation is depicted as colored areas. Comparing the charts, all the PLA designs align well for high preload values, leading to similar performances. The cross and square perforated platelet seem to be the most stable solutions with respect to preload variations.

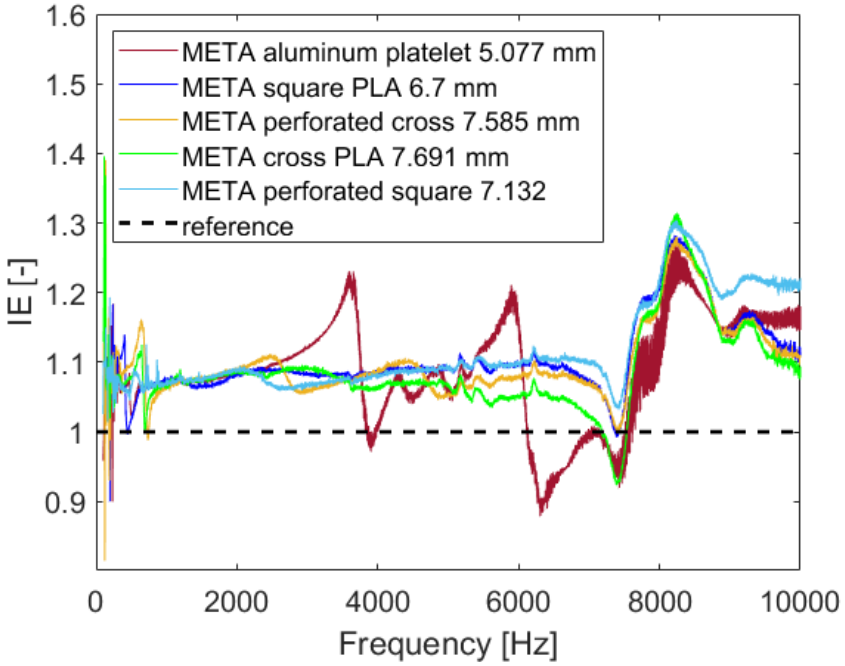

Figure 5.16: IE comparison between different design solutions.

5.5 Measurement setup and samples reproducibility

Until this point, different accelerometer connection designs have been tested in operating condition. The cross PLA platelet design is chosen to be used for testing the riproducibility of the setup (repeating measurements using the same metastructure sample) and different metastructures. For the sake of synthesis, only a few representative preload curves are shown in the following images. Their performances are then superimposed with the previous fit of Fig. 5.15c, computed at the specific preload values, verifying they fall within the same interval.

Firstly, the reproducibility of the setup is tested repeating the measurement campaign on the metastructure sample 1 with a cross PLA platelet as connection element. Results are shown in Fig. 5.17. Increasing preload value, IE curves align around unity as expected. The MD represented in Fig. 5.17c remark this behavior. Comparing the single measured values with the system performance (depicted as a light green area) retrieved in Sec. 5.4.1, the metastructure operates within the tolerances, as expected.

Comparing results with the previous test of Fig. 5.12, they are quite similar in the first half part of the chart. Looking at higher frequencies, system resonances are quite different, even if in the same magnitude range. This uncertainty may be related with the test setup itself. In fact, the alignment of each component of the system (from the threaded rod, through metastructure to the accelerometer) is crucial to let the structure operate in proper conditions, avoiding shear loading. Thus, we can conclude that the setup needs to be improved to allow a better reproducibility of the experiment but is good enough for a first testing of metastructure performances.

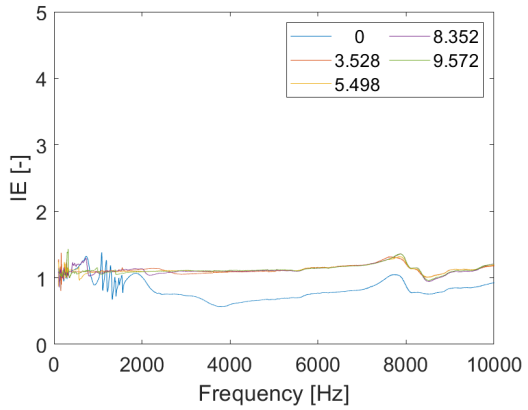

(a) Interfering effect depedence on increasing preloads.

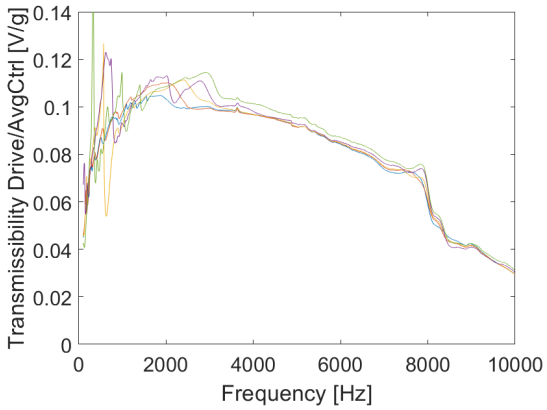

(b) Transmissibility drive over control accelerometer referred to test preloads.

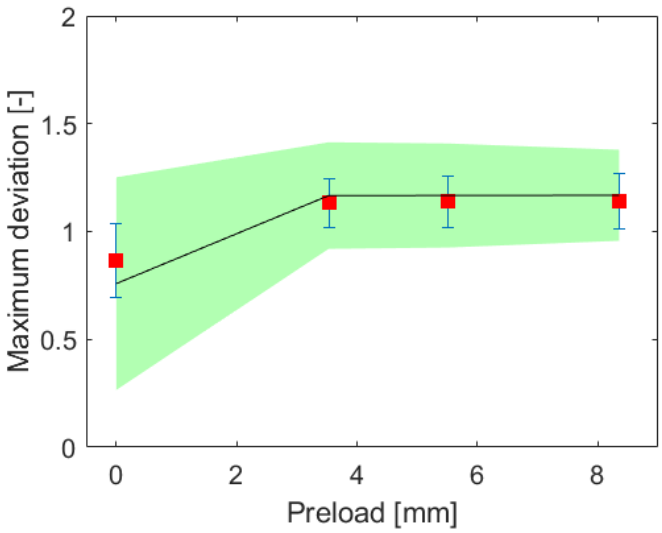

(c) Maximum deviation over test preloads. The reference performance range is depicted as a light green area, whilst its mean is represented as a black line.

Figure 5.17: Experimental results in operating conditions using the PLA cross platelet repeating measurements for sample 1.

Afterwards, tests in operating conditions are carried out on different metastructures. Results for the different samples are shown in Fig. 5.18, 5.19 and 5.20. Comparing the IE curves for the three cases, they show, as expected, the same trend: the higher the preload, the better the metastructure performances. Furthermore, curves are well aligned around the unity and are comparable to the one of Fig. 5.17. Lastly, the MD index for all cases is characterized by a variability within the reference performance range (depicted as a light green area), which even improves as the preload increases.

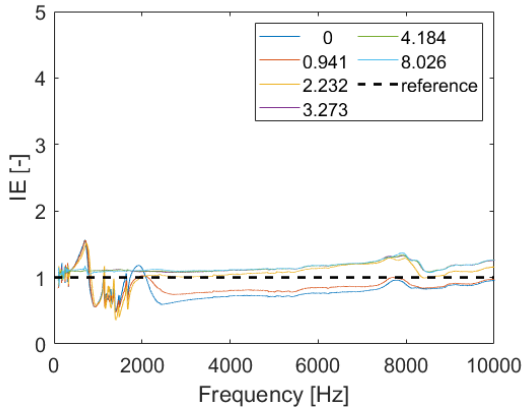

(a) Interfering effect depedence on increasing preloads.

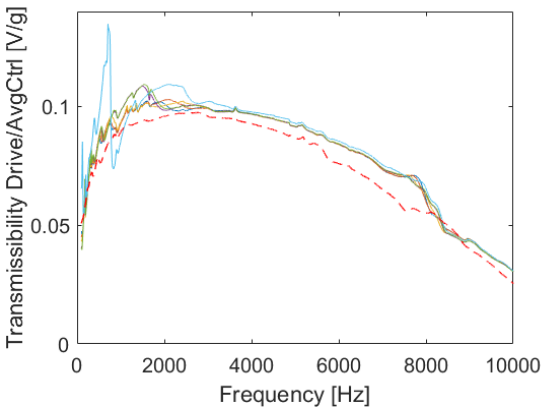

(b) Transmissibility drive over control accelerometer referred to test preloads.

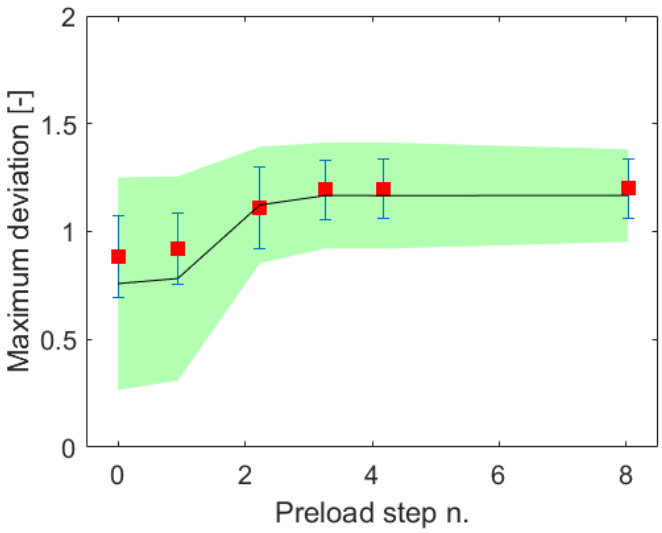

(c) Maximum deviation over test preloads. The reference performance range is depicted as a light green area, whilst its mean is represented as a black line.

Figure 5.18: Experimental results in operating conditions for the PLA cross platelet for sample 3.

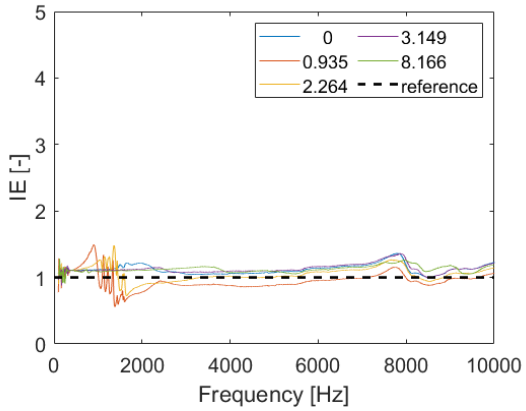

(a) Interfering effect depedence on increasing preloads.

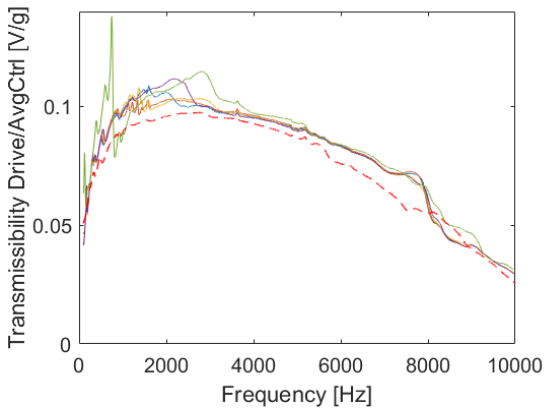

(b) Transmissibility drive over control accelerometer referred to test preloads.

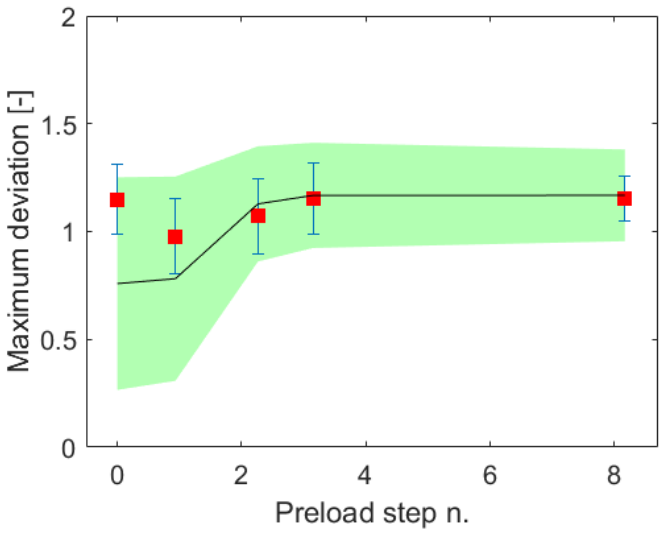

(c) Maximum deviation over test preloads. The reference performance range is depicted as a light green area, whilst its mean is represented as a black line.

Figure 5.19: Experimental results in operating conditions for the PLA cross platelet for sample 4.

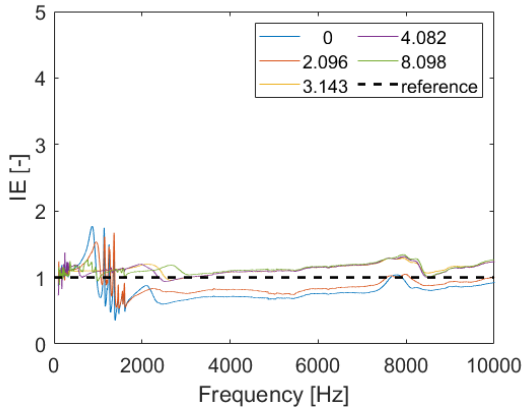

(a) Interfering effect depedence on increasing preloads.

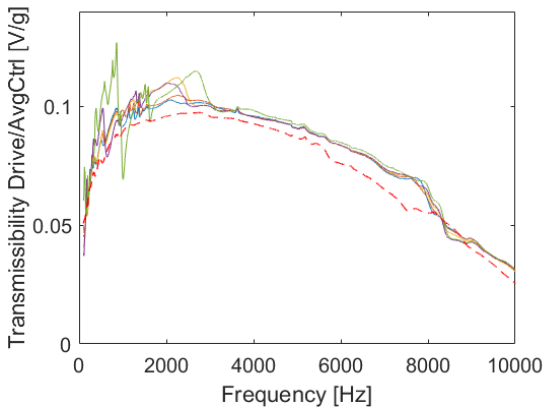

(b) Transmissibility drive over control accelerometer referred to test preloads.

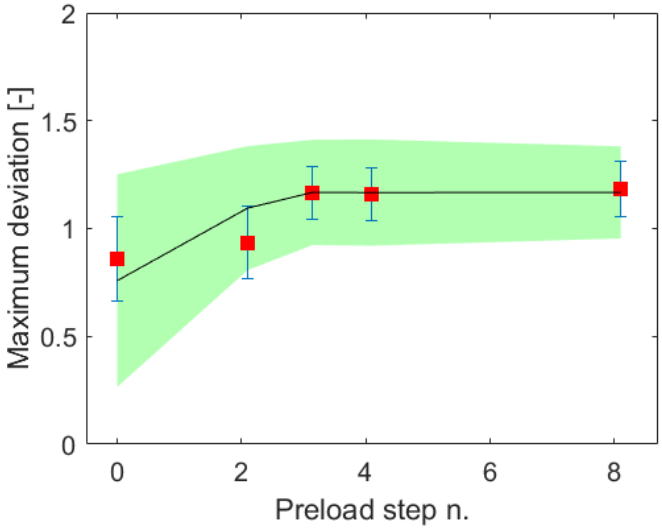

(c) Maximum deviation over test preloads. The reference performance range is depicted as a light green area, whilst its mean is represented as a black line.

Figure 5.20: Experimental results in operating conditions for the PLA cross platelet for sample 5.

5.6 Comparison between different commercially available solutions

A typical commercial solutions for vibration measurements is the DISCOM vibration probe. Its performances were tested, prior to this thesis work, using a similar close-loop setup with control on the acceleration. In this case, the RMS value is used for data comparison and analysis. DISCOM vibration probe test results are shown in Fig. 5.21 for three different preload values. Transmissibility curves in operating conditions for both DISCOM and metastructure solutions are then compared on the same chart shown in Fig. 5.22. In the very low frequency range, DISCOM vibration probe seems to work better compared to the metastructure one. This is not a novelty, the metastructure is designed to be used in the frequency bandgap, thus above approximately 1500 Hz, although, results are encouraging. The metastructure IE response (for the majority of accelerometer connection types) is nearly constant until 7 kHz roughly. Furthermore, looking at higher frequencies of the design range, the deviation from the ideal condition is remarkably smaller considering the metastructure solution. Thus, even if in a preliminary design geometry, the metastructure proposed in this thesis seems to be a good solution to be used as a decoupling element

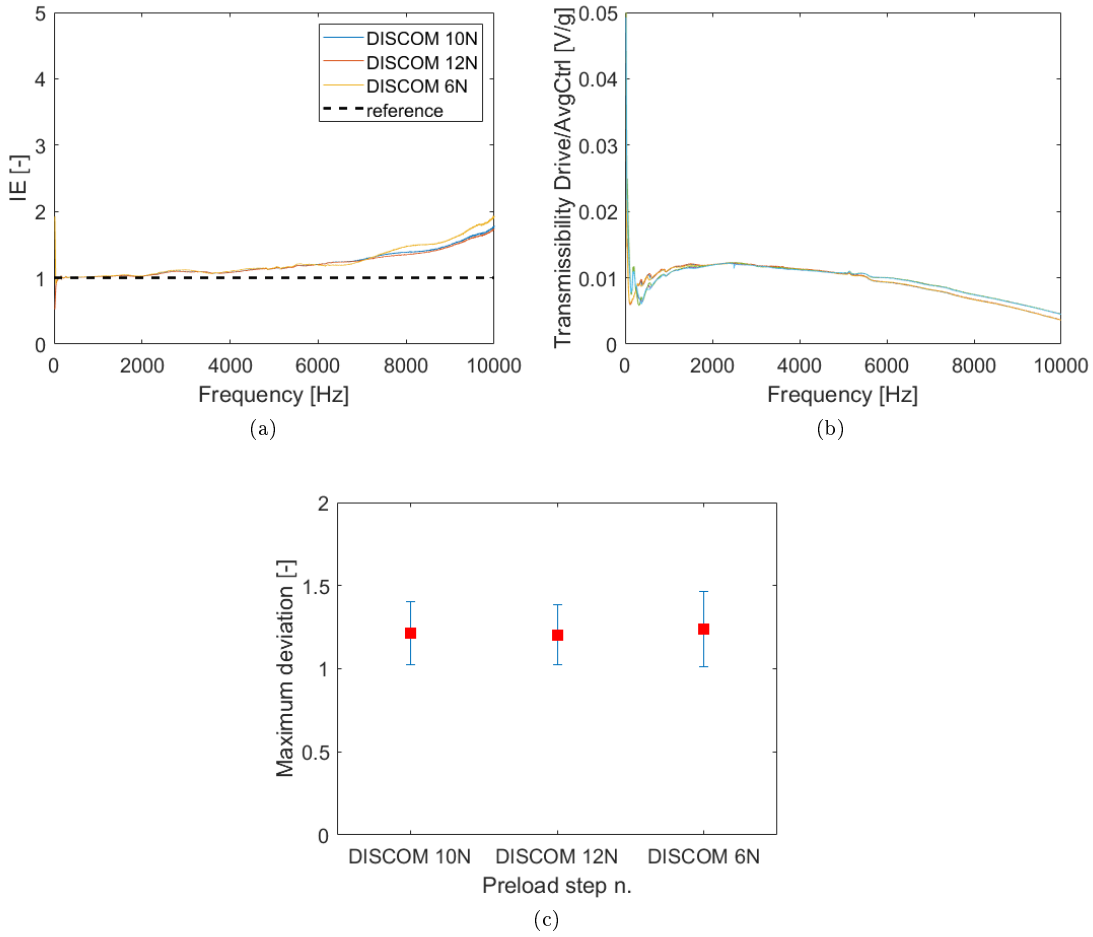

Figure 5.21: Experimental results in operating conditions obtained for DISCOM commercial solution.

for a hand-held vibration probe.

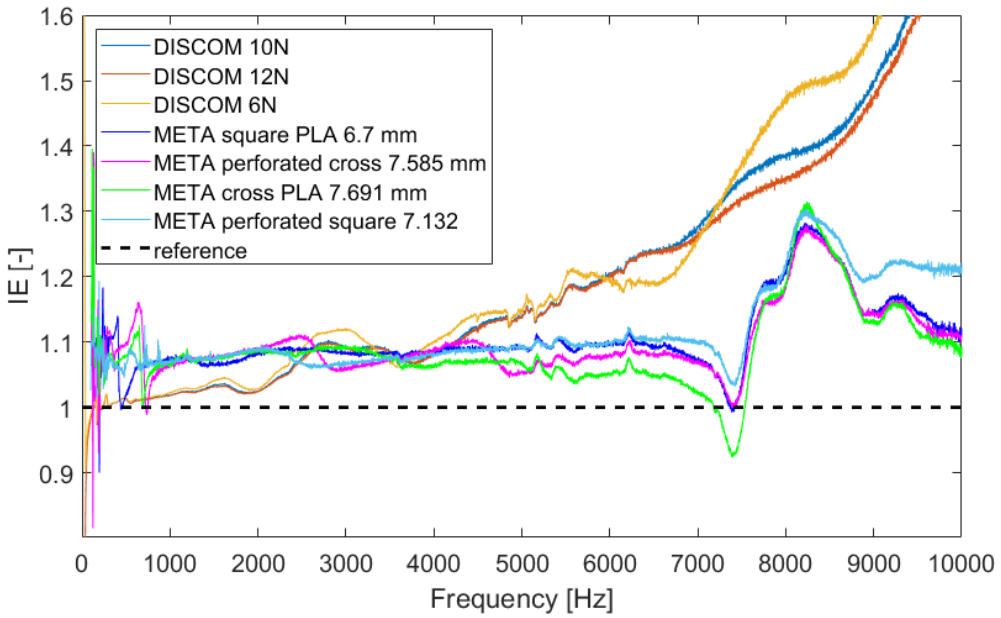

Figure 5.22: Comparison between DISCOM acquired data and metastructure solution.

Chapter 6

Multi-material metastructure

6.1 Introduction

The need to reduce the overall dimensions of the metastructure, while maintaining its vibrational performances, can be achieved by exploiting a multimaterial approach. In addition, we focused on structure modularity for metastructure scalability in size. The unit cell is engineered properly to assess novel requirements.

6.2 Unit cell design

The metastructure topology remains unchanged. Plastic tetrahedral masses are replaced with steel one. Adequate joints are engineered to connect tetrahedral masses to the metastructure skeleton. Furthermore, slanting beam connections are designed bulkier to be more robust.

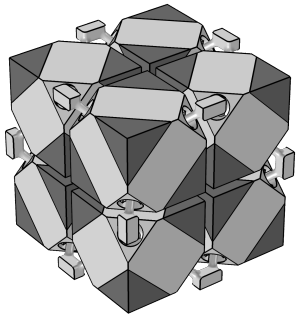

(a) Multimaterial unit cell final assembly.

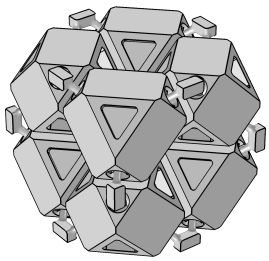

(b) Plastic skeleton.

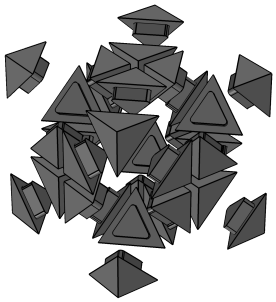

(c) Metal tetrahegonal masses.

Figure 6.1: Multimaterial unit cell

6.3 Bandgap sensitivity analysis

Once the design topology is defined, it is important to choose the proper geometry parameters to minimize metastructure encumbrance whilst maximizing its frequency performances. For this reason, a sensitivity analysis on a parametric geometry of the metastructure is carried out with respect to the unit cell size a, the slanting beams diameters d and the steel mass cutting plane *offset*.

Considering our application, unit cell size should be as small as possible to obtain a compact enough metastructure. The unit cell size a for the analysis spans from 30 to 35 mm. Moving from bigger to smaller values, the bandgap widens but moves towards higher frequencies. The frequency shift is linear with the dimension changing, due to the linear relation between stiffness and dimensions.

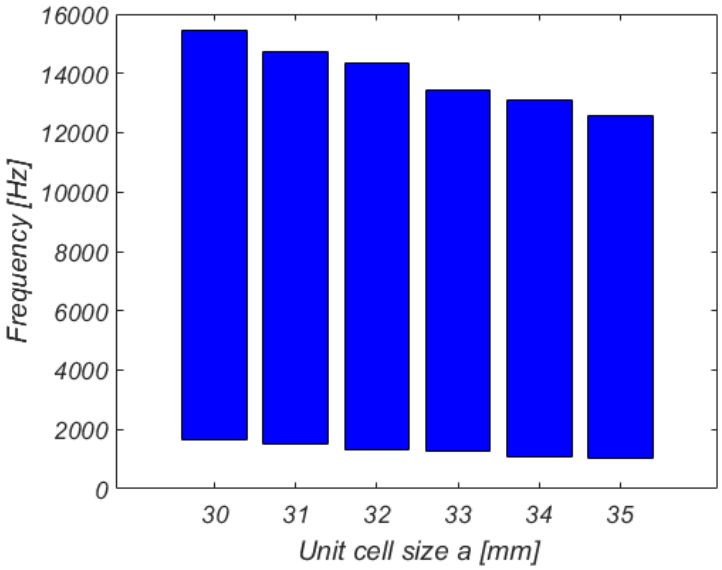

Figure 6.2: Bandgap dependence on unit cell size a. The slanting beam diameneter is 1.2 mm while the offset is 3.5 mm.

Reducing unit cell size, it is fundamental to vary the diameter accordingly to achieve a wide enough bandgap. For this reason, metastructure performances are evaluated varying the diameter d of the slanting beam from 1.2 mm (SLS technology limit) to 1.6 mm. Even if the variation is small in comparison to the bandgap width, reducing the diameter of the slanting beams results in a shift of the bandgap opening frequency towards lower values. The small variation is related to the stiffness of the slanting beams (which has a is linear dependence for axial deformation and a cubic dependence for shear and torsional one) and their participation to global modes at the extremes of the bandgap. Looking at global modes of Fig. 6.5b, it can be argued that for both the opening and closing bandgap ones, there is a small participation of the slanting beams in the deformation. They mostly deform axially in the first global mode, thus, justifying the wider frequency variation of the bandgap opening with respect to the closing frequency.

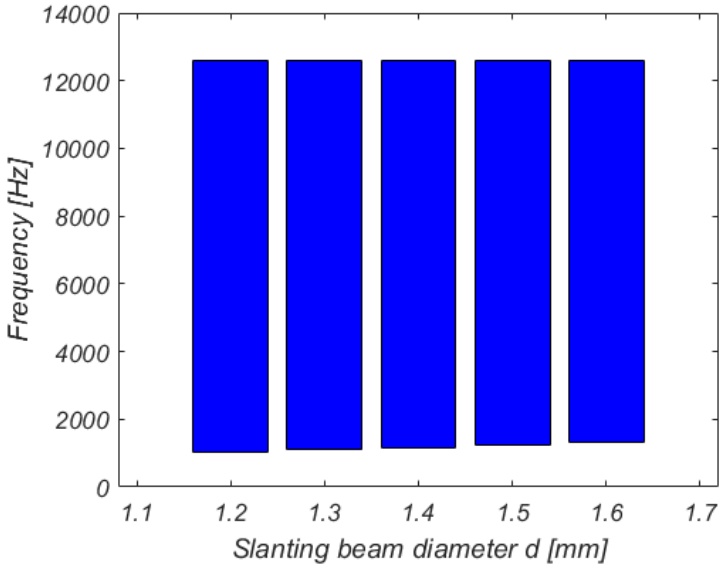

Figure 6.3: Bandgap dependence on diameter d. The unit cell size is 35 mm while the offset is 3.5 mm.

The last parameter considered in the analysis takes into account the percentage of steel in the unit cell. Steel is introduced in the geometry on cube corners, cutting and replacing them accordingly as shown in Fig. 6.1. Thus, the distance of the cutting plane from the center of the cube, called *offset*, defining the base of the steel masses, is considered. We assume it can vary from 3 mm to 4.5 mm, in accordance with geometrical constraints of the assembly. Moving to smaller (i.e. bigger steel mass) to bigger (i.e. smaller steel mass) values the bandgap widens, but also moves towards higher frequencies.

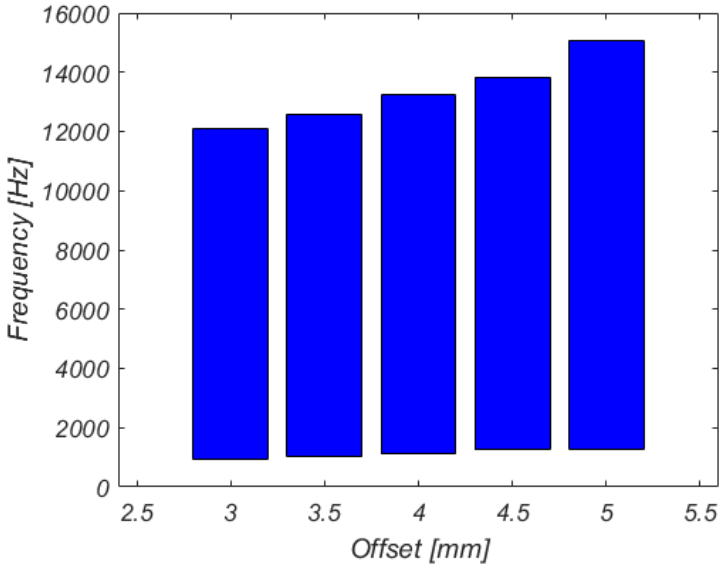

Figure 6.4: Bandgap dependence on steel mass offset *offset*. The slanting beam diameneter is 1.2 mm while the unit cell size is 35 mm.

Finally, performance dependence on geometric parameters is assessed and a trade off with application requirement is done. The need of compactness for easy of usage in the industrial environment led to chose the smallest unit cell size possible for the SLS technology, in this case equal to $a = 30$ mm. Therefore, to compensate the shift versus higher frequencies due to unit cell reduced

size (i.e. to lower the bandgap opening frequency to maintain equal isolation performances), a diameter of $d = 1.2$ mm is chosen, which is the smallest feasible for the manufacturing process. In addiction, for the same prior reason, a $offset = 30$ mm is chosen, lowering the bandgap even further.

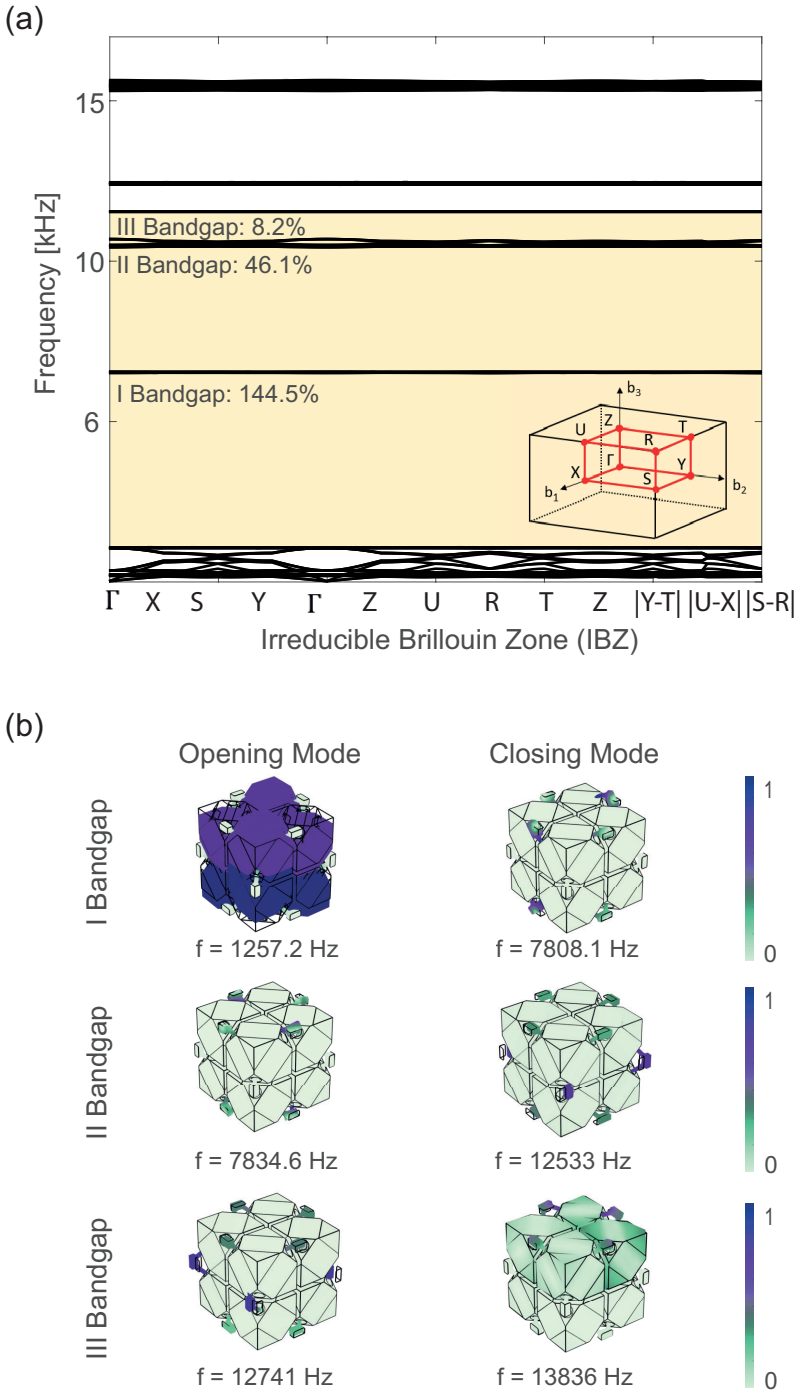

Figure 6.5: (a) Numerical dispersion diagram computed in COMSOL Multiphysics©. The considered Irreducible Brillouin Zone (IBZ) is also provided. (b) Elastic mode shapes (normalized with respect to the maximum displacement) at lower and upper bounds of the bandgaps. The symmetry points are not specified since the modes of each bandgap limit present the same mechanical characteristics. The contour of the normalized displacement field is shown in color.

6.4 FEM analysis

6.4.1 Dispersion analysis

As in the previous case, the multimaterial metastructure dispersion is computed numerically using COMSOL Multiphysics© to determine the bandgap performances of the unit cell shown in Fig. 6.1. Periodic boundary conditions are applied on the six external surfaces of the novel unit cell in the three orthogonal directions to simulate the infinite periodic medium. The same a simple orthorhombic lattice (ORC), already used in the prior FEM model, is chosen for the analysis. The associated Irreducible Brillouin Zone (IBZ) is reported in the figure. Finally, the band diagram is shown in Fig. 6.5a. Under the hypothesis of infinite medium, the multimaterial unit cell is characterized by five wide bandgaps. For our purpose, we are interested in the highlighted ones, because they are trapped between global modes. The first bandgap opens at 1257.21 Hz and closes at 7808.1 Hz, the second covers the range of frequencies from 7834.6 Hz to 12533 Hz, while the third from 12741 Hz to 13836 Hz. Mode shapes with associated opening and closing bandgap frequencies are shown in Fig. 6.5b to evaluate their nature. Exactly like what happens in Fig. 3.3, the first opening mode involves a big modal mass, while the others are characterized by a local deformation of the slanting beam connection between masses. Thus, it confirming the unit cell isolation efficiency. A repetition of three unit cells is sufficient to obtain the metastructure performances we are aiming for our purpose.

The mesh used for the eigenfrequency analysis is shown in Fig. 6.6. The maximum element size used is smaller than $\lambda/5$, where λ is the wavelength associated to the highest frequency to be considered (which is equal to 13836 Hz, referring to Fig. 6.5b).

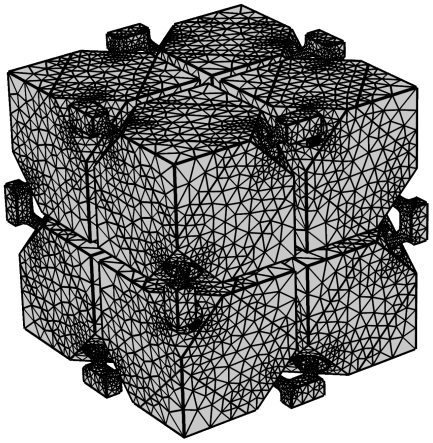

Figure 6.6

6.4.2 Static analysis

In Section 3.3.2, the metastructure manufacturability is assessed through numerical models. The same considerations are performed for the multimaterial case, taking into account gravity load for horizontal and vertical configuration. The base surface of the metastructure is assumed fixed on all simulations. The mesh used for the computation is shown in Fig. 3.6.

A stationary study is used to assess the metastructure compression due to gravity load. The resulting displacement field is reported in Fig. 6.8. The numerical simulation gave as result a maximum stroke of 0.12 mm along the axial direction. Hereafter, the case of a distributed or off-centered compression load equal to 10 N is considered. In the first case, an off-center load is imposed on a single mass of the top surface, resulting in a maximum displacement of13.36 mm in the axial direction. In the second case, the same load is applied on two different adjacent masses of the metastructure, obtaining a maximum stroke of 6.95 mm along the axial direction. Lastly, the load is applied on the whole top surface, resulting in a stoke equal to 2.64 mm which is a reasonable value for practical applications.

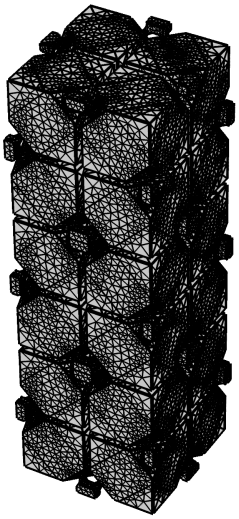

Figure 6.7: Mesh used for the static study, with a average element quality equal to 0.64.

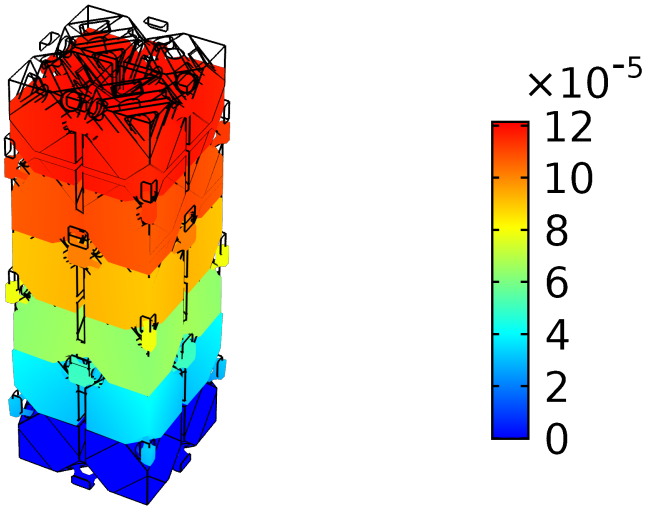

Figure 6.8: Numerical displacement due to the gravity along the axial direction.

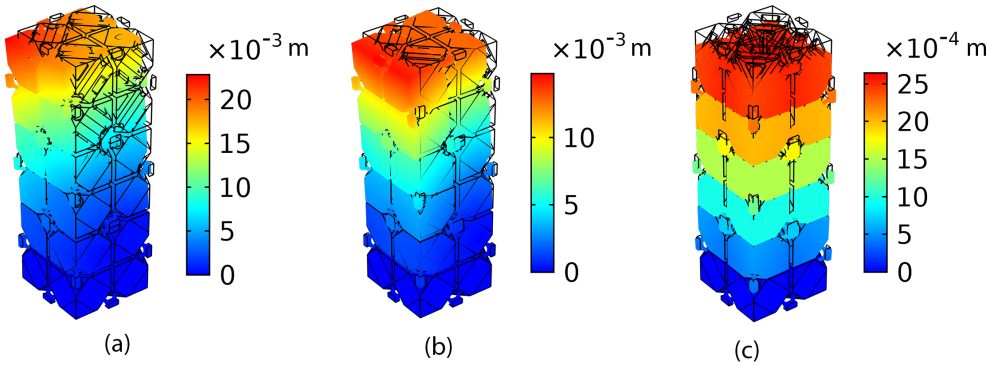

Figure 6.9: Metastructure displacement field due to the superposition of gravity load and surface load of 10 N on (a) only one mass, (b) two adjacent masses or (c) on all four masses.

The deflection stroke due to gravity load for the multimaterial metastructure, considered cantilevered, is computed numerically. The maximum bending found out is about 0.81 mm, which is in line with the application requirements. Arrow values are similar in both single and multi material designs. In fact, they have roughly the same stiffness and dynamic response.

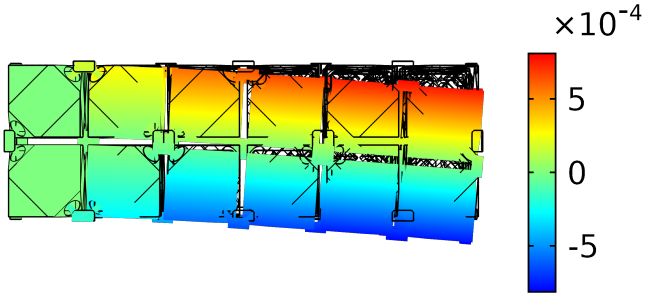

Figure 6.10: Gravity load maximum numerical displacement along gravity direction for the multimaterial metastructure.

6.4.3 Vibration transmissibility assessment

To evaluate how the finite metastructure made by three unit cells with multiple materials performs in the frequency range of interest, a numerical transmission analysis is carried out, as already done in section 3. The excitation is imposed in the same fashion: the input wave is applied on all the bottom surface of the metastructure as a prescribed z-axis acceleration, while the output is measured on the top surface in a small area as shown on the right side of Fig. 6.11, to recreate the accelerometer measurement surface considered in the experimental setup. The transmission

is then computed by dividing the computed output acceleration with the prescribed input one. Results are shown in Fig. 6.11. The black curve is obtained considering no material damping. To allow a better comparison with the dispersion, theoretical bandgaps are highlighted as yellow areas. Bandgap opening and closing frequencies are slightly different from the one retrieved with the infinite hypothesis, due to the finite nature of the metastructure.

As in Chapter 3, the material dissipation is modeled introducing a complex stiffness modulus. The same τ equal to 3 μs is considered for the analysis.

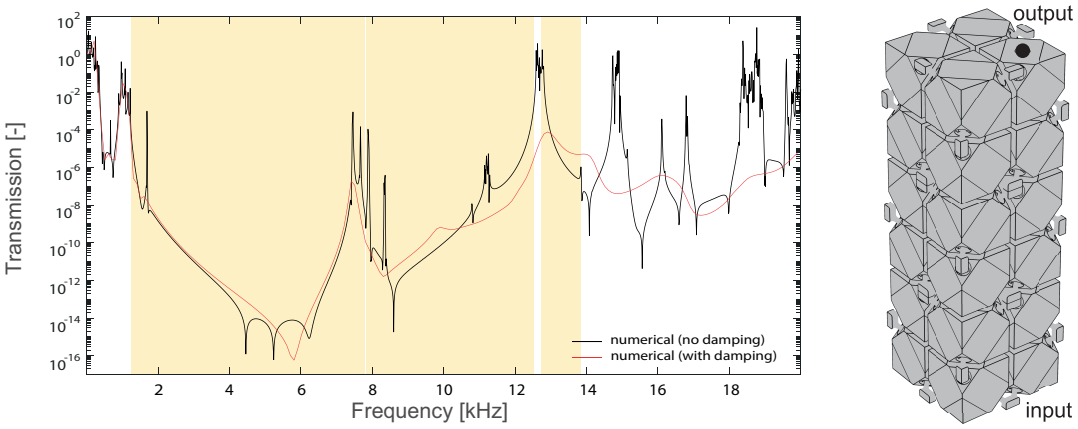

Figure 6.11: Numerical transmission diagram computed in COMSOL Multiphysics©. Theoretical bandgaps computed through the dispersion analysis are reported in yellow for comparison. A schematic view of the 1x1x3 multimaterial metastructure is also reported for the sake of clarity.

6.5 Multimaterial metastructure assembly

The multimaterial metastructure is fabricated using two different technologies: the already exploited SLS printing (specifically by EOS P 770) for plastic skeleton and a metal 3d printer (HP Desktop Metal) for the tetrahedral masses. Each production process has different associated tolerances. Therefore, CAD model have to consider the adequate clearances to make junctions between plastic skeleton and metal masses possible. In the SLS process, the cooling down of the component results in a volume shrinkage. Thus, dimensions have to be scaled to compensate for this behavior. Also metal 3D printing process is affected by a similar problem. Metal parts are printed with a filament loaded with metal particles and then they go through a debinding and a sintering process, in which there is a reduction in volume. Thus, an upstream volume compensation is needed. To take into account manufacturing tolerances, tetrahedral additional masses are drawn to be smaller then the site on which they will be mounted on the PA 2200 skeleton.

An example of the metastructure assembly with the available four steel masses is shown in the following picture. The assembly first step is to glue the masses on the skeleton pieces, as shown in Fig. 6.12. Then, skeletons are attached together producing the final structure. The remaining steel masses to be fabricated are undergoing the final step of their processing and will be available in the very near future, allowing the final assembly and the experimental validation of the metastructure.

Figure 6.12: A preliminary assembled multi-material metastructure.

Chapter 7

Conclusions and future challenges

In this thesis, an innovative multi-purpose metastructure has been proposed as a promising solution for low frequency vibration isolation tasks due to its extreme scalability and tunability, furthermore increased thanks to the usage of different materials.

The specific application of the metastructure designed is that of a handle of a vibration probe hosting an accelerometer.

Therefore, it must guaranteeing reduced size, lightweight mass, wide working frequency range with a high frequency limit up to at least 10 kHz. By exploiting the mode separation mechanism recently proposed in the literature [6], we designed a metastructure of reduced size (i.e. 4 cm unit cell) that shows a working frequency range from 1478 Hz to 10000 Hz theoretically, retrieved from numerically computed band diagram and transmissibility function. Furthermore, a static bending analysis is carried out to verify the maximum stroke was compatible with our application.

Ten prototypes made by 1x1x3 unit cells has been fabricated trough SLS process. Firstly, to evaluate the quality of the samples and to verify they meet the specifications declared by the manufacturer, a dimensional evaluation of the characteristic dimensions (cube mass side and slanting beam diameter) of the printed metastructures is carried out, along with uncertainty related to the measurement process itself and the one related to sample reproducibility. Results show mass cube heights and slanting beams diameters are strongly dependent to the manufacturing process (i.e. direction of printing, temperature release, laser accuracy). However, all fabricated samples verified the 0.3 mm uncertainty declared. Moreover, to check for dust remaining from the fabrication process, all samples are studied by computerized tomography (CT). Compression tests are then carried out on a single metastructure to obtain the force-displacement curve of the sample, which is fundamental to retrieve the corresponding load associated with a known displacement value, useful for the preload evaluation in operating tests. Exploiting the force-displacement curve,the material stiffness has been estimated and used to perform an updating of the numerical model, obtaining a Young modulus equal to 1350 MPa which fits extremely well the experimental transmissibility function. Also samples volume is evaluated in first approximation from CT point cloud, allowing to retrieve, and verify, material mass density, which in our case is about 0.05 $g/[cm^3]$ greater than the value declared by the material provider. In addition, a modal analysis is carried out, considering constraints, both numerically and experimentally (using a SLDV). Natural frequency difference is evaluated and mode shapes are compared obtaining a good agreement between numerical and experimental resonance frequencies. The transmissibility function is then measured experimentally and compared with numerical data. A vibrations attenuation of more then two orders of magnitude has been experimentally demonstrated. To evaluate the variability of the transmissibility function due to the measurement setup, a riproducibility of the experiment is carried out, obtaining its uncertainty. Furthermore, the reproducibility of the transmissibility function for all samples is evaluated and an overall frequency shift of 20 Hz for the second transmissibility function peak is measured.

The metastructure is then tested in operating conditions, i.e. using it as a decoupling element for vibration probe measurements, confirming its effectiveness in the field. The experimental setup is then defined using a feedback on the shaker acceleration due to the introduced metastructure preload. Various solutions of the connection element with the accelerometer are designed and then tested. They all seem to work fine for our application, obtaining a low deviation from ideal

performances with the optimum preload, which is usually a high enough value. Metastructure reproducibility is then evaluated with the operating test setup obtaining a good correspondence.

Lastly, to overcome dimension constraints and make the structure less voluminous, keeping unchanged or improving its performances, a multimaterial metastructure is exploited. Firstly, a sensitivity analysis is carried out on the unit cell geometric parameter, choosing a unit cell size $a = 30$ mm, a diameter of the slanting beams $d = 1.2$ mm and an offset, a parameter strictly correlated with the amount of steel, equal to 30 mm. Theoretical band structure is computed obtaining an ultra-wide gap from 1257.2 Hz to 13836 Hz. The multimaterial metastructure is then assembled for future experimental validation.

In addition to being a promising solution in vibration testing applications and thus a good candidate for a future marketable hand probe, it represents an important improvement of the metastructure proposed in [6] in terms of size and low opening frequency. In the present work, by considering the same material, indeed, the low-pass filter behavior starts at a frequency much smaller then the one proposed in [6] and the unit cell size is reduced of 1 cm in each direction regarding the single-material solution and 2 cm considering the multi-material one.

The final vibration probe design, including all elements (handling, decoupling element and accelerometer connection), should be engineered to be entirely manufactured using additive techniques. Furthermore, each element should be previously designed for the specific application (frequency range of interest, encumbrance, type of handling) and, after the needed customization, the structure should be printed by additive manufacturing as a whole. Thus, reducing costs and allowing extreme design tailoring to the specific application.

The hand held vibration probe should be engineered to be both used by a human operator or to be mounted on the end effector of a collaborative robot. Depending on final configuration, its design and working characteristics should meet different requirements. The following step, should be the design of vibrational testing for on-site production quality control in order to verify the metastructure behavior in an industrial environment.

Ultimately, available literature on metamaterials for vibration suppression mainly focus on unit cell design leaving space for further improvements in the experimental validation of fabricated samples. For this reason, a standard procedure for the experiment setup and testing need to be developed in order to evaluate metamaterial performances properly. For doing so, constraints need to be chosen in order to be a good representation of the numerical model, thus, a free-free condition is preferred with respect to a clamped one. In addition, contact and non-contact measurement techniques should be considered for this purpose, carefully assessing their optimal measurement range and sensitivity.

Appendix A

Dimensional measurements and printing accuracy

Dimensional measurement carried out on each metastructure. Measurement is performed on cubes height (z-direction), cubes width (x-y direction) and slanting beam diameter, along metastructure z-direction (i.e. along 6 numbered metastructure planes of Fig. 4.1). It is worth underline that metastructure 0 (i.e. the first manufactured one) has been printed by itself whilst the other 9 pieces where realized in a batch. Three charts, representing respectively the previously mentioned measurements, are shown for each metastructure in Fig. A.1. The numbered plain of Fig. 4.1 is reported on the x-axis of each chart. Looking at the first graph of each row, thus comparing measurements for different specimens, a decreasing (or increasing, in the case of flipped metastructure) trend for the cube height is present. This is true especially for specimens 0 and 8, in which farthest data is not compatible. Another consideration can be done comparing chart 1 and 2 of each metastructure. Cube measurements in the x and y-directions are nearly constant along longitudinal metastructure direction, with low dispersion around the mean value. In addition, they are remarkably different from height measurements from the first chart. It seems that the printing process is more accurate in the (x,y) plane then on the z-direction. Lastly, diameter measurements seem to follow an alternating trend due to their printing direction (45 deg inclination from cube planes, following its diagonals). Dimensional tolerances (of 0.3 mm) from the manufacturer are verified in the majority of measurements.

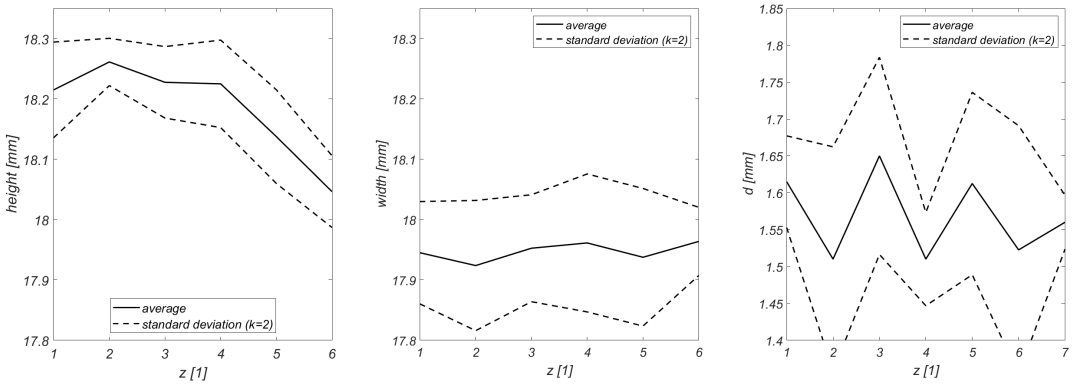

(a) Metastructure 0.

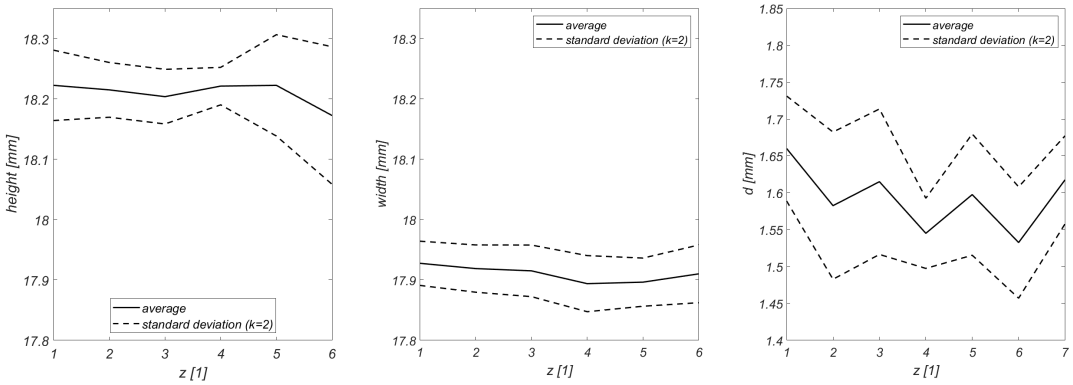

(b) Metastructure 1.

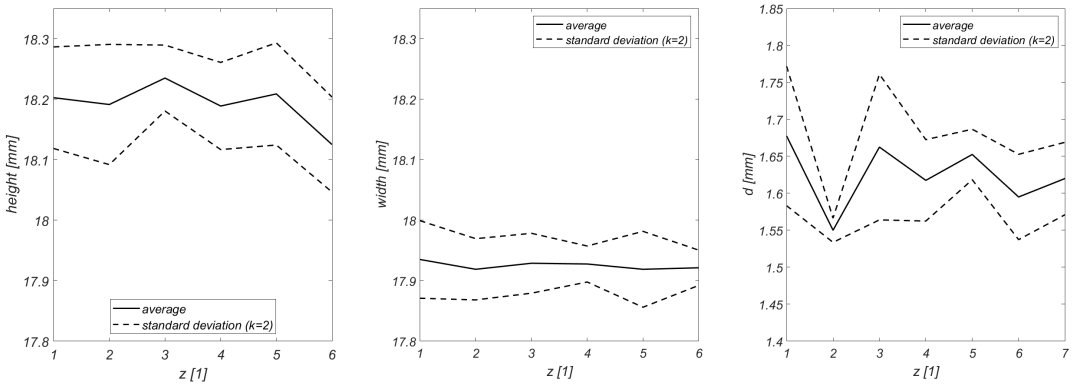

(c) Metastructure 2.

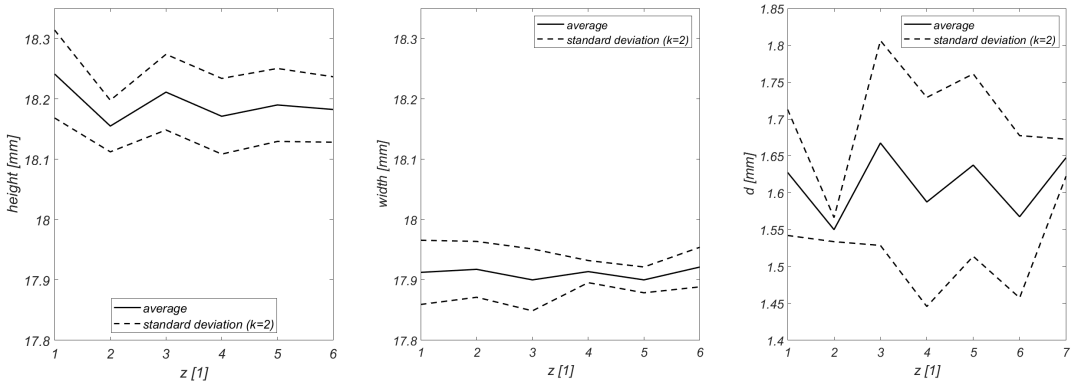

(d) Metastructure 3.

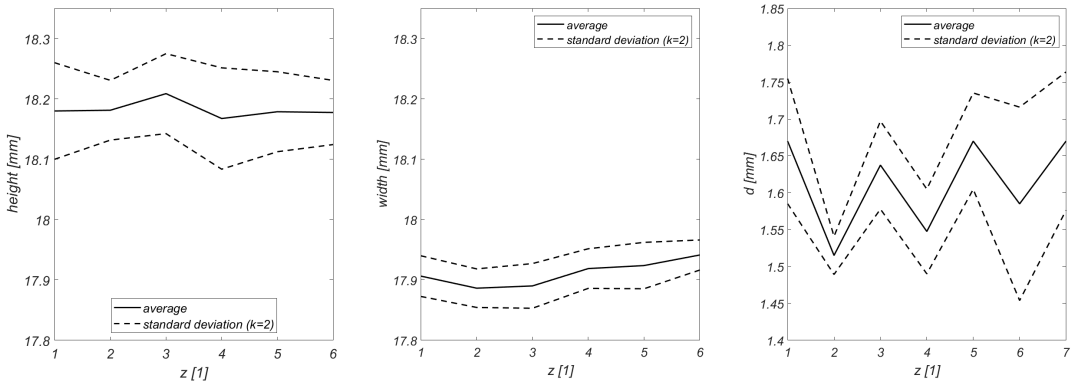

(e) Metastructure 4.

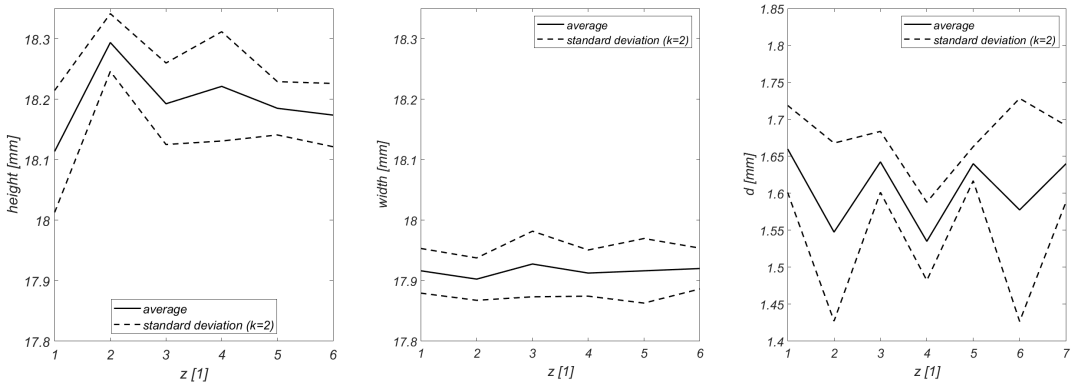

(f) Metastructure 5.

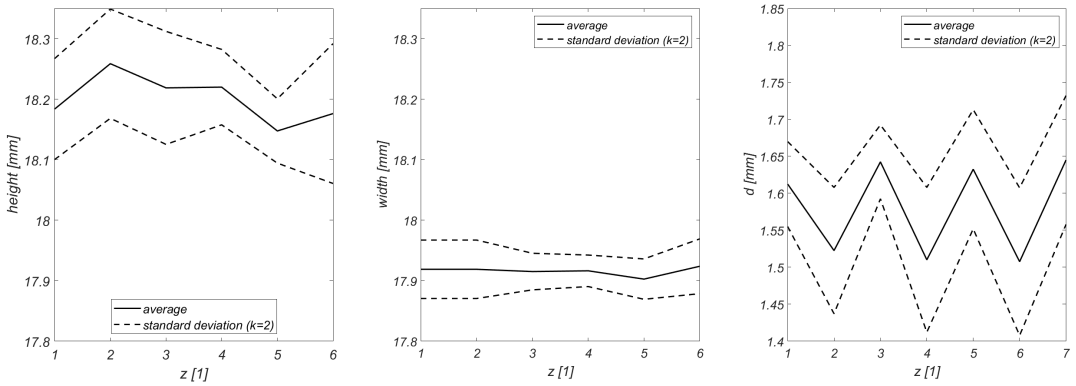

(g) Metastructure 6.

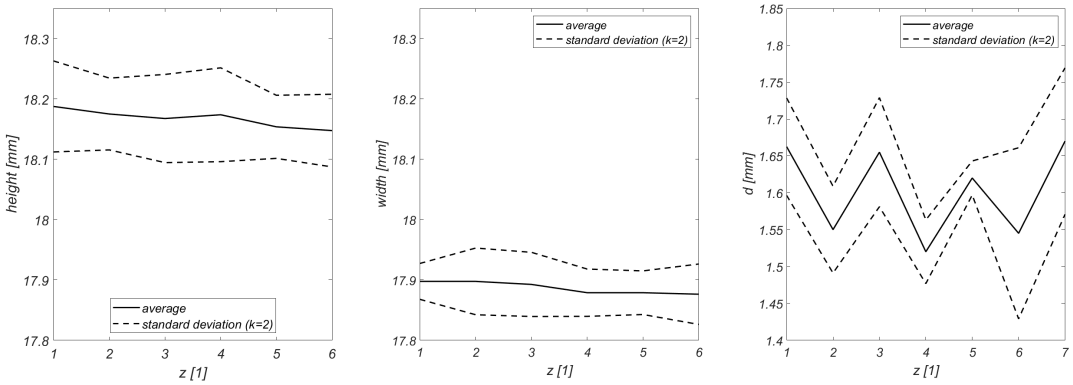

(h) Metastructure 7.

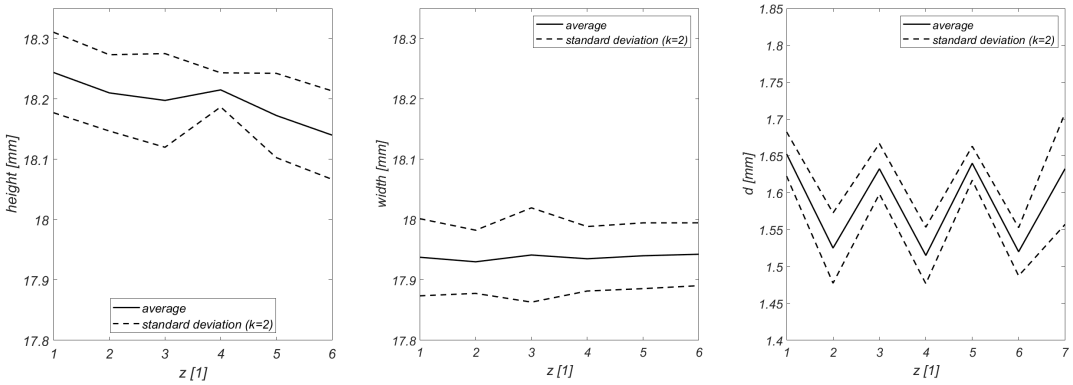

(i) Metastructure 8.

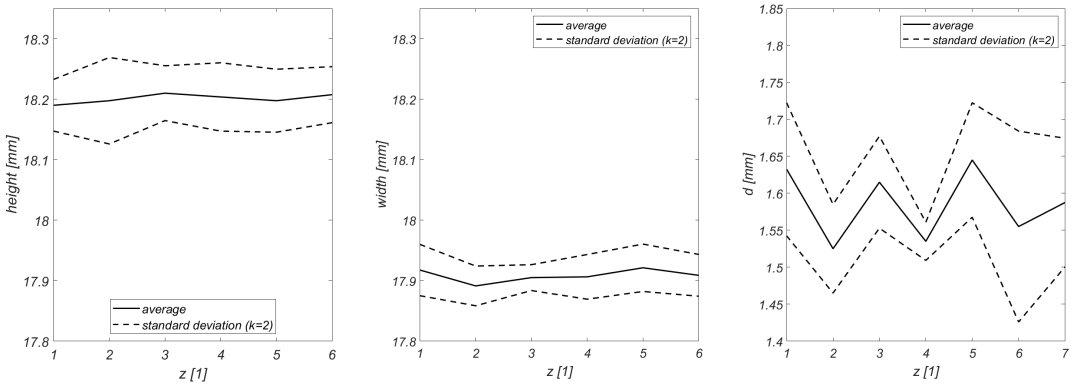

(j) Metastructure 9.

Figure A.1: Dimensional measurements on cubes height (z-direction), cubes width (x-y direction) and slanting beam diameter along metastructure z-direction (i.e. along 6 numbered metastructure planes of Fig. 4.1). Data is taken on each metastructure printed sample.

Appendix B

Mode shapes from finite element analysis

The list of eigenfrequencies and eigenmodes computed by finite element analysis with COMSOLMultiphysics© is shown in Fig. B.-1. The experimental transmissibility of Fig. 4.20 suddenly reduces its amplitude after approximately 350 Hz. Thus, low frequency modes, located before that value, are useful to characterize the metastructure dynamics due to their amplitude, when retrieved from experimental data. Modes located above

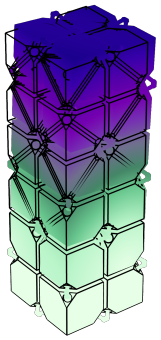

mode 1

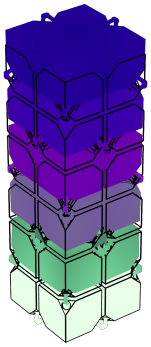

mode 2

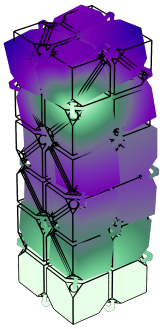

mode 3

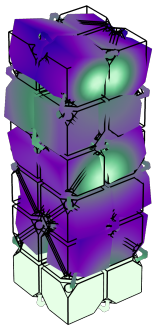

mode 4

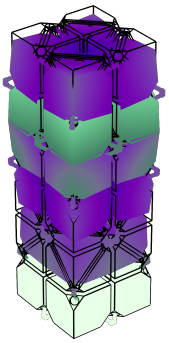

mode 5

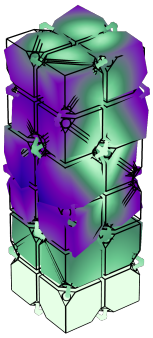

mode 6

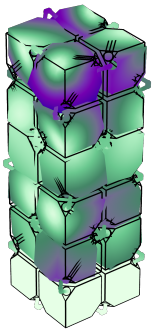

mode 7

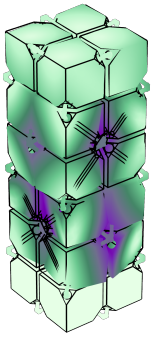

mode 8

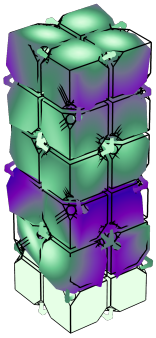

mode 9

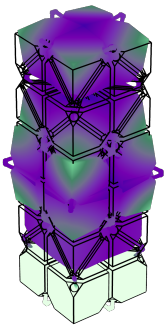

mode 10

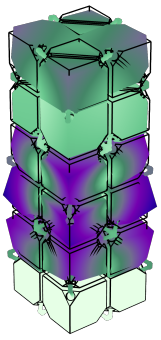

mode 11

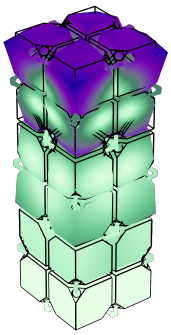

mode 12

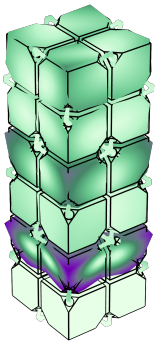

mode 13

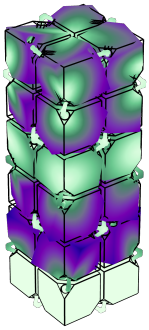

mode 14

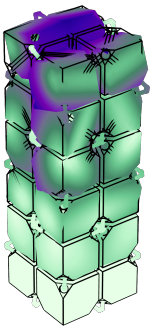

mode 15

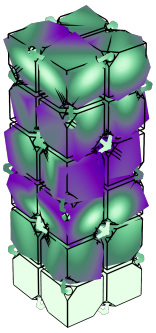

mode 16

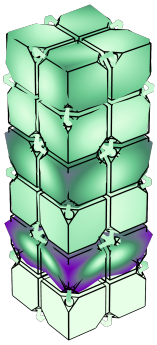

mode 17

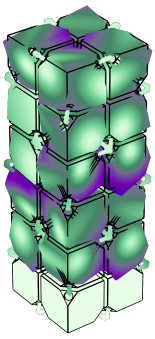

mode 18

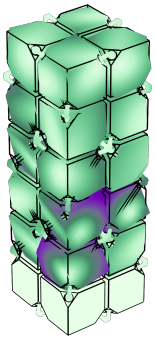

mode 19

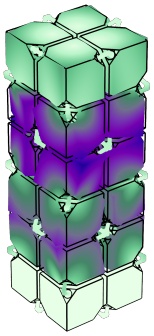

mode 20

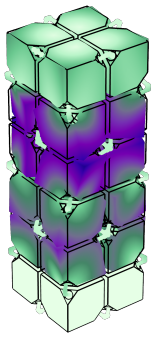

mode 21

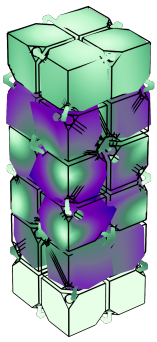

mode 22

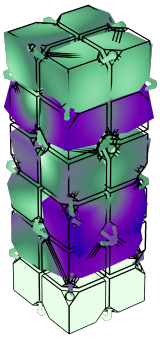

mode 23

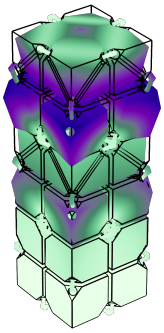

mode 24

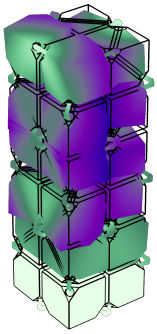

mode 25

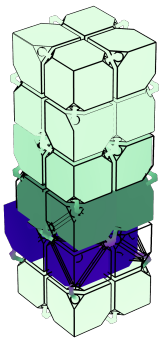

mode 26

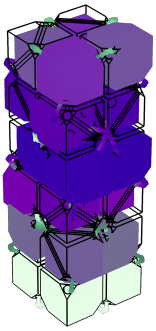

mode 27

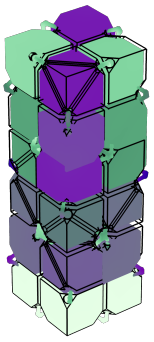

mode 28

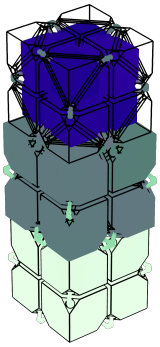

mode 29

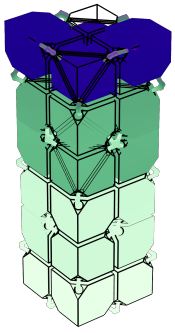

mode 30

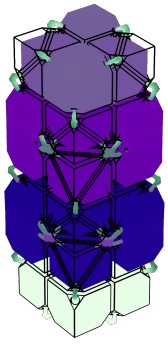

mode 31

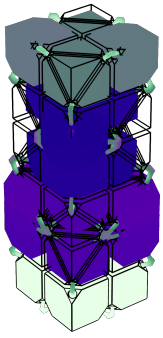

mode 32

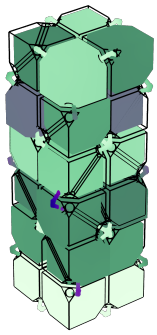

mode 33

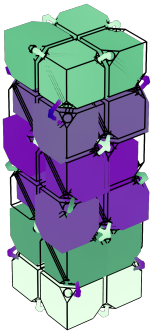

mode 34

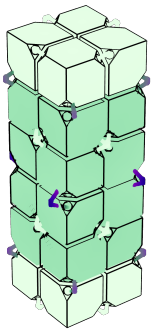

mode 35

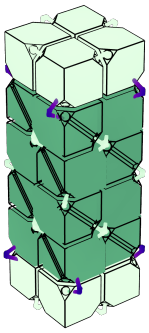

mode 36

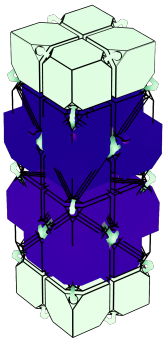

mode 37

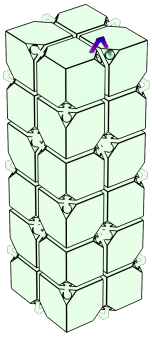

mode 38

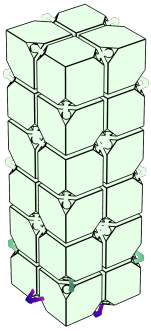

mode 39

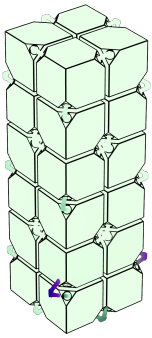

mode 40

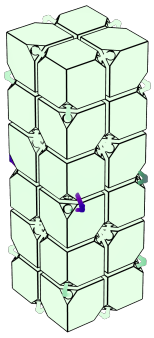

mode 41

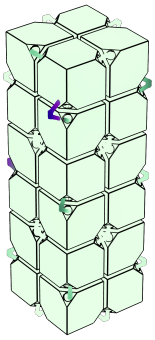

mode 42

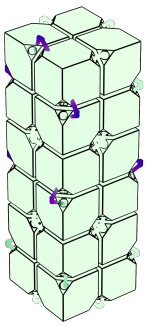

mode 43

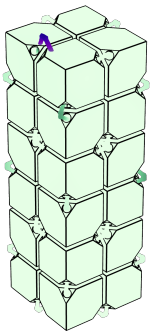

mode 44

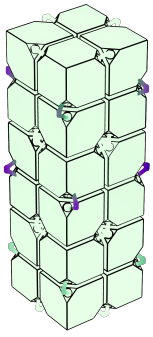

mode 45

Figure B.-1: Finite element modal analysis.

.

Appendix C

Mode shapes from experimental modal analysis

The list of eigenfrequencies and eigenmodes retrieved from experimental modal analysis is shown in Fig. C.-1. Modes located above

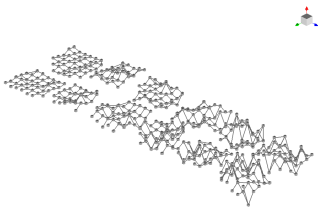

mode 1

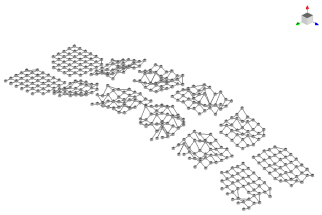

mode 2

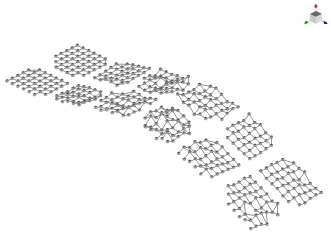

mode 3

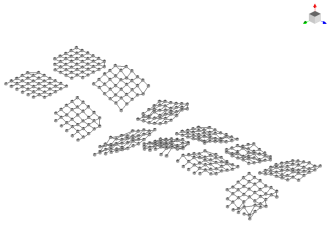

mode 4

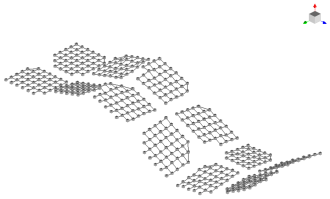

mode 5

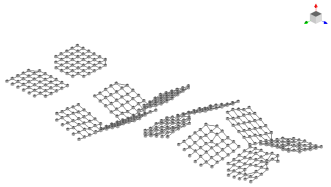

mode 6

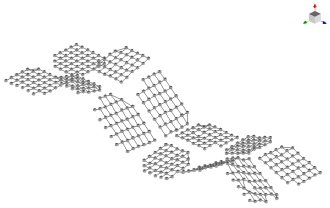

mode 7

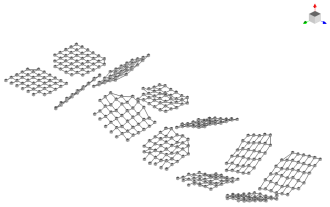

mode 8

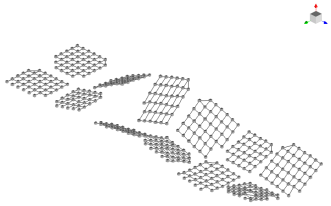

mode 9

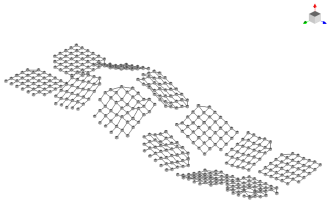

mode 10

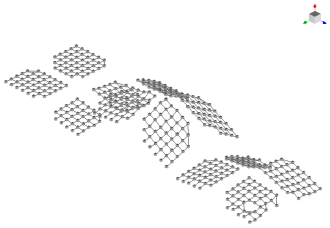

mode 11

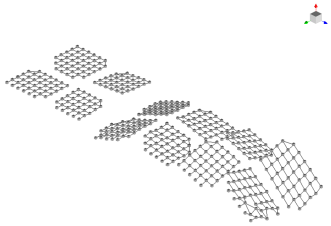

mode 12

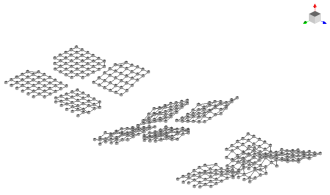

mode 13

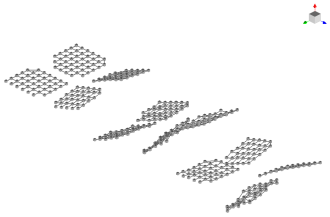

mode 14

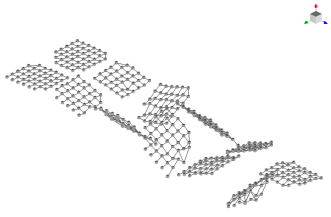

mode 15

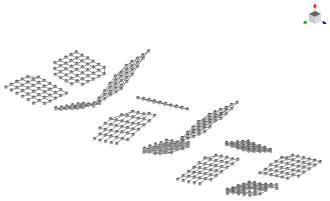

mode 16

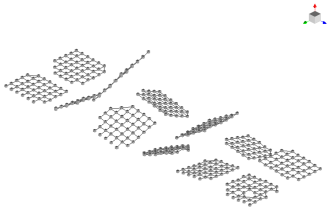

mode 17

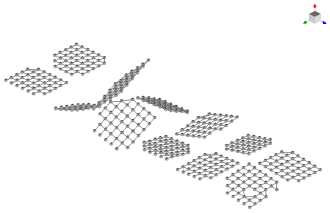

mode 18

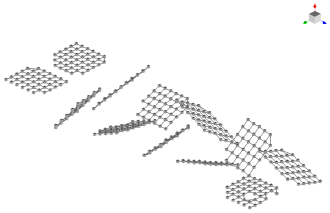

mode 19

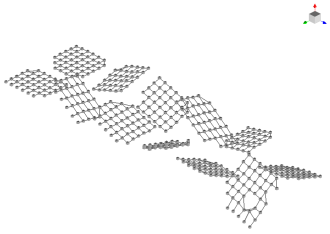

mode 20

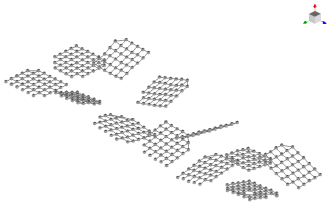

mode 21

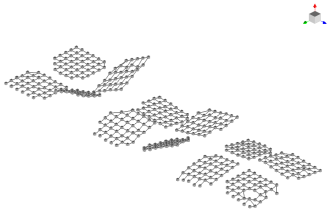

mode 22

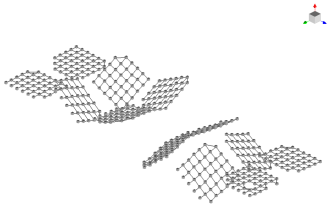

mode 23

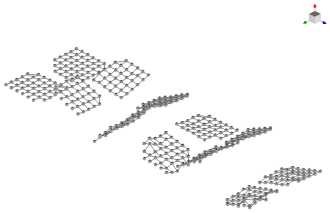

mode 24

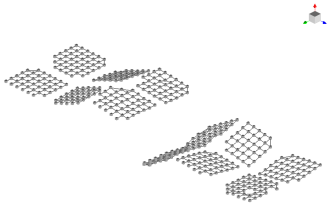

mode 25

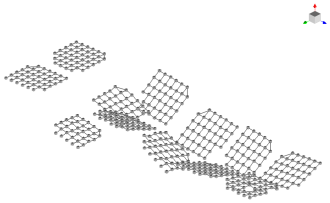

mode 26

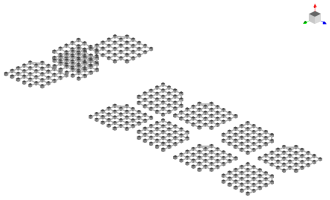

mode 29

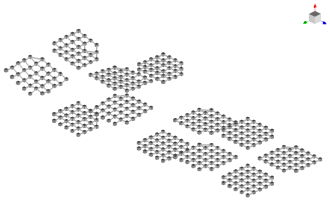

mode 29

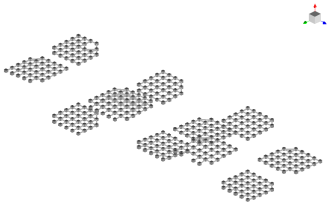

mode 30

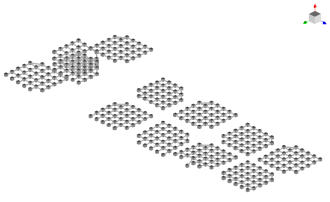

mode 31

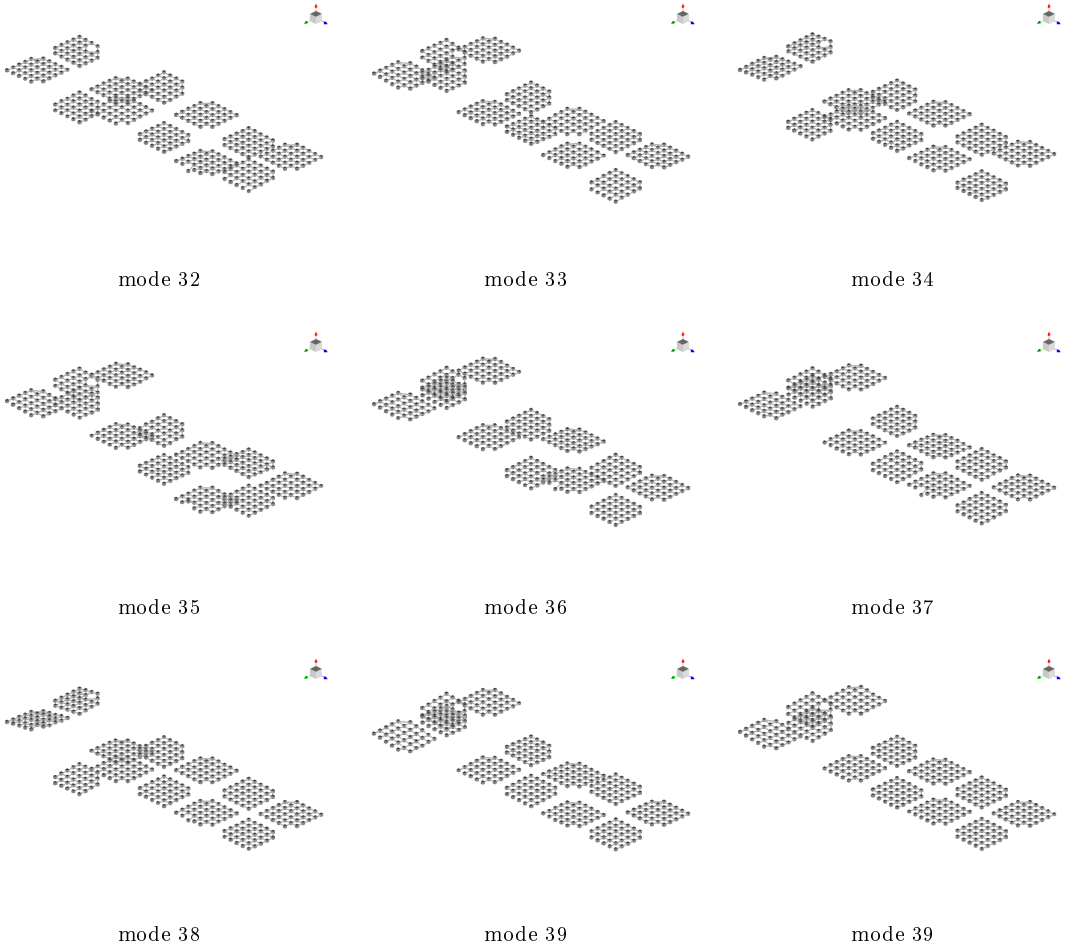

Figure C.-1: Mode shapes retrieved from experimental modal analysis.

Appendix D

Tomographic images for internal remaining dust detection

Tomographic investigations are carried out on each metastructure sample to search for irregularities. Hereafter, representative tomographic images from computed reconstruction are shown. Black areas correspond to air, lighter areas to PA 2200 print and gray areas to remaining dust.

The first sample is clean enough, dust remains should not invalidate its functionality. Instead, in the second one there is a small presence of dust blocking slanting beams in a part of the structure. The situation get worst looking at sample three. On the other side, sample four is almost perfectly clean. Sample five has small cleaning issues. On contrary, sample six need a further cleaning. Sample seven is properly cleaned. Sample eight has remaining dust compromising its functionality. Lastly, sample nine has a small amount of remaining dust attached and should work as intended.

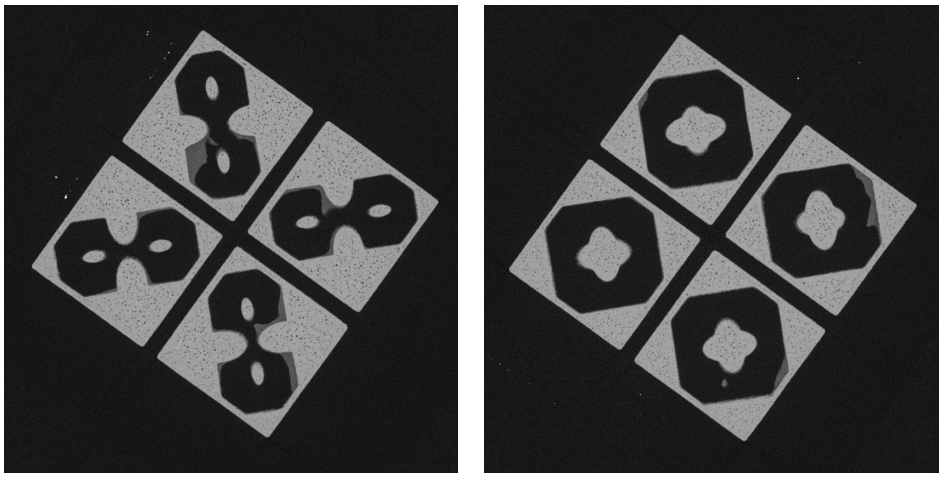

slice 1 slice 2

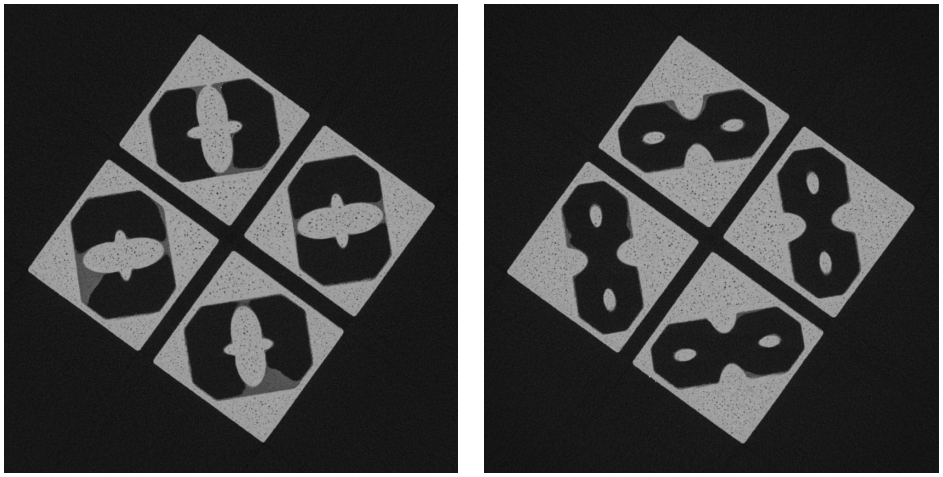

slice 3 slice 4

Figure D.1: Tomographic slice for sample 2.

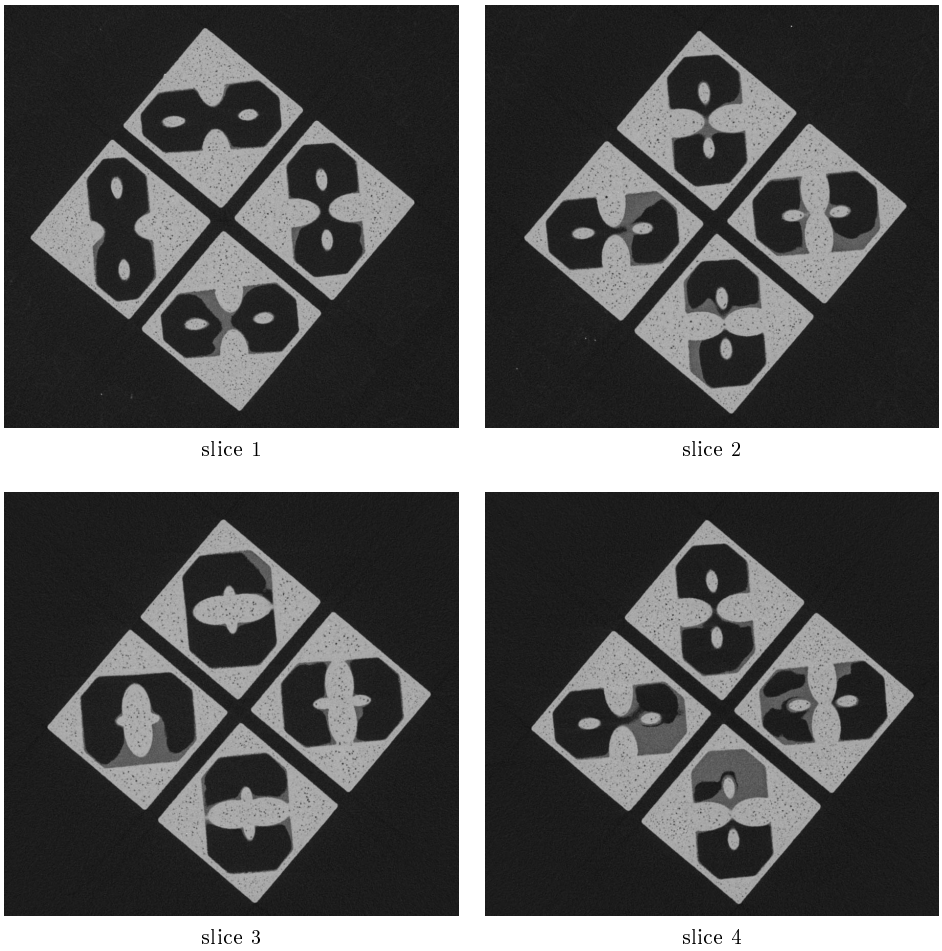

slice 1 slice 2

slice 3 slice 4

Figure D.2: Tomographic slice for sample 3.

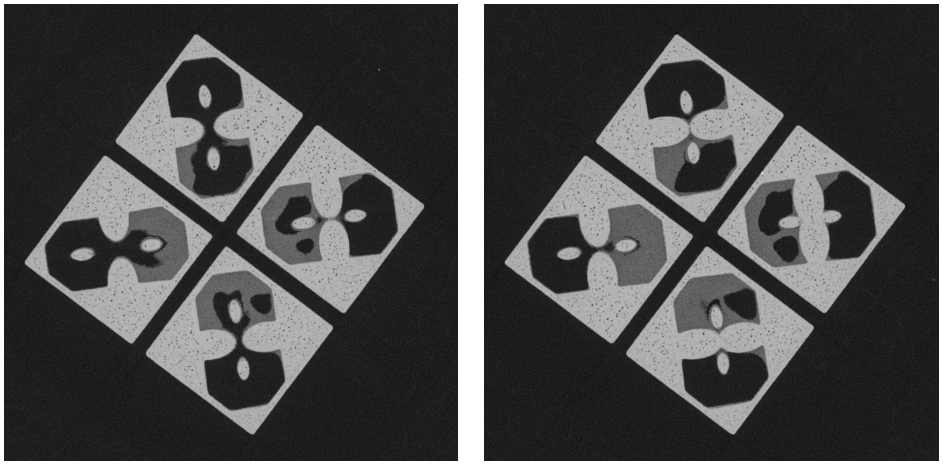

slice 1 slice 2

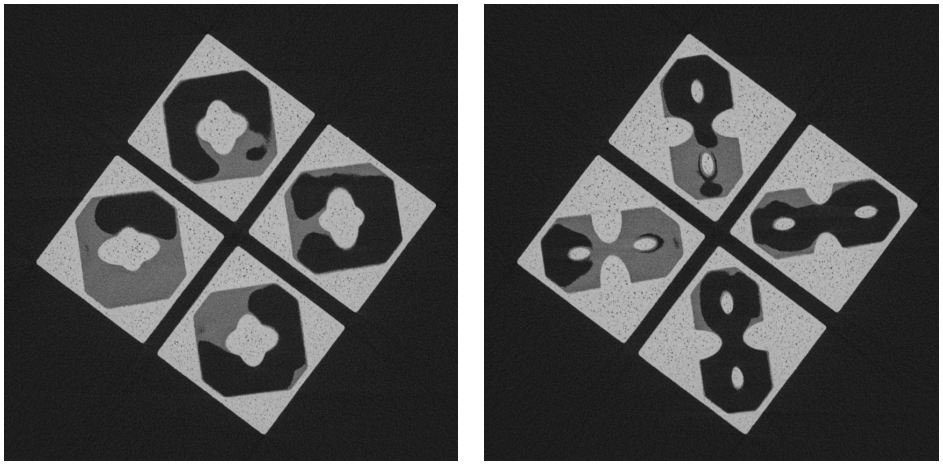

slice 3 slice 4

Figure D.3: Tomographic slice for sample 4.

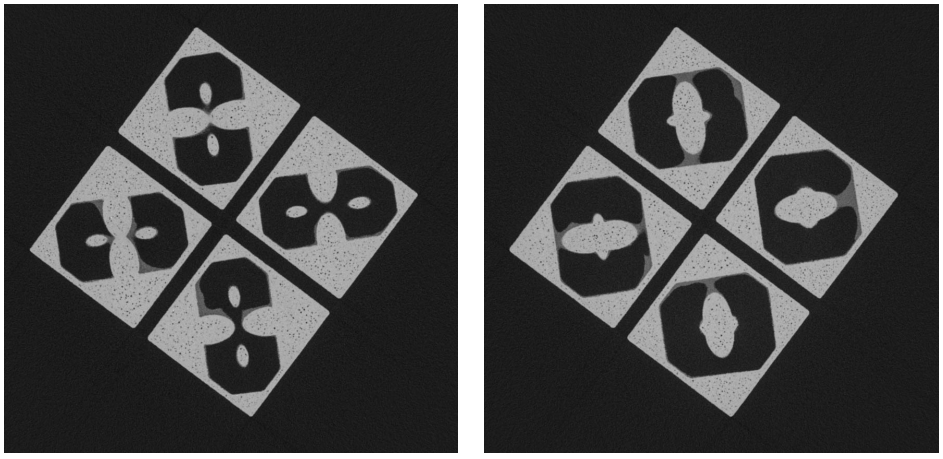

slice 1 slice 2

Figure D.4: Tomographic slice for sample 5.

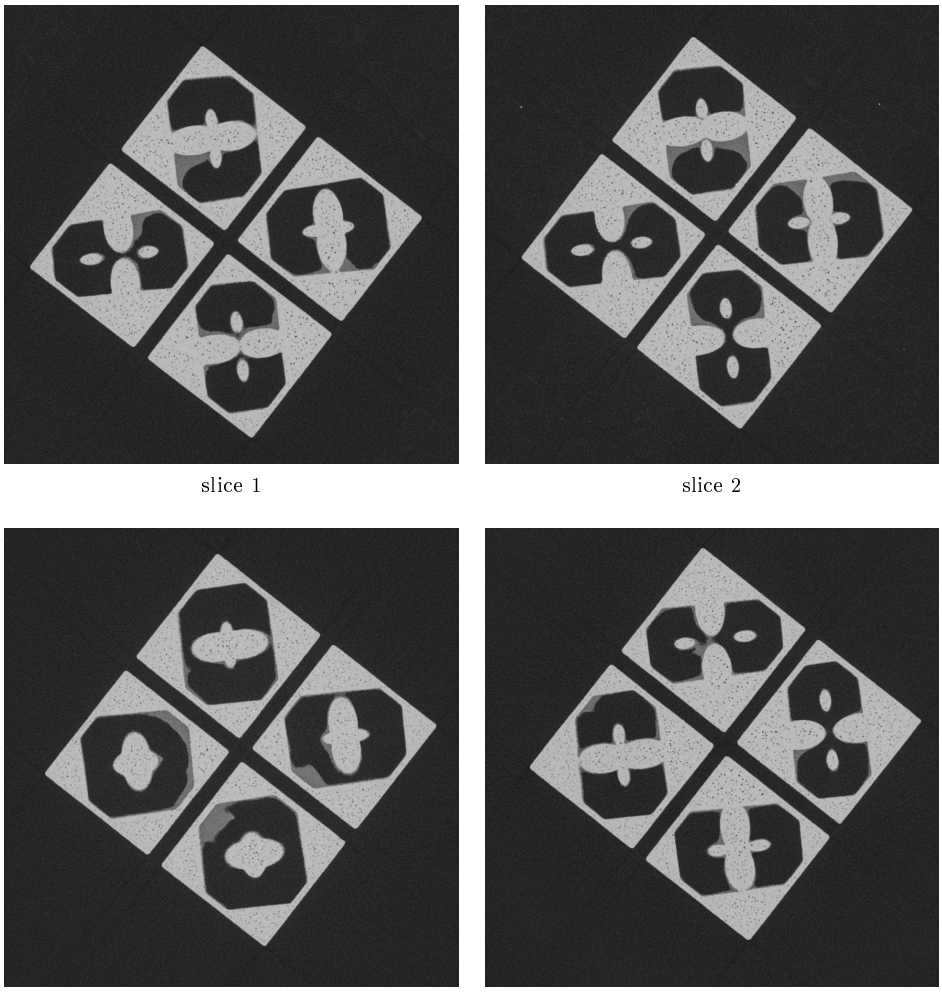

slice 1 slice 2

slice 3 slice 4

Figure D.5: Tomographic slice for sample 6.

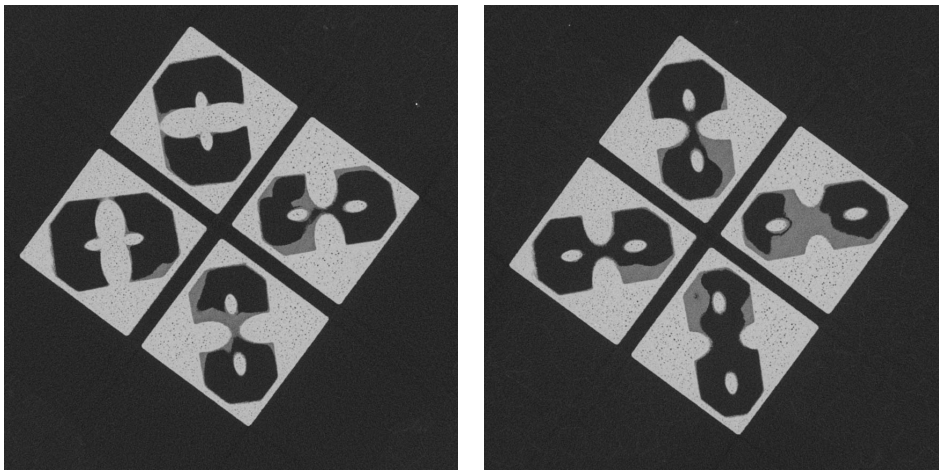

slice 1 slice 2

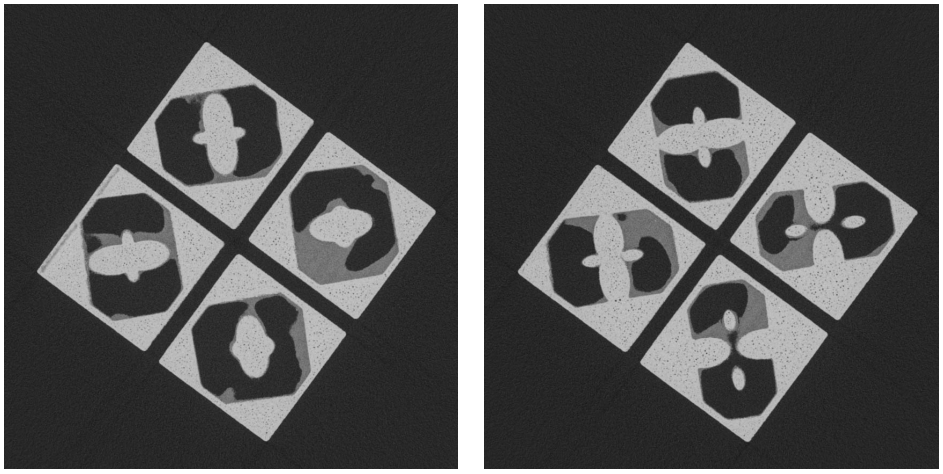

slice 3 slice 4

Figure D.6: Tomographic slice for sample 7.

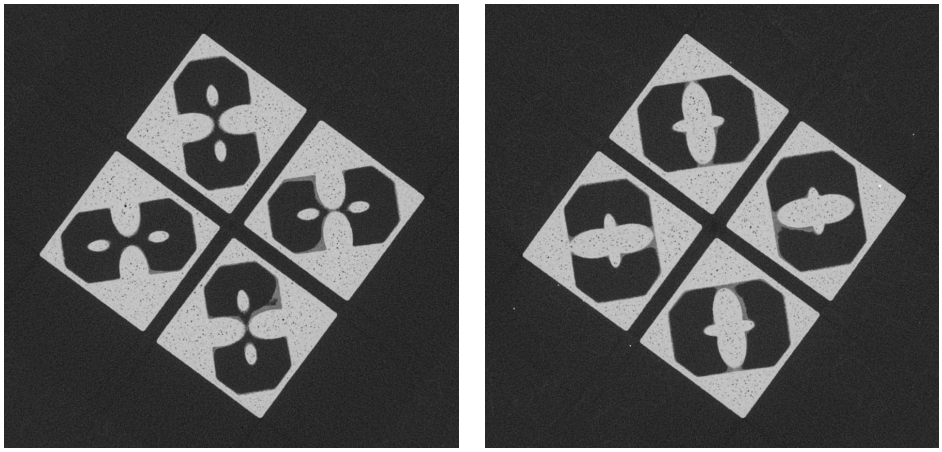

slice 1 slice 2

slice 3 slice 4

Figure D.7: Tomographic slice for sample 8.

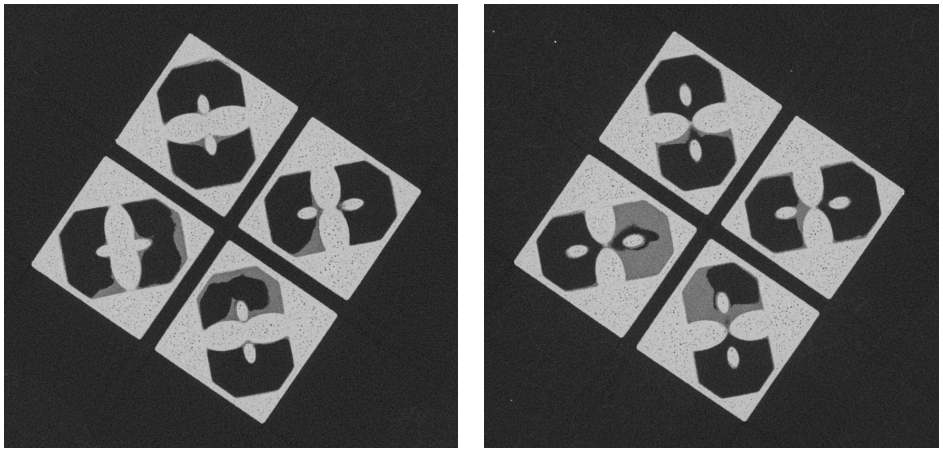

slice 1 slice 2

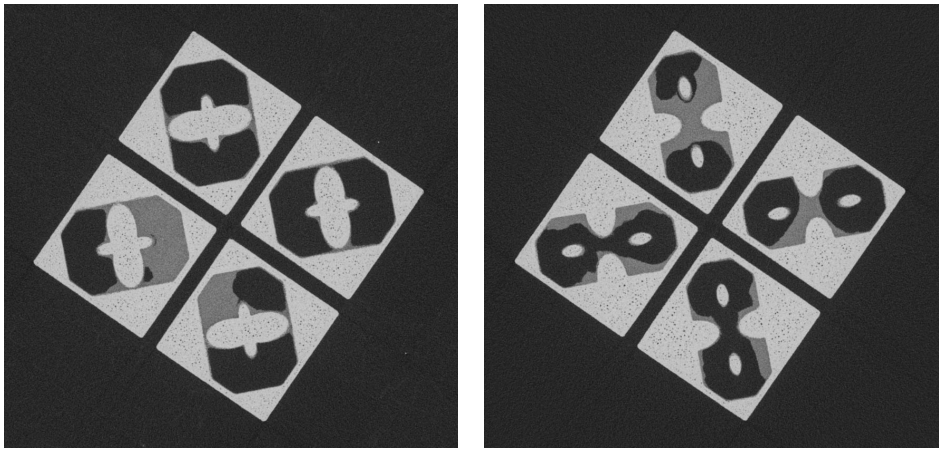

slice 3 slice 4

Figure D.8: Tomographic slice for sample 9.

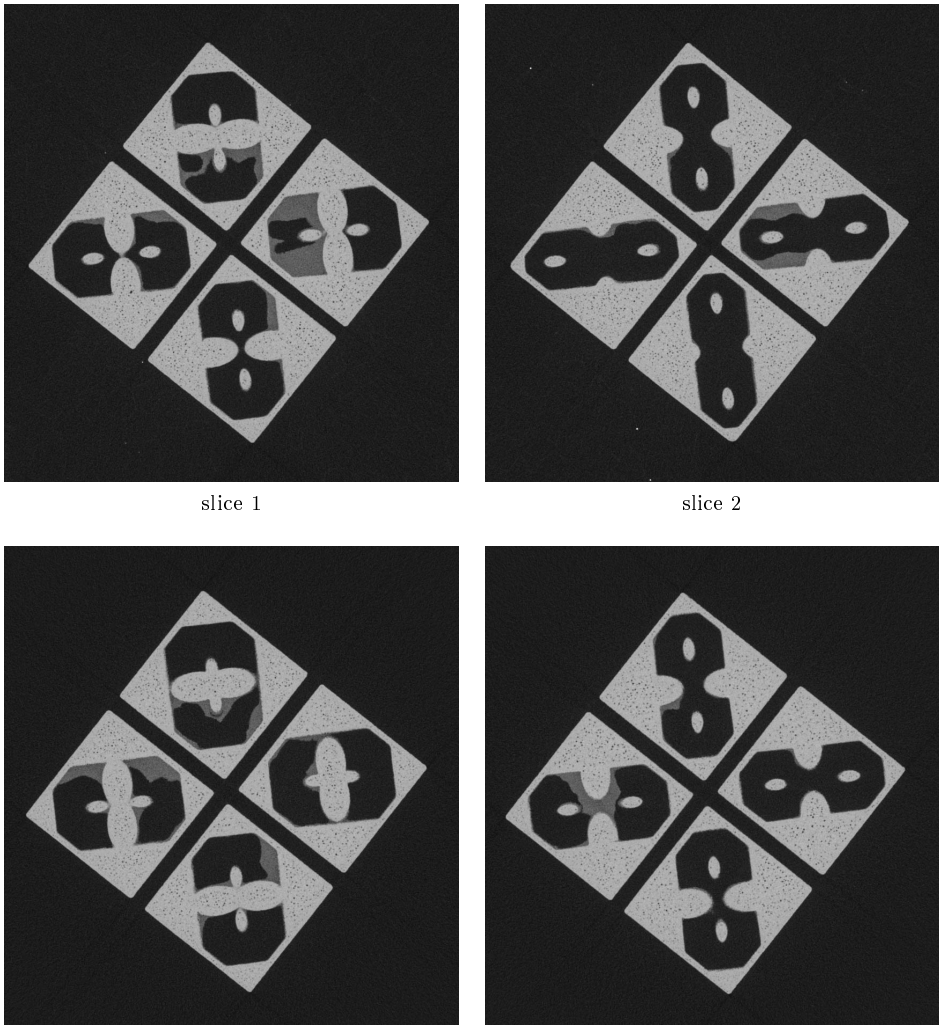

slice 1 slice 2

slice 3 slice 4

Figure D.9: Tomographic slice for sample 10.

Bibliography

[1] Jacob Fraden. *Handbook of Modern Sensors*. Springer International Publishing, 2015.

[2] Harald Ibach and Hans Lüth. *Solid-State Physics*. Springer Berlin Heidelberg.

[3] Philip Hofmann. *Solid State Physics*. Wiley-VCH GmbH, 2015.

[4] J.P. Groby A. Cebrecos, V. Romero-GarcÍa. Eea summer school - acoustic metamaterials and sonic crystals.

[5] Yan Pennec and Bahram Djafari-Rouhani. Fundamental properties of phononic crystal. In *Phononic Crystals*, pages 23–50. Springer New York.

[6] L. D'Alessandro, E. Belloni, R. Ardito, F. Braghin, and A. Corigliano. Mechanical low-frequency filter via modes separation in 3d periodic structures. *Applied Physics Letters*, 111(23):231902, 2017.

[7] Robert Randall. *Vibration-based Condition Monitoring : Industrial, Automotive and Aerospace Applications*. John Wiley & Sons.

[8] Timo Malm, Timo Salmi, Ilari Marstio, and Iina Aaltonen. Are collaborative robots safe? In *Automaatiopäivät 23*, pages 110–117, Finland, 2019. Finnish Society of Automation. Automaatiopäivät23 ; Conference date: 15-05-2019 Through 16-05-2019.

[9] Ales Vysocky and Petr Novak. HUMAN – ROBOT COLLABORATION IN INDUSTRY. 2016(02):903–906.

[10] Eloise Matheson, Riccardo Minto, Emanuele G. G. Zampieri, Maurizio Faccio, and Giulio Rosati. Human–robot collaboration in manufacturing applications: A review. 8(4):100.

[11] Miriam Matúšová, Marcela Bučányová, and Erika Hrušková. The future of industry with collaborative robots. 299:02008.

[12] Tobias Kopp, Marco Baumgartner, and Steffen Kinkel. Success factors for introducing industrial human-robot interaction in practice: an empirically driven framework. 112(3-4):685–704.

[13] Heiner Lasi, Peter Fettke, Hans-Georg Kemper, Thomas Feld, and Michael Hoffmann. Industry 4.0. 6(4):239–242.

[14] *Industry 4.0: Industrial Revolution of the 21st Century*. Springer-Verlag GmbH, 2018.

[15] Emre Cevikcan Alp Ustundag. *Industry 4.0: Managing The Digital Transformation*. Springer-Verlag GmbH, 2017.

[16] C Mineo, M Vasilev, B Cowan, C N MacLeod, S G Pierce, C Wong, E Yang, R Fuentes, and E J Cross. Enabling robotic adaptive behaviour capabilities for new industry 4.0 automated quality inspection paradigms. 62(6):338–344.

[17] Foivos Psarommatis, Gökan May, Paul-Arthur Dreyfus, and Dimitris Kiritsis. Zero defect manufacturing: state-of-the-art review, shortcomings and future directions in research. 58(1):1–17.

[18] Florian Eger, Daniel Coupek, Davide Caputo, Marcello Colledani, Mariluz Penalva, Jon Ander Ortiz, Hermann Freiberger, and Gernot Kollegger. Zero defect manufacturing strategies for reduction of scrap and inspection effort in multi-stage production systems. 67:368–373.

[19] Elisa Verna, Gianfranco Genta, Maurizio Galetto, and Fiorenzo Franceschini. Towards zero defect manufacturing: probabilistic model for quality control effectiveness. In *2021 IEEE International Workshop on Metrology for Industry 4.0 & IoT (MetroInd4.0&IoT)*. IEEE.

[20] K. Vacharanukul and S. Mekid. In-process dimensional inspection sensors. 38(3):204–218.

[21] Ercihan Kiraci, Pasquale Franciosa, Glen A. Turley, Alan Olifent, Alex Attridge, and Mark A. Williams. Moving towards in-line metrology: evaluation of a laser radar system for in-line dimensional inspection for automotive assembly systems. 91(1-4):69–78.

[22] Zai-Gen Wu, Chao-Yi Lin, Hao-Wei Chang, and Po Ting Lin. Inline inspection with an industrial robot (IIIR) for mass-customization production line. 20(11):3008.

[23] Daniel Mejia-Parra, Jairo Sánchez, Oscar Ruiz-Salguero, Marcos Alonso, Alberto Izaguirre, Erik Gil, Jorge Palomar, and Jorge Posada. In-line dimensional inspection of warm-die forged revolution workpieces using 3d mesh reconstruction. 9(6):1069.

[24] Gianluca Di Giulio, A. Nicolini, Gian M. Revel, and Enrico P. Tomasini. Quality control of electronic devices by vibration analysis. In Enrico P. Tomasini, editor, *Fourth International Conference on Vibration Measurements by Laser Techniques: Advances and Applications*. SPIE.

[25] Steve Vanlanduit, Peter Verboven, Bart Cauberghe, Louis Huysmans, and Patrick Guillaume. On the use of a laser doppler vibrometer for quality control of picture tubes. In *SPIE Proceedings*. SPIE.

[26] Jiri Vass and C. Cristalli. Bearing fault detection for on-line quality control of electric motors. *10th IMEKO TC10 International Conference on Technical Diagnostics*, 01 2005.

[27] C. Cristalli, N. Paone, and R.M. Rodriguez. Mechanical fault detection of electric motors by laser vibrometer and accelerometer measurements. 20(6):1350–1361.

[28] Cristina Cristalli, Barbara Torcianti, and Jiri Vass. A new method for filtering speckle noise in vibration signals measured by laser doppler vibrometry for on-line quality control. In *Seventh International Conference on Vibration Measurements by Laser Techniques: Advances and Applications*. SPIE.

[29] Jiri Vass. Reducing speckle noise in vibration signals measured with laser doppler vibrometry.

[30] Barbara Torcianti, Cristina Cristalli, and Jiri Vass. Non-contact measurement for mechanical fault detection in production line. In *2007 IEEE International Symposium on Diagnostics for Electric Machines, Power Electronics and Drives*. IEEE.

[31] C. Cristalli, Enrico Concettoni, and Barbara Torcianti. *Vibration measurements and analysis for mechanical fault detection in production line*, pages 253–295. 01 2011.

[32] S. Serafini, N. Paone, and P. Castellini. Quality control agent: Self-adaptive laser vibrometry for on-line diagnostics. In *AIP Conference Proceedings*. AIP.

[33] E. García Plaza, P.J. Núñez López, and E.M. Beamud González. Efficiency of vibration signal feature extraction for surface finish monitoring in CNC machining. 44:145–157.

[34] Déborah Reis, Fernanda Vanzo, Jorge Reis, and Marcus Duarte. Archives of acoustics.

[35] Ernest Doebelin. *Strumenti e metodi di misura*. McGraw-Hill.

[36] Felix Levinzon. *Piezoelectric Accelerometers with Integral Electronics*. Springer-Verlag GmbH, 2014.

[37] D. J. Ewins. *Modal Testing: Theory, Practice and Application*. WILEY, 2009.

[38] Paulo S. Varoto Kenneth G. Mcconnell. *Vibration Testing*. John Wiley & Sons, 2008.

[39] C. Q. Liu. *Principles of vibration analysis : with applications in automotive engineering*. SAE International.

[40] Bruel and an HBK company Kjaer. Structure-borne noise sensor.

[41] M. S. Kushwaha, P. Halevi, L. Dobrzynski, and B. Djafari-Rouhani. Acoustic band structure of periodic elastic composites. 71(13):2022–2025.

[42] M. Gorisse, S. Benchabane, G. Teissier, C. Billard, A. Reinhardt, V. Laude, E. Defaÿ, and M. Aïd. Observation of band gaps in the gigahertz range and deaf bands in a hypersonic aluminum nitride phononic crystal slab. 98(23):234103.

[43] A. Khelif, A. Choujaa, B. Djafari-Rouhani, M. Wilm, S. Ballandras, and V. Laude. Trapping and guiding of acoustic waves by defect modes in a full-band-gap ultrasonic crystal. 68(21):214301.

[44] A. Khelif, A. Choujaa, S. Benchabane, B. Djafari-Rouhani, and V. Laude. Guiding and bending of acoustic waves in highly confined phononic crystal waveguides. 84(22):4400–4402.

[45] Fu-Li Hsiao, Abdelkrim Khelif, Hanane Moubchir, Abdelkrim Choujaa, Chii-Chang Chen, and Vincent Laude. Waveguiding inside the complete band gap of a phononic crystal slab. 76(5):056601.

[46] Tzung-Chen Wu, Tsung-Tsong Wu, and Jin-Chen Hsu. Waveguiding and frequency selection of lamb waves in a plate with a periodic stubbed surface. 79(10):104306.

[47] P. H. Otsuka, K. Nanri, O. Matsuda, M. Tomoda, D. M. Profunser, I. A. Veres, S. Danworaphong, A. Khelif, S. Benchabane, V. Laude, and O. B. Wright. Broadband evolution of phononic-crystal-waveguide eigenstates in real- and k-spaces. 3(1).

[48] F. Cervera, L. Sanchis, J. V. Sánchez-Pérez, R. Martínez-Sala, C. Rubio, F. Meseguer, C. López, D. Caballero, and J. Sánchez-Dehesa. Refractive acoustic devices for airborne sound. 88(2):023902.

[49] A. Håkansson, J. Sánchez-Dehesa, and L. Sanchis. Acoustic lens design by genetic algorithms. 70(21):214302.

[50] Andreas Håkansson, Francisco Cervera, and José Sánchez-Dehesa. Sound focusing by flat acoustic lenses without negative refraction. 86(5):054102.

[51] Bakhtiyar Orazbayev and Romain Fleury. Far-field subwavelength acoustic imaging by deep learning. 10(3):031029.

[52] Suxia Yang, J. H. Page, Zhengyou Liu, M. L. Cowan, C. T. Chan, and Ping Sheng. Ultrasound tunneling through 3d phononic crystals. 88(10):104301.

[53] Suxia Yang, J. H. Page, Zhengyou Liu, M. L. Cowan, C. T. Chan, and Ping Sheng. Focusing of sound in a 3d phononic crystal. 93(2):024301.

[54] Xiangdong Zhang and Zhengyou Liu. Negative refraction of acoustic waves in two-dimensional phononic crystals. 85(2):341–343.

[55] J. H. Page. Focusing of ultrasonic waves by negative refraction in phononic crystals. 6(12):121606.

[56] Jian Liu, Liping Li, Baizhan Xia, and Xianfeng Man. Fractal labyrinthine acoustic metamaterial in planar lattices. 132-133:20–30.

[57] A O Krushynska, F Bosia, M Miniaci, and N M Pugno. Spider web-structured labyrinthine acoustic metamaterials for low-frequency sound control. 19(10):105001.

[58] Xiao-Jian Liu and You-Hua Fan. Band structure characteristics of t-square fractal phononic crystals. 22(3):036101.

[59] A.S. Fallah, N. Navadeh, V.V. Tereshchuk, and V.N. Gorshkov. Phononic dispersion in anisotropic pseudo-fractal hyper-lattices. 164:107560.

[60] Junyi Liu, Hanbei Guo, and Ting Wang. A review of acoustic metamaterials and phononic crystals. 10(4):305.

[61] Thomas Vasileiadis, Jeena Varghese, Visnja Babacic, Jordi Gomis-Bresco, Daniel Navarro Urrios, and Bartlomiej Graczykowski. Progress and perspectives on phononic crystals. 129(16):160901.

[62] Zhengyou Liu, Xixiang Zhang, Yiwei Mao, Y. Y. Zhu, Zhiyu Yang, C. T. Chan, and Ping Sheng. Locally resonant sonic materials. *Science*, 289(5485):1734–1736, 2000.

[63] Xiyue An, Changliang Lai, Hualin Fan, and Chuanzeng Zhang. 3d acoustic metamaterial-based mechanical metalattice structures for low-frequency and broadband vibration attenuation. *International Journal of Solids and Structures*, 191-192:293–306, 2020.

[64] Rodger Walser. Metamaterials: An introduction. In *Introduction to Complex Mediums for Optics and Electromagnetics*, pages 295–316. SPIE.

[65] Ni Qing and Cheng Jian-Chun. Homogenization of two-dimensional phononic crystals at low frequencies. 22(9):2305–2308.

[66] Ying-Hong Liu, Chien C. Chang, Ruey-Lin Chern, and C. Chung Chang. Phononic band gaps of elastic periodic structures: A homogenization theory study. 75(5):054104.

[67] Min Yang, Guancong Ma, Ying Wu, Zhiyu Yang, and Ping Sheng. Homogenization scheme for acoustic metamaterials. 89(6):064309.

[68] Laetitia Roux, Charles Croënne, Christian Audoly, and Anne-Christine Hladky-Hennion. Homogenization of acoustic metamaterials using retrieval methods. 127(22):225102.

[69] M. Ibarias, Yu. Zubov, J. Arriaga, and A. A. Krokhin. Phononic crystal as a homogeneous viscous metamaterial. 2(2):022053.

[70] Xingcun Colin Tong. *Functional Metamaterials and Metadevices*. Springer International Publishing.

[71] Z. Yao, V. Zega, Yan Su, Yi Zhou, Jingbo Ren, J. Zhang, and A. Corigliano. Design, fabrication and experimental validation of a metaplate for vibration isolation in mems. *Journal of Microelectromechanical Systems*, 29:1401–1410, 2020.

[72] S. Wang, L.C. Popa, and D. Weinstein. Gan mems resonator using a folded phononic crystal structure. *Solid-State Sensors, Actuators and Microsystems Workshop Hilton Head Island, South Carolina*, 29:72–75, 2014.

[73] Z. Yang, H. M. Dai, N. H. Chan, G. C. Ma, and Ping Sheng. Acoustic metamaterial panels for sound attenuation in the 50–1000 hz regime. 96(4):041906.

[74] Jia-Hao He and Hsin-Haou Huang. Complete vibrational bandgap in thin elastic metamaterial plates with periodically slot-embedded local resonators. *Archive of Applied Mechanics*, 88(8):1263–1274, 2018.

[75] Yubao Song, Jihong Wen, Hao Tian, Xiangyu Lu, Zhengchu Li, and Leping Feng. Vibration and sound properties of metamaterial sandwich panels with periodically attached resonators: Simulation and experiment study. *Journal of Sound and Vibration*, 489:115644, 2020.

[76] Hao Zhang, Shengbing Chen, Zongzheng Liu, Yubao Song, and Yong Xiao. Light-weight large-scale tunable metamaterial panel for low-frequency sound insulation. 13(6):067003.

[77] Yang Liu, Xiyue An, Hailong Chen, and Hualin Fan. Vibration attenuation of finite-size metaconcrete: Mechanism, prediction and verification. *Composites Part A: Applied Science and Manufacturing*, 143:106294, 2021.

[78] Stephanie J. Mitchell, Anna Pandolfi, and Michael Ortiz. Investigation of elastic wave transmission in a metaconcrete slab. *Mechanics of Materials*, 91:295–303, 2015.

[79] Fariha Mir, Mohammadsadegh Saadatzi, Riaz U. Ahmed, and Sourav Banerjee. Acoustoelastic MetaWall noise barriers for industrial application with simultaneous energy harvesting capability. 139:282–292.

[80] Muhammad, C. W. Lim, and N. S. Vyas. A novel application of multi-resonant dissipative elastic metahousing for bearings. 34(4):449–465.

[81] Wenwang Wu, Wenxia Hu, Guian Qian, Haitao Liao, Xiaoying Xu, and Filippo Berto. Mechanical design and multifunctional applications of chiral mechanical metamaterials: A review. 180:107950.

[82] Srajan Dalela, P. S. Balaji, and D. P. Jena. A review on application of mechanical metamaterials for vibration control. pages 1–26.

[83] Sanjay Kumar and Heow Pueh Lee. Recent advances in active acoustic metamaterials. 11(08):1950081.

[84] Ziwei Wang, Quan Zhang, Kai Zhang, and Gengkai Hu. Tunable digital metamaterial for broadband vibration isolation at low frequency. 28(44):9857–9861.

[85] C. Claeys, E. Deckers, B. Pluymers, and W. Desmet. A lightweight vibro-acoustic metamaterial demonstrator: Numerical and experimental investigation. *Mechanical Systems and Signal Processing*, 70-71:853–880, 2016.

[86] M. Nouh, O. Aldraihem, and A. Baz. Vibration characteristics of metamaterial beams with periodic local resonances. *Journal of Vibration and Acoustics*, 136(6), 10 2014. 061012.

[87] Kathryn H. Matlack, Anton Bauhofer, Sebastian Krödel, Antonio Palermo, and Chiara Daraio. Composite 3d-printed metastructures for low-frequency and broadband vibration absorption. *Proceedings of the National Academy of Sciences*, 113(30):8386–8390, 2016.

[88] E. Panahi, A. Hosseinkhani, M.F. Khansanami, D. Younesian, and M. Ranjbar. Novel cross shape phononic crystals with broadband vibration wave attenuation characteristic: Design, modeling and testing. *Thin-Walled Struct.*, 163:107665, 2021.

[89] Fen Yu, Yueli Huo, Qian Ding, Cong Wang, Jinxin Yao, Zhenpeng He, Yongtao Sun, Haoqiang Gao, and Aijun Sun. Structural design and band gap properties of 3d star-shaped single-phase metamaterials.

[90] Heng Jiang, Mangong Zhang, Yu Liu, Dongliang Pei, Meng Chen, and Yuren Wang. Band gaps and vibration isolation of a three-dimensional metamaterial with a star structure. *Materials*, 13(17), 2020.

[91] H. Meng, D. Chronopoulos, A.T. Fabro, W. Elmadih, and I. Maskery. Rainbow metamaterials for broadband multi-frequency vibration attenuation: Numerical analysis and experimental validation. 465:115005.

[92] Claus Claeys, Noé Geraldo Rocha de Melo Filho, Lucas Van Belle, Elke Deckers, and Wim Desmet. Design and validation of metamaterials for multiple structural stop bands in waveguides. *Extreme Mechanics Letters*, 12:7–22, 2017. Frontiers in Mechanical Metamaterials.

[93] Kaijun Yi and Manuel Collet. Broadening low-frequency bandgaps in locally resonant piezoelectric metamaterials by negative capacitance. *Journal of Sound and Vibration*, 493:115837, 2021.

[94] Miles V. Barnhart, Xianchen Xu, Yangyang Chen, Shun Zhang, Jizhou Song, and Guoliang Huang. Experimental demonstration of a dissipative multi-resonator metamaterial for broadband elastic wave attenuation. *Journal of Sound and Vibration*, 438:1–12, 2019.

[95] A.O. Krushynska, M. Miniaci, F. Bosia, and N.M. Pugno. Coupling local resonance with bragg band gaps in single-phase mechanical metamaterials. *Extreme Mechanics Letters*, 12:30–36, 2017. Frontiers in Mechanical Metamaterials.

[96] Luca D'Alessandro, Anastasiia O. Krushynska, Raffaele Ardito, Nicola M. Pugno, and Alberto Corigliano. A design strategy to match the band gap of periodic and aperiodic metamaterials. *Scientific Reports*, 10(1):16403, 2020.

[97] Weifeng Jiang, Ming Yin, Qihao Liao, Luofeng Xie, and Guofu Yin. Three-dimensional single-phase elastic metamaterial for low-frequency and broadband vibration mitigation. 190:106023.

[98] Muhammad and C.W. Lim. Dissipative multiresonant pillared and trampoline metamaterials with amplified local resonance bandgaps and broadband vibration attenuation. 142(6).

[99] Xiang Fei, Lei Jin, Xiujuan Zhang, Xin Li, and Minghui Lu. Three-dimensional anti-chiral auxetic metamaterial with tunable phononic bandgap. 116(2):021902.

[100] Nitish Kumar and Siladitya Pal. Low frequency and wide band gap metamaterial with divergent shaped star units: Numerical and experimental investigations. 115(25):254101.

[101] Weijian Zhou, Muhammad, Weiqiu Chen, Zhenyu Chen, and C.W. Lim. Actively controllable flexural wave band gaps in beam-type acoustic metamaterials with shunted piezoelectric patches. 77:103807.

[102] W. Elmadih, D. Chronopoulos, W. P. Syam, I. Maskery, H. Meng, and R. K. Leach. Three-dimensional resonating metamaterials for low-frequency vibration attenuation. *Scientific Reports*, 9(1):11503, 2020.

[103] Muhammad, C.W. Lim, and J.N. Reddy. Built-up structural steel sections as seismic metamaterials for surface wave attenuation with low frequency wide bandgap in layered soil medium. 188:440–451.

[104] L. D'Alessandro, R. Ardito, F. Braghin, and A. Corigliano. Low frequency 3d ultra-wide vibration attenuation via elastic metamaterial. *Scientific Reports*, 9(1):8039, 2019.

[105] Luca D'Alessandro, Valentina Zega, Raffaele Ardito, and Alberto Corigliano. 3d auxetic single material periodic structure with ultra-wide tunable bandgap. *Scientific Reports*, 8(1):2262, 2018.

[106] Yan Lu, Yang Yang, James K. Guest, and Ankit Srivastava. 3-d phononic crystals with ultra-wide band gaps. *Scientific Reports*, 7(1):7137, 2017.

[107] L. D'Alessandro, E. Belloni, R. Ardito, A. Corigliano, and F. Braghin. Modeling and experimental verification of an ultra-wide bandgap in 3d phononic crystal. *Applied Physics Letters*, 109(22):221907, 2016.

[108] G. Acar and C. Yilmaz. Experimental and numerical evidence for the existence of wide and deep phononic gaps induced by inertial amplification in two-dimensional solid structures. 332(24):6389–6404.

[109] J. V. Sánchez-Pérez, D. Caballero, R. Mártinez-Sala, C. Rubio, J. Sánchez-Dehesa, F. Meseguer, J. Llinares, and F. Gálvez. Sound attenuation by a two-dimensional array of rigid cylinders. 80(24):5325–5328.

[110] Matthew D. Guild, Victor M. García-Chocano, Weiwei Kan, and José Sánchez-Dehesa. Acoustic metamaterial absorbers based on multilayered sonic crystals. 117(11):114902.

[111] Ralf Lucklum. Phononic crystals and metamaterials – promising new sensor platforms. 87:40–45.

[112] Vincent Laude and Abdelkrim Khelif. Computational problems and numerical techniques for the analysis of phononic crystals. In *Phononic Crystals*, pages 85–107. Springer New York.

[113] Christopher Hakoda, Joseph Rose, Parisa Shokouhi, and Clifford Lissenden. Using floquet periodicity to easily calculate dispersion curves and wave structures of homogeneous waveguides. In *AIP Conference Proceedings*. Author(s).

[114] N. (Cornell University) Mermin Neil (Cornell University) Ashcroft. *Solid State Physics*. Cengage Learning, Inc, 1976.

[115] Charles Kittel. *Introduction to Solid State Physics*. WILEY, 2004.

[116] T. Gorishnyy, C. K. Ullal, M. Maldovan, G. Fytas, and E. L. Thomas. Hypersonic phononic crystals. 94(11):115501.

[117] Frieder Lucklum and Michael Vellekoop. Design and fabrication challenges for millimeter-scale three-dimensional phononic crystals. 7(11):348.

[118] I-Chieh Lee, N. Jeyaprakash, and Che-Hua Yang. Characterization of ceramic phononic crystals prepared with additive manufacturing: Ultrasonic technique and finite element analysis. 46(17):27550–27560.

[119] Toyokatsu Miyashita. Full band gaps of sonic crystals made of acrylic cylinders in air –numerical and experimental investigations–. 41(Part 1, No. 5B):3170–3175.

[120] R. Martínez-Sala, J. Sancho, J. V. Sánchez, V. Gómez, J. Llinares, and F. Meseguer. Sound attenuation by sculpture. 378(6554):241–241.

[121] C. Croënne, E. J. S. Lee, Hefei Hu, and J. H. Page. Band gaps in phononic crystals: Generation mechanisms and interaction effects. 1(4):041401.

[122] Bo Yuan, Victor F. Humphrey, Jihong Wen, and Xisen Wen. On the coupling of resonance and bragg scattering effects in three-dimensional locally resonant sonic materials. 53(7):1332–1343.

[123] Jaesoon Jung, Hyun-Guk Kim, Seongyeol Goo, Kyoung-Jin Chang, and Semyung Wang. Realisation of a locally resonant metamaterial on the automobile panel structure to reduce noise radiation. 122:206–231.

[124] Yufan Tang, Shuwei Ren, Han Meng, Fengxian Xin, Lixi Huang, Tianning Chen, Chuanzeng Zhang, and Tian Jian Lu. Hybrid acoustic metamaterial as super absorber for broadband low-frequency sound. 7(1).

[125] EOS. Pa2200 material data sheet for eosint p.

[126] Wahyu Setyawan and Stefano Curtarolo. High-throughput electronic band structure calculations: Challenges and tools. *Computational Materials Science*, 49(2):299–312, 2010.

[127] Rebecca Ford. Material parameters of polyamide pa 2200.

[128] J. Natarajan. *Advances in Additive Manufacturing Processes*. Bentham Science Publishers, 2021.

[129] PCB model 352c23 datasheet.

[130] Everaldo de Barros and Carlos d'Andrade Souto. Evaluation of a vibration text fixture. 22(3).